

LARGE-SCAN-RANGE ELECTROTHERMAL MEMS MICROMIRRORS AND  
MICROLENSSES AND THEIR BIOMEDICAL IMAGING APPLICATIONS

By

LIN LIU

A DISSERTATION PRESENTED TO THE GRADUATE SCHOOL  
OF THE UNIVERSITY OF FLORIDA IN PARTIAL FULFILLMENT  
OF THE REQUIREMENTS FOR THE DEGREE OF  
DOCTOR OF PHILOSOPHY

UNIVERSITY OF FLORIDA

2013

© 2013 Lin Liu

To my parents, Changgui Liu and Xinlan Gong, and my husband, Lu Peng, for their  
endless love and unwavering support

## ACKNOWLEDGMENTS

I would like to express my deepest appreciation to my advisor, Professor Huikai Xie, who has continually given me guidance, support and encouragement. Professor Xie is a patient teacher and an inspiring advisor, who has shared his invaluable knowledge and experience without reservation and always inspired me to explore new ideas and innovative solutions. I enjoyed the open research environment Professor Xie created in our Biophotonics & Microsystems Laboratory (BML). In this environment, I was well-supported and also given freedom to conceive my own ideas. I also appreciate that Professor Xie not only acted as the best advisor for my research but a valuable friend in my life. I'm especially grateful for the strong trust and confidence Professor Xie placed in me which made me believe in myself and motivated me to reach my full potentials. This dissertation would not have been possible without Professor Xie's persistent help and support.

I would like to thank my committee members, Professor Toshikazu Nishida, Professor Huabei Jiang, Professor Henry Zmuda, and Professor Peter Zory, for serving on my dissertation committee. The lectures from Professor Nishida provided me the fundamentals for my research in MEMS. I also thank Professor Nishida for his challenging questions and constructive suggestions in the proposal defense of this research. These questions and suggestions were extremely beneficial to my confocal endomicroscopy project. I was greatly enlightened from the discussions with Professor Jiang on image reconstruction issues. I'm also grateful for Professor Jiang's great support in our collaboration project. I thank Professor Zmuda for sacrificing his time and serving on my dissertation committee. I'm thankful to Professor Zory for open his lab facilities to me. I always appreciate the efforts Professor Zory made to fix his Argon Ion

laser so I could use it for my research. Professor Zory is one of the greatest scientists I've ever met and I thank him for showing me his rigorous research methodologies and irresistible enthusiasm for scientific experiments.

I would like to acknowledge the academic instructions and friendship from Dr. Shuguang Guo. Dr. Guo is a great OCT specialist who can always manage to explain optics in most understandable ways. My acknowledgement also goes to Dr. Lei Wu, Dr. Kemiao Jia, Dr. Hongzhi Sun, Dr. Mingliang Wang, and Dr. Sagnik Pal, whose advice, guiding and friendship have been invaluable to me on academic level and personal level. I would like to thank my research collaborators, Dr. Huabei Jiang's group and Dr. Xingde Li's group, for their time and efforts dedicated to our projects. I also cherish all the memories in the BML family, and treasure the friendship with all the colleagues in BML. It's my great pleasure to work together with Erkang Wang, Wenjun Liao, Jiping Li, Victor Zeng, Xiaoyang Zhang, Can Duan, Wenjing Liu, Yingtao Ding, Andrea Pais, and Sean Samuelson.

Last, but by no means least, I thank my parents, Changgui Liu and Xinlan Gong, for giving me the most selfless and endless love. I thank my dear husband, Lu Peng, for standing aside with me for all these years and giving me true love and unwavering support.

## TABLE OF CONTENTS

	<u>page</u>
ACKNOWLEDGMENTS.....	4
LIST OF TABLES.....	8
LIST OF FIGURES.....	9
ABSTRACT .....	13
CHAPTER	
1 INTRODUCTION .....	15
1.1 Conventional Cancer Diagnosis Methods and Their Limitations.....	15
1.2 Emerging Biomedical Imaging Technologies .....	16
1.3 MEMS-Based Endoscopy .....	20
1.4 MEMS Optical Scanners.....	23
1.4.1 MEMS Micromirrors.....	23
1.4.2 MEMS Microlens Scanners .....	28
1.5 Research Objectives.....	31
1.6 Dissertation Overview .....	32
2 EMERGING BIOMEDICAL IMAGING METHODOLOGIES .....	34
2.1 Optical Coherence Tomography .....	34
2.1.1 Principles of OCT .....	34
2.1.2 Theoretical Analysis and Imaging Parameters .....	36
2.2 Confocal Scanning Microscopy.....	42
2.2.1 Theory of Confocal Scanning Microscopy .....	42
2.2.2 Imaging Properties .....	45
2.2.2.1 Resolution .....	45
2.2.2.2 Contrast .....	49
2.2.3 Confocal Scanning Endomicroscopy .....	51
2.3 Chapter Summary.....	54
3 THROUGH-SILICON-VIAS MICROMIRROR AND ENDOSCOPIC OCT APPLICATIONS.....	55
3.1 Electrothermal Bimorph Actuators .....	56
3.1.1 Principles of Electrothermal Bimorph Actuation.....	56
3.1.2 Optimization and Materials Selection .....	59
3.2 TSV Micromirror.....	61
3.2.1 TSV Micromirror Design .....	61
3.2.2 Device Fabrication.....	65
3.2.3 Device Characterization .....	65

3.3	Endoscopic OCT Imaging Using TSV Micromirror .....	69
3.3.1	Endoscopic OCT System .....	69
3.3.2	Imaging Experiment and Results.....	71
3.4	Chapter Summary.....	74
4	MICROMIRRORS BASED ON A CURVED CONCENTRIC BIMORPH ACTUATOR .....	75
4.1	Motivations for Circular Mirror and Curved Actuator .....	75
4.2	Electrothermal CCBA Design.....	76
4.1.1	Design Descriptions.....	76
4.1.2	Analytical Model .....	79
4.1.3	Finite Element Analysis .....	85
4.3	MEMS Micromirrors Based on CCBA .....	87
4.3.1	Design and Simulation.....	87
4.3.2	Device Fabrication.....	92
4.3.3	Device Characterization .....	93
4.4	Chapter Summary.....	99
5	MICROLENS SCANNERS AND CONFOCAL MICROSCOPY APPLICATIONS..	100
5.1	Electrothermal Microlens Scanners .....	101
5.2	MEMS-Based 2D Confocal Scanning Microscope .....	105
5.2.1	2D CSM System.....	105
5.2.2	MEMS Microlens Scanner for Automatic Depth Scan .....	106
5.2.3	System Characterization .....	108
5.2.4	Imaging Experiments and Results.....	109
5.3	MEMS-Based 3D Confocal Scanning Microscope .....	111
5.3.1	3D CSM System.....	111
5.3.2	MEMS Scanning Devices .....	112
5.3.3	System Characterization .....	115
5.3.4	Imaging Experiments and Results.....	117
5.4	MEMS-Based 3D Confocal Scanning Endomicroscope.....	120
5.4.1	3D Confocal Endomicroscope System .....	121
5.4.2	Endomicroscopic Probe Design .....	125
5.4.3	MEMS Scanning Devices .....	127
5.4.4	System Characterization .....	131
5.4.5	Imaging Experiments and Results.....	133
5.5	Chapter Summary.....	138
6	CONCLUSION AND FUTURE WORK.....	139
6.1	Research Accomplishments .....	139
6.2	Future Work.....	143
	LIST OF REFERENCES .....	146
	BIOGRAPHICAL SKETCH.....	164

## LIST OF TABLES

<u>Table</u>		<u>page</u>
1-1	Overview of imaging systems .....	16
3-1	Thermal-mechanical properties of commonly used MEMS materials .....	59
3-2	Design parameters summary of TSV micromirror.....	64
5-1	Design parameters of microlens scanners .....	103

## LIST OF FIGURES

<u>Figure</u>		<u>page</u>
2-1	Schematic diagram of an OCT system .....	36
2-2	Schematic diagram of Michelson interferometer.....	37
2-3	Schematic diagram of wide-field microscope .....	43
2-4	Schematic diagram of confocal scanning microscope .....	44
2-5	Integrated endomicroscopy system from Pentax.....	52
2-6	Confocal endoscope probe from Manuna Kea Technologies .....	52
3-1	Structural views of a cantilevered bimorph beam. ....	57
3-2	Design concept and geometry schematic of the LSF-LVD actuator .....	62
3-3	TSV micromirror design.....	63
3-4	Process flow of the TSV micromirror .....	66
3-5	Static scan angle test result for the TSV micromirror.....	67
3-6	Static vertical displacement test result for the TSV micromirror.....	68
3-7	Frequency response test result for the TSV micromirror .....	68
3-8	Schematic of the endoscopic OCT system .....	70
3-9	3D model of the endoscopic OCT probe design .....	70
3-10	Photograph of the endoscopic OCT probe .....	72
3-11	2D cross-sectional OCT images by the endoscopic OCT system .....	73
3-12	3D cross-sectional OCT images by the endoscopic OCT system .....	73
4-1	Schematic diagram to illustrate the advantages of curved actuators with circular mirror plate.....	77
4-2	Schematic of design and SEM picture of the CCBA.....	78
4-3	Schematic and FEA simulation results of a curved bimorph.....	80
4-4	Schematic of the CCBA.....	82

4-5	3D plot of the center line of the CCBA.....	85
4-6	3D finite element model of the CCBA.....	86
4-7	Out-of-plane displacement of the CCBA vs. temperature change.....	86
4-8	Schematic design and SEM picture of Type I tip-tilt-piston mirror.....	87
4-9	FEM simulation results of Type I mirror.....	89
4-10	Schematic design and SEM picture of Type II piston-only mirror.....	90
4-11	3D finite element model of Type II mirror.....	91
4-12	Process flow of MEMS mirrors based on CCBA's.....	92
4-13	Type I Tip-tilt-piston mirror static measurement of piston movement.....	94
4-14	Type II piston-only mirror static measurement of piston movement.....	95
4-15	Type I Tip-tilt-piston mirror: scan angle vs. applied voltage.....	96
4-16	Frequency response of Type I tip-tilt-piston mirror.....	97
4-17	Frequency response of Type II piston-only mirror.....	98
5-1	Schematic of LSF-LVD based microlens scanner.....	101
5-2	SEM images of fabricated microlens scanners.....	102
5-3	Photos of assembled tunable microlenses.....	104
5-4	Photos of a tunable microlens driven at different voltages.....	104
5-5	Schematic design of the 2D CSM.....	105
5-6	SEM images of loaded and unloaded microlens scanner used in the 2D CSM.....	107
5-7	Static measurement of the microlens scanner used in the 2D CSM: vertical displacement vs. voltage.....	107
5-8	Frequency response of the microlens scanner used in the 2D CSM.....	108
5-9	Resolution measurement results of the 2D CSM.....	109
5-10	2D confocal reflectance image of micro-particles embedded in polymer taken by the 2D CSM.....	110

5-11	2D confocal reflectance image of rat skin taken by the 2D CSM.....	110
5-12	Schematic design of the 3D CSM.....	112
5-13	Photos and characterizations of the tunable microlens used in the 3D CSM. ..	113
5-14	Photos and characterizations of the 2D micromirror used in the 3D CSM.....	114
5-15	Characterizations of the 3D CSM system.....	116
5-16	Reflectance image of group 7 elements in a USAF resolution target by the 3D CSM.....	116
5-17	2D confocal reflectance images of micro-particles embedded in PDMS taken by the 3D CSM .....	118
5-18	A stack of Figure 4-17B~ Figure 4-17E with some particles labeled .....	119
5-19	3D volume-rendered image of micro-particles embedded in PDMS obtained by the 3D CSM .....	119
5-20	2D and 3D confocal reflectance image of rat brain tissue by the 3D CSM .....	120
5-21	System design of the 3D confocal scanning endomicroscope.....	122
5-22	3D endoscopic probe mechanical design .....	124
5-23	Optical design of the confocal endoscopic probe .....	125
5-24	Optical simulation results of the confocal endoscopic probe .....	126
5-25	SEMs and characterizations of the 2D ISC micromirror used in the endomicroscope .....	128
5-26	Photos and characterizations of the tunable lens used in the 3D confocal scanning endomicroscope.....	129
5-27	Photos of the assembled confocal endoscopic probe.....	131
5-28	System characterization results of the 3D confocal scanning endomicroscope. ....	132
5-29	2D and 3D confocal reflectance images of micro-patterns by the 3D confocal scanning endomicroscope.....	134
5-30	2D and 3D confocal reflectance images of micro-particles embedded in PDMS by the 3D confocal scanning endomicroscope .....	135

5-31	2D and 3D confocal reflectance images of onion skin by the 3D confocal scanning endomicroscope.....	136
5-32	2D and 3D confocal reflectance images of rat brain tissue by the 3D confocal scanning endomicroscope.....	137

Abstract of Dissertation Presented to the Graduate School  
of the University of Florida in Partial Fulfillment of the  
Requirements for the Degree of Doctor of Philosophy

LARGE-SCAN-RANGE ELECTROTHERMAL MEMS MICROMIRRORS AND  
MICROLENSSES AND THEIR BIOMEDICAL IMAGING APPLICATIONS

By

Lin Liu

May 2013

Chair: Huikai Xie

Major: Electrical and Computer Engineering

Emerging imaging technologies such as optical coherence tomography (OCT), confocal scanning microscopy (CSM), and nonlinear optical microscopy (NLOM) demonstrate powerful imaging performances and hold great promises to replace conventional biopsy for early cancer diagnosis. To realize in vivo optical imaging and optical biopsy, miniature endoscopy systems must be developed. The major challenges for endoscopic OCT, CSM and NLOM include the miniaturization of optical scan engines for both lateral and axial scans, the requirement of large scan range under low drive voltage, and the miniaturization of optics without largely sacrificing optical performance.

This dissertation presents a 2D electrothermal micromirror with through-silicon-vias (TSV) that provides large scanning angle ( $\pm 16^\circ$ ) and fast scanning speed (resonance at 659 Hz) at low voltage (less than 3.6 V). A time-domain endoscopic OCT system using the TSV micromirror for 2D beam scan has been developed. The TSV interconnection together with an ultra-compact probe design reduces the probe size to only 2.6 mm in diameter.

A new curved concentric bimorph actuator (CCBA) has been developed to actuate circular micromirrors with improved area efficiency, while achieving large scan range at low drive voltage. Two mirrors based on CCBA actuators have been designed and fabricated. Type I tip-tilt-piston micromirror is capable of scanning  $\pm 11^\circ$  at 0.6 V, and generating a 227  $\mu\text{m}$  piston displacement at only 0.8 V. Type II piston-only micromirror generates large vertical displacement of about 200  $\mu\text{m}$  at 0.9 V.

Multiple designs of electrothermal microlens scanners and focal tunable microlenses driven by such scanners have been developed. The microlens scanners are able to actuate microlenses with large tunable ranges from hundreds of microns to 1 mm at 5 V or lower. Three generations of CSM systems have been developed based on the MEMS focal-tunable microlenses. A 2D CSM using a MEMS focal-tunable microlens for large-tunable-range depth scan and a motor-driven stage for lateral scan has been designed. Then, a free-space 3D CSM using a MEMS focal-tunable microlens for axial scan and a 2D micromirror for lateral scan has been experimentally demonstrated. Last, a fiber-optic 3D confocal scanning endomicroscope with a 3D MEMS scan engine, a high-performance optical system design and a compact endoscopic probe has been developed.

## CHAPTER 1 INTRODUCTION

Cancer is one of the most common causes of death and it accounts for nearly a quarter of deaths in the US. American Cancer Society estimates about 577,190 deaths of cancer and 1,638,910 new cancer cases in the US for the year 2012 [1]. The survival rate of many cancers, including cancers of the breast, cervix, rectum, colon, oral cavity, skin and prostate, can be drastically increased if they can be diagnosed at an early stage. For example, breast cancer, the second leading cause of cancer death in women in 2012, has a survival rate of 99% if diagnosed at localized breast cancer stage [1]. The incidence rate of colorectal cancer, the third most common cancer in the US, has been decreasing for the past decade, which is largely attributed to the diagnosis and removal of precancerous polyps due to the improved use of colorectal cancer screening [2]. Although new treatment methods are emerging for cancers at advanced stages, the treatment at the point is typically very expensive and traumatic to patients. Successful methodologies for early stage cancer detection, therefore, are critical in reducing the morbidity and mortality of cancers.

### **1.1 Conventional Cancer Diagnosis Methods and Their Limitations**

Biopsy followed by *ex vivo* histological analysis is the traditional way for cancer diagnosis, but poses many shortcomings for the patient. This invasive diagnosis method involves bleeding, infection from tissue sampling, may cause complications from anesthesia, and may spread the tumors from the mechanical agitation [3]. Besides, random biopsy or biopsy without guiding by proper imaging is highly likely to miss invasive part of a tumor and result in an underestimation of the invasion and thus an inaccurate diagnosis. The current biopsy endoscopes are often equipped with white

light cameras to guide the biopsy, which can only visualize the surface morphology of tissue but not the precancerous lesion under the surface. Other than these, the delay time for diagnosis, and the added cost and risk are also the issues of this invasive diagnosis method.

Non-invasive imaging methodologies have been intensively studied to aid the cancer diagnosis. Computed tomography (CT), magnetic resonance imaging (MRI) and ultrasound are macroscopic non-invasive imaging systems that are currently in wide clinical use. However, these clinical imaging technologies do not provide sufficient resolution for the detection of many important pathology abnormalities of precancerous lesions based on the lesion anatomy, such as early stage neoplastic changes and coronary plaque predisposed to rupture [4]. An overview of the imaging systems under clinical use is summarized in Table 1-1 [5]. In order for non-invasive cancer diagnosis methodologies to replace conventional biopsy, micrometer-scale resolution has to be realized to resolve the clinically relevant microstructures that are resolvable by conventional biopsy.

Table 1-1. Overview of imaging systems

Technique	Typical Resolution	Depth	Time	Quantitative
MRI	500 $\mu\text{m}$	No limit	Minutes to hours	Yes
CT	1 mm	No limit	Minutes	Yes
Ultrasound	100 $\mu\text{m}$	mm	Seconds to minutes	Yes
PET	1-2 mm	No limit	Minutes to hours	Yes
SPECT	1-2 mm	No limit	Minutes to hours	Yes

## 1.2 Emerging Biomedical Imaging Technologies

New imaging technologies are emerging that hold great promises for early cancer detection, such as optical coherence tomography (OCT), confocal scanning microscopy (CSM), and nonlinear optical microscopy (NLOM). Unlike conventional

histopathology that requires the invasive biopsy, these non-invasive imaging methodologies can be used together with catheters and endoscopes to enable *in-vivo* real-time imaging of inner organs, can be applied where standard biopsy is hazardous or impossible, can reduce the sampling errors from biopsy, and can be employed to guide surgical procedures.

OCT is a fast developing technology capable of high-resolution, high contrast cross-sectional imaging of biological tissues [6]. OCT acquires cross-sectional images by measuring the echoes of backscattered light by low-coherence interferometry. It has been widely used for medical imaging in eye and skin diseases due to its high resolution (<10  $\mu\text{m}$ ) and noninvasive nature [7-12]. Endoscopic OCT has also been demonstrated to be very useful in examining internal organs [4] and has been successfully applied in many applications including gastrointestinal endoscopy [13, 14], urology [15-17], gynecology[18-20], and laryngology [21, 22], etc. The image penetration depths of OCT reach over 2 cm in transparent tissues like eye and embryo [23-25], and 2-3 mm in highly scattering bio-tissues [26, 27]. The principles and designs of OCT are described in more details in Chapter 2.

CSM, first proposed by Minsky in 1955 [28], revolutionized the optical microscopy by introducing point-by-point illumination and pinhole filtering to effectively increase contrast and resolution and also enable optical sectioning. By illuminating the sample from a point source at a single diffraction-limit point at a time, confocal microscopy avoids most of unwanted light from outside the focal volume that obscures the image at focal point. Additionally, back-reflected and back-scattered light from the sample will pass a pinhole conjugate to the focal point and the point source, which would further

reject the light not from the confocal volume [29, 30]. By suppressing the stray background light through the pinhole, the contrast of confocal microscopy is greatly enhanced compared to the wide-field microscopy. Additionally, the capacity of confocal scanning microscopy to image thin slice of tissue, called “optical sectioning”, enables 3D confocal imaging.

Confocal endomicroscopy is an imaging technology that extends the ultrahigh microscopic resolution, high contrast, and optical sectioning ability of the CSM to *in vivo* imaging. The conventional way for tumor cells grading is histopathology analysis of cellular shape, size, mitotic figures, etc from the biopsy samples [3]. With confocal endomicroscopy, the diagnosis of precancerous lesions and the grading of tumor cells could be performed *in-vivo* by optical biopsy instead of excisional biopsy. The cellular, nuclear and structural morphologic features can be visualized in living tissues with a lateral resolution of 0.5 to 3  $\mu\text{m}$ , a depth resolution of 3 to 9  $\mu\text{m}$ , and an imaging depth of 200 to 500  $\mu\text{m}$  [3]. *In-vivo* confocal microscopic imaging of skin, retina, liver, cornea, kidney, stomach and bladder tissues [31-42] has been demonstrated by many researchers. The details of the CSM and the confocal endomicroscopy including the principles and properties are elaborated in Chapter 2.

NLOM is another optical imaging methodology that has rapidly developed in the past few decades. Since the invention of the two-photon fluorescence microscopy in 1990 [43], imaging techniques based on nonlinear optical effects have begun to draw attentions for the inherent optical sectioning capacity and the ability to image at deep depth. While the linear optical microscopy is based on single-photon processes in which the light-matter interactions linearly depends on the incident light intensity, the nonlinear

optical microscopy deals with multi-photon processes that leads to high-order light-matters interactions. The major nonlinear optical effects include multi-photon absorption, coherent anti-stoke Raman scattering (CARS), and higher order harmonic generation [44]. The induced polarization of the matter subject to the vector electrical field of interaction light is given by [45]:

$$P = \chi^{(1)}E + \chi^{(2)}E^2 + \chi^{(3)}E^3 + \dots + \chi^{(n)}E^n$$

, where  $\chi^{(n)}$  is the  $n^{\text{th}}$  order susceptibility tensor. The linear susceptibility  $\chi^{(1)}$  represents the absorption and reflection of light in light-matter interactions. The second order susceptibility tensor  $\chi^{(2)}$  corresponds to second harmonic generation (SHG), and the third order susceptibility tensor  $\chi^{(3)}$  contributes to third-order processes including third harmonic generation (THG), two-photon absorption, and coherent anti-stoke Raman scattering (CARS).

In two-photon excited fluorescence (TPEF), since the cross-section of two-photon excitation is about 40 orders smaller than that of single-photon excitation [46,47], a near-infrared femtosecond pulsed laser with high instant power is typically used to excite the fluorescence at localized space and time. The TPEF is localized at the focal volume and will drop off quickly when getting away from the focal volume, therefore achieving highly resolution, high contrast, and inherent optical sectioning without the pinhole [48]. Besides, the deep penetration of the infrared light and the wide-field detection enable TPEF image deep into tissue [49, 50]. SHG microscopy is another popular nonlinear imaging technology, in which ultrashort laser pulses induce two

photons to produce a photon with exactly twice the frequency of the incident photons via a coherent harmonic up-conversion process [51-53].

### 1.3 MEMS-Based Endoscopy

To develop miniature endoscopy systems suitable for *in vivo* optical imaging and optical biopsy have been a goal for long. Although fast progress has been made in the past decades, several major challenges still exist for the *in vivo* endoscopic OCT, *in vivo* confocal endomicroscopy, and *in vivo* nonlinear optical endoscopy. The challenges common to all optical endoscopy include:

- Light scan mechanisms that allow for sufficient miniaturization to millimeter scale as well as fast, large-range scan at low voltages. The light scanning mechanism is the crucial issue and bottle-neck technology for many endoscopic systems.
- Endoscope probe designs with great mechanical flexibility and compact size in order to access the internal organs. The diameter requirement ranges from less than one millimeter to several millimeters and the rigid length from millimeters to several centimeters.
- Optical design based on micro-optics with adequately high optical performances.

Particularly for *in vivo* nonlinear optical endoscopy, it requires an efficient media to deliver the ultra-short laser pulses to bio-samples and collect the small nonlinear signal to detection. Photonic crystal fiber proves to be a good choice that can guide the ultrashort laser pulses without significant temporal and spectral broadening due to the group velocity dispersion and self-phase modulation shown in regular fiber [54]. The pulse broadening will result in large nonlinear excitation efficiency drop and penetration depth reduction [55, 56]. Besides, a scan mechanism that can achieve not only fast and large-range lateral scan but also depth scan is highly desirable, since the inherent optical sectioning capability of nonlinear optical microscopy needs to combine with the depth scan for 3D image formation.

The particular challenges for confocal endomicroscopy include the miniaturizations of both lateral and axial scan engines to realize 3D *in vivo* confocal imaging. The automatic axial scan is desired to fully employ the optical sectioning capacity of CSM as well as add the 3D imaging and diagnosis. In addition, micro-optics design with high optical performance is also necessary.

Endoscopic OCT requires proper imaging optics with both proper depth of focus and sufficient lateral resolution. Specifically for optical coherence microscopy (OCM), high NA objective is needed to generate microscopic resolution, and meantime depth scanning mechanism with sub-millimeter to millimeter scan range is required to compensate the small depth of focus.

Beam scanning mechanisms that have been adopted in optical endoscopy include scanning at proximal end across a fiber bundle [57-61], rotating or translating fiber or other optical elements by motors at the proximal end [62-64], vibrating the tip of a single fiber at the distal end [65-70], and scanning light beam at the distal end by MEMS-based scan engines [71-89].

Using the fiber bundle avoids the scan at the distal end, therefore simplifying the miniaturization of the image head. Fiber bundle has been used for confocal endoscopy and nonlinear optical endoscopy [57-61]. However, since the fiber cores are spatially separated by the claddings, the image plane is sampled at discrete points. The limitations are the inherent pixilation artifact of fiber bundle because of the spacing between fibers, the compromise among the sampling, the photo-efficiency and the resolution, and the leakage of light to adjacent fibers that would reduce the imaging contrast [90, 91].

Slow scan is a common issue for proximal end motor-based scan because of the friction or vibration of external motors. For example, a linear scanning probe by a galvanometer translates a distal fiber tip at up to 30 Hz and is limited to one-dimensional scan [62]. A forward-view OCT probe with a pair of angled GRIN lenses and two dc motors rotating at the proximal end scans at only 21 rpm [63]. A circumferential scanning OCT probe using a fiber optic rotary joint as the scanning mechanism has a low scan speed of only a few Hz [64].

Fiber distal vibration by piezoelectric or electromagnetic element has been applied to confocal endoscopy, nonlinear optical endoscopy and endoscopic OCT [65-70]. The drawbacks of this scanning mechanism are coupling non-uniformity and coupling loss especially at large angle.

Optical beam scan employing MEMS scanners provides an option to continuously scan beam at high speed and large range with high stability, uniform coupling and multidimensional scan capability. Meantime MEMS scanners can be miniature enough to fit into the endoscopes.

Miniature MEMS scanners and their applications in CSM, NLOM and OCT have been extensively studied and reported. Maitland *et al.* and Shin *et al.* reported confocal microscopes using 2D MEMS mirrors for the lateral scan [71, 72], but the depth scan was absent. MEMS-based confocal microscopes capable of 3D scan have been reported [73-76]. However, the systems reported in [74-76] relied on external motors and sliding stages for the axial scan. The instability from friction and the tradeoffs between size, speed and cost are the potential challenges of using external motor-based axial scanners. Jeong *et al.* presented a 3D dual-axis confocal microscope using

a pair of electrostatic MEMS mirrors, with the 2D mirror for the lateral scan and the 1D mirror for the depth scan. However, the axial displacement was only 10  $\mu\text{m}$  at 200 V dc or  $\pm 27.5 \mu\text{m}$  at resonance (4.69 kHz) under an ac voltage from 0-180 V [73]. The static displacement was too small even at high voltage, while at resonance, the frequency was too high for the axial scan. A miniature scanning system that can scan in both lateral and axial directions with large range, high speed, low drives and high stability is still missing. To develop such 3D scanning system is an objective of this research.

Nonlinear optical endoscopic systems based on MEMS mirrors have also been widely reported [77-83]. The 3D system reported in [79] is the only one that reported the depth scan of nonlinear optical endoscopy but the depth scan is achieved by an external 1D translation stage. An automatic depth scan mechanism is highly desired for nonlinear optical endoscopy.

MEMS-based OCT endoscopic probes with diameters ranging from 2.8 mm to 6 mm have been reported [84-89]. However, for endoscopic imaging of some internal organs such as human esophagus, further miniaturized probes are needed so that they can fit into the 2.8 mm biopsy channels of standard GI endoscopes [92]. Further miniaturization could be achieved by MEMS mirrors with higher fill factor, smaller chip size, space-saving electrical interconnection, or more compact probe design.

## **1.4 MEMS Optical Scanners**

### **1.4.1 MEMS Micromirrors**

Microelectromechanical system (MEMS) micromirrors have been applied to many different areas such as projection displays, optical switches, barcode readers, endoscopic biomedical imaging, Fourier transform spectrometers, tunable lasers, and adaptive optics [93-102]. The tip-tilt motion of MEMS micromirrors is useful for one-

dimensional (1D) or two-dimensional (2D) scanning for biomedical imaging [93, 94], optical displays [95], optical switches [96], barcode readers [97], etc. The Piston scan motion of micromirrors is desired in such applications as wave-front shaping in adaptive optics [98], tunable lasers [99], Fourier transform spectrometers [100,101], and spatial light modulators [102], etc. Scan range, driving voltage, bandwidth, fill factor, power consumption, footprint, repeatability and reliability are the general performance parameters for MEMS micromirrors.

Major actuation mechanisms that have been widely used in MEMS micromirrors include electrostatic [103-120], electromagnetic [121-124], piezoelectric [125-131], and electrothermal [132-138].

The first MEMS micromirror ever reported was an electrostatic parallel-plate micromirror developed by K. E. Peterson in 1880 [103]. It used the electrostatic force between the mirror plate and electrodes underlying to generate an optical scan angle of  $\pm 2^\circ$  under 300 V. Parallel-plate electrostatic micromirrors recently reported achieved larger optical scan angle [104-109]. However, the inherent nonlinearity and tight pull-in limit in parallel-plate actuator makes it more suitable for applications where large force but small displacements are required. Comb-drive actuator, compared to parallel-plate actuator, exhibits larger force density, better stability and linear operation over large displacement. For optical beam scanner that requires angular rotation, vertical comb drive (VCD) is needed to generate the out-of-plane actuation. Yeh *et al.* reported a staggered vertical comb drive (SVCD) torsional actuator integrating poly-silicon movable fingers with bulk silicon static fingers [110]. Schenk *et al.* reported 1D and 2D micromirror driven by SVCD with asymmetric electrodes for the starting tilt and trench

filling for electrical isolation, and an optical scan angle of up to  $60^\circ$  were achieved with 20V at resonance [111]. Su *et al.* developed a 2D micromirror with single-crystal silicon flat mirror plate bonded to a poly-silicon comb drive actuator, and an optical scan angle of  $\pm 7.5^\circ$  was achieved [112]. Lee *et al.* reported a gimbaled micromirror based on SOI wafers with two device layers and a self-aligned SVCD that can generate  $\pm 9^\circ$  static optical deflection angle at 155V [113]. Patterson *et al.* developed an AVCD-based micromirror using photoresist reflow to form a photoresist hinge [114]. Xie *et al.* reported a Post-CMOS micromirror using a thin-film curved hinge to generate the initial tilt for angular vertical comb drive (AVCD) and it achieved an angular scan of up to  $\pm 4.7^\circ$  at 18 V [139]. Jun *et al.* present an assembled AVCD-based on SU8 tilting pillars for the initial tilting [115]. A gimbal-less 2D MEMS micromirror proposed by Milanovic *et al.* was driven by four orthogonally positioned SVCDs coupled to the mirror plate by mechanical links and rotation transformers [116-119]. The rotation transformer enabled the angular magnification and up to  $\pm 10^\circ$  static angle was achieved under voltage less than 150 V. Tsai *et al.* also developed a gimbal-less micromirror with hidden radial VCD and cross-bar springs fabricated by SUMMiT-V surface micromachining process [120].

High speed and low power consumption are the major advantages of electrostatic actuators, but the high driving voltage and relatively small fill factor due to the large area occupied by comb drives limit the applications of electrostatic mirrors in certain fields such as endoscopic imaging. Besides, electrostatic micromirror is often operated at resonance to generate sufficient scan angle, which causes non-linear beam transfer characteristic, image distortion and difficulty in signal processing.

Electromagnetic actuation, on the other hand, can achieve large displacement and large force at low voltage. The Lorentz force of a current carrying coil in a magnetic field is utilized to actuate the mirror plate. Miyajima *et al.* developed a polyimide-hinged 1D micromirror with a pair of permanent magnets and a driving coil to achieve up to 60° at resonance frequency of 72 Hz [121]. Yalcinkaya *et al.* present a 2D micromirror with the magnetic field oriented at 45° to the slow and the fast axis, and large scan angles of 65° and 53° were achieved for the two scan directions [122]. Ji *et al.* reported a 2D micromirror driven by radial magnetic field that achieves a scan angle up to 8.8° [123]. A concentric permanent magnet pair and an electroplated coil were used to generate the magnetic actuation force. Yang *et al.* reported a coilless micromirror that utilized the eddy current to produce the Lorentz Force and achieved 20° scan angle at resonant under input 9 mW power [124].

Electromagnetic micromirrors reported usually involved either external magnets and/or on-chip coils. The bulky external magnet is an obstacle for the miniaturization and it also complicates the packaging, therefore limiting the applications of electromagnetic micromirrors to endoscopic imaging. The introduction of on-chip coils involves complicated coil routing, Joule heating problem and high power consumption.

Piezoelectric actuation began to be applied to micromirror as the thin film piezoelectric materials developed to an applicable state [140-147]. Yee *et al.* reported a piston-motion micromirror actuated by PZT cantilever unimorph actuators for tracking of optical data storage application [125]. Tsaur *et al.* developed a 2D micromirror driven by double layered PZT actuators derived by sol-gel method [126]. Filhol *et al.* demonstrated a 1D torsional micromirror excited to high-frequency resonances by

piezoelectric bimorphs [127]. Koh *et al.* reported a 2D micromirror excited by S-shaped PZT actuators [128]. Park *et al.* reported a 1D piezoelectric micromirror based on a thick PZT film using aerosol deposition method (ADM) [129]. Tani *et al.* demonstrated a 2D piezoelectric micromirror driven by cantilever PZT unimorphs cascade in a meandering shape to accumulate angular displacement [130]. Zhu *et al.* demonstrated a tip-tilt-piston micromirror with minimized lateral shift and high form factor using a folded-structured cantilever PZT unimorph actuator [131]. Large bandwidth and low power consumption make piezoelectric actuators very attractive, but charge leakage, hysteresis, and toxicity set additional challenges.

Electrothermal actuators can provide large displacement and force at low voltage and achieve relatively high fill factor. Various bimorph-based electrothermal MEMS mirrors with different materials and fabrication processes have been reported. For example, Buser *et al.* demonstrated a biaxial scan mirror driven by Al/Si bimorphs with an IC-compatible fabrication process [132]. Buhler *et al.* proposed electrothermal micromirrors with Al/SiO<sub>2</sub> bimorph actuators fabricated by a standard CMOS fabrication process [133]. Jain *et al.* reported both 1D and 2D micromirrors based on Al/SiO<sub>2</sub> bimorphs fabricated using a DRIE CMOS-MEMS process [134]. Singh *et al.* reported an electrothermal micromirror driven by Al/Si bimorph actuator capable of generating 17° scan angle at less than 2 V [135]. Wu *et al.* demonstrated a folded lateral-shift-free electrothermal actuator based on Al/SiO<sub>2</sub> bimorphs which was fabricated on an SOI wafer with a combined surface- and bulk- micromachining process [136]. The tip-tilt-piston micromirror with a mirror plate of 1 mm by 1 mm achieved a piston displacement of 0.6 mm under 5.5 V and a static optical scan angle of ± 30° at less than 5 V. Jia *et al.*

presented a TTP micromirror actuated by a fold dual S-shaped Al/ SiO<sub>2</sub> bimorphs [137]. Kim *et al.* demonstrated a micromirror rotated by a twisting-type actuation system comprised of two parallel Ni/SiN<sub>x</sub> bimorph beams bending in opposite directions [138].

Although electrothermal micromirror has the drawbacks of relatively high power consumption and slow response, it also exhibits outstanding advantages. The large force and large displacement generated by small voltages are highly desired by endoscopic applications which favor large scan range as well as safe operation voltage inside human body. It also comes with simpler fabrication process with lower cost compared with electrostatic vertical comb drive actuators, easier packaging and compact size compared to electromagnetic actuators, hysteresis-free and toxicity-free materials compared with piezoelectric actuators. Besides, it allows for high fill-factor and large mirror aperture that can potentially enable further miniaturization for endoscopy. These advantages make electrothermal micromirror an ideal choice for biomedical imaging applications, especially for endoscopic imaging applications, where the power consumption is not critical and speed requirement is within the achievable range of electrothermal micromirrors.

#### **1.4.2 MEMS Microlens Scanners**

Besides MEMS micromirrors, MEMS focal-tunable microlens is also an important research field in optical MEMS. MEMS focal-tunable microlens is capable of dynamic tuning of focus, which is highly desired by many applications in modern optics.

Adaptive and tunable optical components and systems have been a very active study area of optics for years [148]. Their various applications including correcting the light disturbed by atmosphere in astronomical telescopes [149], enhance retinal imaging resolution and quality for human eyes [150], the autonomous focus for cameras and

adaptive zoom lens [151,152], focal depth scanning for microscopy and other biomedical imaging modalities [153-156], focus adjustment and optimization for optical data storage [157,158], and varifocal lens for display system [159], etc. The adaptive optical components can be deformable mirrors for wave-front aberration correction, or focal tunable lens for dynamic focusing of light when it goes out-of-focus.

Conventional optical systems accomplish the focus adjustment by moving glass lenses using bulk mechanical components. To downscale such tunable lens systems for miniature optical applications is limited by fabrication techniques and friction from the mechanical movement especially when surface-to-volume ratio increases [151].

Two major types of tunable microlens under active studies are liquid or polymer micro-lenses with deformable shape, and microlens physically displaced by actuators. The liquid or polymer tunable lenses have deformable shapes that can be changed by electrowetting [151, 160, 161], pneumatic actuation [162], hydraulic actuation [163, 164], liquid crystal [159, 165] or hydrogels [166]. The focal length is varied as shape/curvature of microlens is changed, and large tunable range of a few millimeters could be achieved.

However, liquid or polymer microlenses have large driving voltages and/or large size and very slow response time. Large actuation voltages over 100 V are required by electrowetting, which raises safety issues for some applications such as endoscopic imaging. The response is typically very slow in the range of seconds that pose problems for applications that require fast operation such as dynamic tracking for optical disks. Some complex or bulky components may be involved, such as the external pumping components for hydraulic driven liquid lens, introduce extra difficulty for miniaturization and system integration. Also severe optical distortion may be introduced in liquid crystal

or electrowetting actuation which needs electrodes immersed in electrolyte solution [167]. Aberrations may also be introduced when changing the shape of the lens, which will deteriorate the image quality. Besides, the numerical aperture changes when the focal length is tuned, leading to varying imaging performance along the adaptive focal path. All these factors make deformable liquid or polymer lens not a good choice for endoscopic microscopy which required high image quality and consistent imaging performance along the scan path.

Tunable microlenses physically displaced by actuators have also been developed [154, 155, 168-171]. Kwon *et al.* reported a two-dimensional stacked microlens-scanner for confocal imaging array that can actuate the microlens laterally in x- and y- directions for 75  $\mu\text{m}$  at resonance [170]. The same group also reported a z-scan microlens scanner actuated by electrostatic vertical comb drive that achieved up to 55  $\mu\text{m}$  at a resonance frequency of 400 Hz [172]. Gorecki *et al.* demonstrated a confocal microscope using a 3D stacked on-chip MEMS microlens scanner. The electrostatic parallel-plate z-scanner was able to scan up to 100  $\mu\text{m}$  [173]. Gokce *et al.* developed a microlens array vertically sitting on a 2D comb-drive actuator with one dimension scan in x-direction and one dimension in z-direction. They reported a 124  $\mu\text{m}$  in-plane scan range and a 34  $\mu\text{m}$  out-of-plane scan range [173]. Jain *et al.* demonstrated a LVD-electrothermal actuator integrated with photoresist reflow microlens to generate up to 280  $\mu\text{m}$  depth scan [153,171]. Lei *et al.* proposed a LSF-LVD electrothermal actuator integrated with a glass microlens for a large vertical tunable range of 0.88 mm [174]. Electrothermal actuators provide smaller tunable range than the pneumatic actuation but the response time is much faster. When

compared with electrostatic driven tunable microlens, electrothermal actuators offer larger actuation range under small voltage, and also less complex fabrication and assembly.

### **1.5 Research Objectives**

The objectives of this research are to develop MEMS micromirrors and microlenses and to explore their applications in various biomedical imaging fields including endoscopic OCT, CSM and NLOM for *in vivo* cancer diagnosis. More specifically, the research objectives are listed as follows:

First, to design, fabricate and characterize 2D MEMS micromirrors with small footprint, large scan range, low driving voltage, high scan speed, and precise position control.

Second, to push the limit of the miniaturization of endoscopic probes by using a unique through-silicon-via (TSV) electrical interconnect in micromirror; and to develop an endoscopic OCT system and a compact probe design that integrate the TSV micromirror, a fiber and micro-optics to realize high-performance *in vivo* OCT imaging.

Third, to develop curved bimorph actuators and micromirrors based the curved concentric electrothermal actuators; and to explore the feasibility of employing curved actuators to improve the form factor and area efficiency of micromirrors and to study the actuation characteristics of curved electrothermal actuators.

Fourth, to develop tunable microlens scanners with small footprint, large tunable range, low driving voltage, high scan speed, and stable actuation; and to integrate microlens scanners with microlenses to form focal-tunable microlenses and to perform depth scan for microscopic imaging.

Fifth, to design and construct MEMS-based 2D and 3D CSM systems and confocal endomicroscope systems; to achieve automatic large-range lateral and axial scan under low driving voltage with the 2D MEMS micromirror and 1D MEMS tunable microlens; and finally, to integrate MEMS scan engines, optical fiber and miniature optics into compact endoscopic probes for *in vivo* imaging.

## 1.6 Dissertation Overview

There are six chapters in this dissertation. Chapter 1 reviews the background and introduces the motivation of this project, including the conventional cancer diagnosis methods, the emerging imaging techniques, the state-of-the-art MEMS-based endoscopy and MEMS optical scanner. Chapter 2 presents in details the principles of optical coherence tomography and confocal scanning microscopy, the two major optical systems that the author will develop in this dissertation. In Chapter 3, the principle, design, fabrication and characterization of electrothermal micromirror with TSV will be presented, followed by the demonstration of the endoscopic OCT system that employs the TSV micromirror for *in vivo* imaging. Then in Chapter 4, two types of MEMS micromirrors based on a curved concentric electrothermal actuator will be introduced, including the motivation, the design concept, the analytical results, the finite element simulation results, the fabrication, and the characterization. Chapter 5 focuses on several MEMS tunable microlens designs developed and the confocal scanning microscopic imaging systems based on the developed tunable microlenses. The confocal scanning microscopic imaging systems will be described from the 1<sup>st</sup> generation 2D CSM system in which only MEMS-scanner is used, to the 2<sup>nd</sup> generation 3D CSM system using both a MEMS micromirror and a MEMS tunable microlens for 3D scan, and finally to the 3<sup>rd</sup> generation confocal scanning endomicroscope system with

3D full-MEMS scanning system, high-performance micro-optics and a miniature endoscopic imaging probe. Finally, the entire research work and accomplishments are summarized in Chapter 6, together with the outlook for future work and potential research opportunities following this research.

## CHAPTER 2 EMERGING BIOMEDICAL IMAGING METHODOLOGIES

As discussed in Chapter 1, Biopsy followed by *ex vivo* histological analysis, as the traditional way of cancer diagnosis, has many shortcomings and needs to be replaced by alternative advanced technologies. The widely used clinical imaging technologies such as CT, MRI and ultrasound couldn't meet the requirements for *in vivo*, noninvasive cancer diagnosis because of their insufficient resolutions. Some emerging imaging technologies including OCT, CSM and NLOM stand out as promising solutions for optical biopsy and *in vivo* cancer detection. In this chapter, we will study the working principles, major properties and design considerations of OCT and CSM. The fundamentals of OCT and CSM will be used as guidance for the MEMS-based imaging system design and instrumentation.

### **2.1 Optical Coherence Tomography**

#### **2.1.1 Principles of OCT**

OCT is an emerging non-invasive imaging technology that generates high-resolution, high-contrast cross-sectional images of tissues. OCT is analogous to ultrasound B mode imaging except that light instead of sound is used for imaging. OCT typically has much higher spatial resolutions than ultrasound. The typical spatial resolution of clinical ultrasound system is as fine as 150  $\mu\text{m}$ , which is determined by the frequency of the sound waves, while the spatial resolutions of 1-15  $\mu\text{m}$  can be achieved by OCT [175]. The penetration depth of ultrasound, however, is higher than OCT. The typical clinical ultrasound imaging system can generate images up to several tens of centimeters deep. However, for ultrasound there exists a tradeoff between the spatial resolution and the penetration depth. High frequency ultrasound (100 MHz or higher)

with enhanced spatial resolution faces strong attenuation in bio-tissues and limited penetration depths of a few millimeters [175]. The image penetration depths of OCT reach over 2 cm in transparent tissues like eye and embryo [23-25], and 2-3 mm in highly scattering bio-tissues [26, 27].

Similar to ultrasound, OCT measures the dimensions of different structures by detecting the echo time delay it takes for light to be backscattered from different depths of structures. However, since the velocity of light propagation is about a million times faster than that of sound propagation, the echo time delay of light couldn't be detected directly by electronics as in the case of ultrasound [175]. For example, the echo time delay for an OCT system with 10  $\mu\text{m}$  axial spatial resolution corresponds to a time resolution of about  $30 \times 10^{-5}$  sec, which is impossible for direct electronic detection.

Low-coherence interferometry is therefore introduced into OCT to detect the echo time delay. Low-coherence interferometry originated from optical coherence-domain reflectometry, a technique developed preliminarily for measuring the reflections and the faults locations in waveguides and optoelectronic components [176, 177].

A schematic diagram of a typical time-domain OCT system is shown in Figure 2-1. Low coherence light from a broad-band light source is coupled into a Michelson interferometer. The light is divided by a fiber-coupler into a reference arm and a sample arm. The Light backscattered from the sample and light reflected from a scanning reference mirror combines at the fiber coupler. The interferometric signal that contains the backscattered signal information is detected by a photo-detector, followed by data processing electronics, data acquisition, and image display.

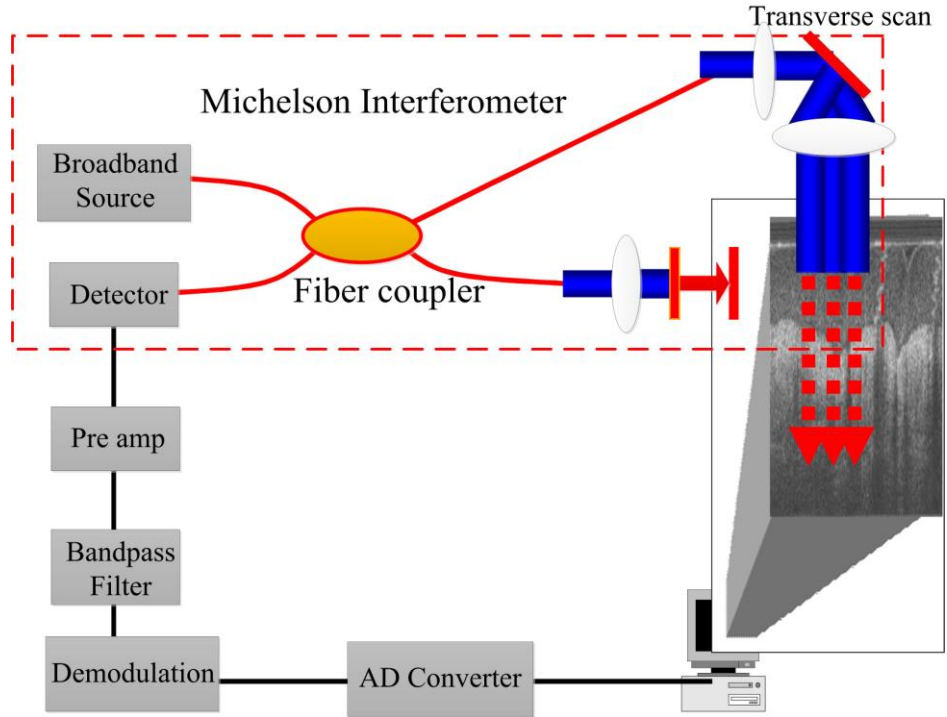


Figure 2-1. Schematic diagram of an OCT system

### 2.1.2 Theoretical Analysis and Imaging Parameters

To facilitate the analysis of the OCT signal, we consider a simplified schematic of the Michelson interferometer as shown in Figure 2-2. The single-path lengths of the reference arm and the sample are  $L_r$  and  $L_s$ , respectively. The electric fields of the reflected light from the reference mirror and the sample reflecting surface are  $E_r$  and  $E_s$ , respectively. For low coherence light source that contains a broad bandwidth of frequencies,  $E_r$  and  $E_s$  should be represented by the functions of frequency:

$$E_r(\omega) = A_r(\omega) \exp\{-j[2\beta_r(\omega)L_r - \omega t]\} \quad (2-1)$$

$$E_s(\omega) = A_s(\omega) \exp\{-j[2\beta_s(\omega)L_s - \omega t]\} \quad (2-2)$$

$E_r$  and  $E_s$  are combined at the beam-splitter and the electric field of the light signal after the beam-splitter is the sum of  $E_r$  and  $E_s$ . The detector responds to the average light intensity over the whole bandwidth of the light source and the photocurrent is given by [178]:

$$I_d = \left\langle \int_{-\infty}^{+\infty} \frac{dw}{2\pi} \frac{\eta e}{h\nu} \frac{|E_r(w) + E_s(w)|^2}{2\varepsilon_0} \right\rangle = \left\langle \int_{-\infty}^{+\infty} \frac{dw}{2\pi} \frac{\eta e}{2h\nu\varepsilon_0} \left[ |A_r|^2 + |A_s|^2 + \text{Re}(E_s(w)E_r(w)^*) \right] \right\rangle \quad (2-3)$$

$$I_d \propto \text{Re} \left\{ \int_{-\infty}^{+\infty} dw \left[ (E_s(w)E_r(w)^*) \right] \right\} = \text{Re} \left\{ \int_{-\infty}^{+\infty} dw S(w) \exp[-j\Delta\phi(w)] \right\} \quad (2-4)$$

, where  $S(w) = A_s(w)A_r(w)^*$  (2-5)

, and  $\Delta\phi(w) = 2\beta_s(w)L_s - 2\beta_r(w)L_r$  (2-6)

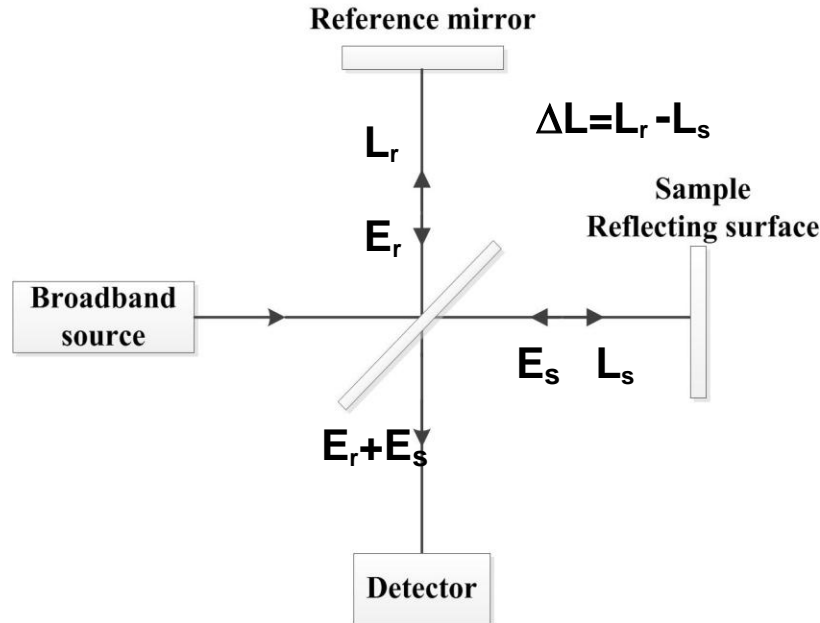


Figure 2-2. Schematic diagram of Michelson interferometer

$S(w)$  is the power spectrum of the light source.  $\Delta\phi(w)$  is the phase mismatch between the returning light from sample arm and the returning light from the reference

arm as a function of frequency. Consider a light source with a power spectrum of  $S(w-w_0)$ , a center frequency of  $w_0$  and a bandwidth of  $\Delta w$ . Assume the propagation constants of the sample arm and the reference arm are same and the light propagates in non-dispersive medium. The propagation constant can be expanded as first-order Taylor expansion as:

$$\beta(w) = \beta_s(w) = \beta_r(w) = \beta(w_0) + \beta'(w_0)(w-w_0) \quad (2-7)$$

Let the length difference between the sample arm and the reference arm:

$$\Delta L = L_s - L_r \quad (2-8)$$

The phase mismatch in Equation 2-6 is then determined only by  $\Delta L$ :

$$\Delta\phi(w) = \beta(w_0)(2\Delta L) + \beta'(w_0)(w-w_0)(2\Delta L) \quad (2-9)$$

The photocurrent  $I_d$  in Equation 2-4 then becomes:

$$I_d \propto \text{Re} \left\{ \exp[-jw_0\Delta\tau_p] \int_{-\infty}^{+\infty} \frac{d(w-w_0)}{2\pi} S(w-w_0) \exp[-j(w-w_0)\Delta\tau_g] \right\} \quad (2-10)$$

$$\text{, where the phase delay mismatch } \Delta\tau_p = \frac{2\beta(w_0)\Delta L}{w_0} = \frac{2\Delta L}{V_p} \quad (2-11)$$

$$\text{and the group delay mismatch } \Delta\tau_g = 2\beta'(w_0)\Delta L = \frac{2\Delta L}{V_g} \quad (2-12)$$

, where  $V_p$  and  $V_g$  are the phase velocity of the center frequency and the group velocity.

It can be seen from Equation 2-10 that the interferometric signal of the photocurrent includes an envelope and a carrier. The envelope is the inverse Fourier transform of the power spectrum and the carrier is a fringe signal oscillating with  $2\Delta L$  at a spatial frequency of  $\beta(w_0)$ .

For Gaussian power spectrum

$$S(w - w_0) = \sqrt{\frac{2\pi}{\sigma_w^2}} \exp\left[-\frac{(w - w_0)^2}{2\sigma_w^2}\right] \quad (2-13)$$

, where  $2\sigma_w$  is the standard deviation power bandwidth

, the photocurrent in Equation 2-10 becomes:

$$I_d \propto \exp\left[-\frac{\Delta\tau_g^2}{2\sigma_\tau^2}\right] \text{Re}\left\{\exp[-jw_0\Delta\tau_p]\right\} \quad (2-14)$$

$$\text{, where } 2\sigma_\tau = \frac{2}{\sigma_w} \quad (2-15)$$

Equation 2-14 shows that for a Gaussian power spectrum source, the photocurrent is a carrier fringe signal with a Gaussian envelope function. Besides, the standard deviation temporal width of the Gaussian envelope is inversely proportional to the bandwidth of the source power spectrum as shown in Equation 2-15. The Gaussian envelope determines that the interference fringes are detected only when the group delay mismatch is within the standard deviation temporal width of the Gaussian envelope:

$$\beta'(w_0)(2\Delta L) \leq 2\sigma_\tau \quad (2-16)$$

The standard deviation axial resolution, therefore, can be derived as:

$$\Delta L_\sigma = \frac{1}{\beta'(w_0)\sigma_w} = \frac{v_g}{\sigma_w} \quad (2-17)$$

The full-width at half-maximum (FWHM) axial resolution of a Gaussian source with a FWHM bandwidth of  $\Delta\lambda$  can be derived as [178]:

$$\Delta L_{FWHM} = \frac{2 \ln 2 \lambda_0^2}{\pi \Delta \lambda} \approx 0.44 \frac{\lambda_0^2}{\Delta \lambda} \quad (2-18)$$

Equation 2-17 and Equation 2-18 show that the axial resolution is inversely proportional to the bandwidth of the source. Therefore, broadband light source is used in OCT in order to achieve high axial resolution.

From Equation 2-16 to Equation 2-18 we can also find that only when the optical path mismatch between the sample arm and the reference arm is smaller than the axial resolution can the interference fringes be seen by the photo-detector. This is the inherent optical gating properties of OCT that can exclude signal from depths other than the coherence gate being detected. The coherence gate greatly enhances the contrast of the OCT imaging. Besides, the reference arm can be used as the depth scanning reference to quantitatively measure the axial dimensions of samples.

After the photocurrent is detected by the photodetector, a series of data processing is required to extract the amplitude of the envelope signal.

Let the travel velocity of the reference scan mirror be  $V_r$ , then the carrier frequency of the electrical current signal can be derived from Equation 2-11 as:

$$\omega_d = \frac{2V_r \omega_0}{V_p} \quad (2-19)$$

The photocurrent is first converted into the voltage, and then a bandpass filter that centered at the carrier frequency is then used to extract the interferometric signal from the DC parts and the noise, and finally the envelope of the interferometric signal that contains the information of the backscattered light is extracted.

Another unique characteristic of OCT is that the axial and the transverse resolution are decoupled in OCT. The axial resolution is determined by the bandwidth of

the optical source, while the transverse resolution is determined by the focusing characteristics of the objective lens. High transverse resolution can be achieved by using an objective lens with a large numerical aperture. The transverse resolution is given by

$$\Delta x = \frac{4\lambda}{\pi} \frac{f}{D} = \frac{2\lambda}{\pi} \left( \frac{1}{NA} \right) \quad (2-20)$$

Where D is the spot size on the objective lens and f is the focal length of the objective.

The depth of focus (DOF) or the confocal parameter is another important parameter of OCT. DOF is the longitudinal distance within which the light beam is considered focused. The DOF of a Gaussian beam is given by:

$$DOF = \frac{\pi \Delta x^2}{2\lambda} = \frac{2\lambda}{\pi} \left( \frac{1}{NA} \right)^2 \quad (2-21)$$

Equation 2-20 and Equation 2-21 imply that the improvement of transverse resolution is always at the expense of sacrificing the DOF. Since the penetration depths of OCT in most bio-tissues are about 2-3 mm, the DOF should also fall in this range to guarantee that the spot size is small and the image quality is consistent through the whole penetration depth. A balance between the transverse resolution and the DOF needs to be reached. And instead of pursuing confocal microscopic scale high resolution, the NA of the objective lens in OCT is often limited ( $NA < 0.2$ ) to make the DOF greater than hundreds of microns. For instance, a DOF of 1 mm is achieved with a transverse resolution of about 30  $\mu\text{m}$  under a center wavelength of 1300 nm.

In order to reach high transverse resolution and large DOF at the same time, some novel methods have been developed to get cellular-level transverse resolution

OCT, also called optical coherence microscopy (OCM). OCM offers advantages for large imaging depth in highly scattering tissues compared to confocal microscopy, and high resolution compared to regular mode OCT. However, these advantages come at the price of higher requirement on optics quality and increased complexity on the instrumentation.

## **2.2 Confocal Scanning Microscopy**

### **2.2.1 Theory of Confocal Scanning Microscopy**

Confocal scanning microscopy, as a subset of the well-established microscopy, is one of the most important tools for biomedical imaging, materials study and semiconductor inspection, etc [[179-181]]. It has been well known for the high contrast microscopic imaging, very high sub-micron resolution, and the optical sectioning ability that enables 3D imaging. Various technologies have been developed in the field of microscopy to suppress the stray background light and enhance the contrast. For instance, fluorescence microscopy detects only the emitted fluorescence light with shifted frequency than the excitation light [182,183]. The phase contrast microscopy acquired only the light with retarded phase from passing through sample [184,185]. And for confocal microscopy, the contrast enhancing and background stray light suppressing are accomplished by the point illumination from a point source and the spatial filter by a pinhole detector conjugate to the focal point and the point source to screen out the light from outside the confocal volume [29].

The basic components of a conventional wide-field microscope are shown schematically in Figure 2-3. A light source and a condenser lens provide uniform illumination on the sample, known as bright-field imaging. A high-performance objective generates an inverted, real intermediate image of the object inside the tube. The tube

length is typically made 160 mm from the shoulder of the objective. And the intermediate image is typically formed 150 mm from the shoulder and 10 mm inside the tube. The system shown in Figure 2-3 is an infinity-corrected microscopic system, where light is collimated after the objective lens, and a tube lens is added to form the intermediate real image 10 mm inside the tube. The ocular, also named as eyepiece, acts as an additional magnifier and also a relay to another image plane such as retina. The ocular produces a virtual image of the object at a suitable viewing distance for human eyes to observe. There are two sets of conjugate planes [29]: one set is the planes conjugate to the object (Object plane), the intermediate image (O+1), and the image (O+2); the other set is the planes conjugate to the pupil, including the lamp filament (P-2), the image of the lamp filament before condenser (P-1), the shoulder of the objective (Pupil plane), the pupil of retina or camera (P+1).

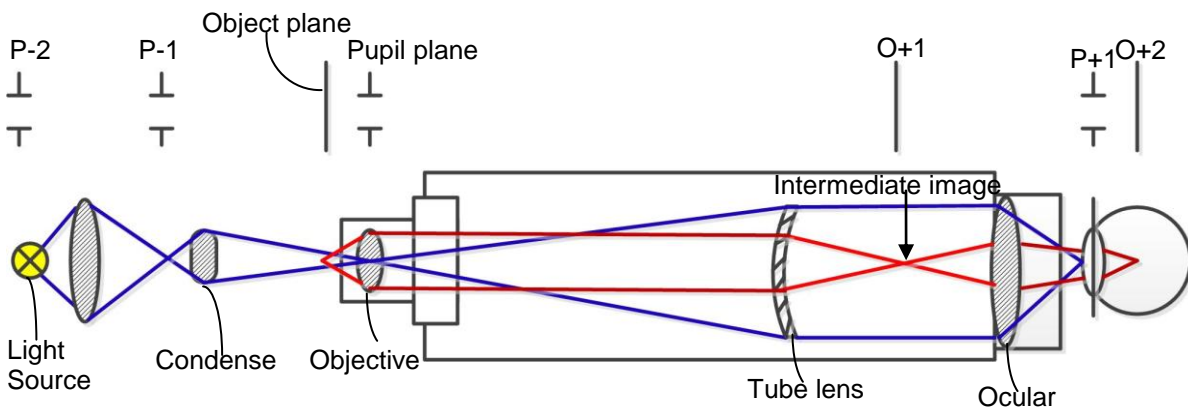


Figure 2-3. Schematic diagram of wide-field microscope

The confocal microscope differs from the wide-field microscope in that it illuminates and images only one point at the focal point per time and excludes light contributed from outside the focal volume from detector by a pinhole. Scanning mechanisms in transverse directions and axial direction have to be incorporated for

multiple points imaging and 2D and 3D images formation. As shown in Figure 2-4, a point light source or a light source spatially filter by a pinhole passes through an objective and forms a diffraction-limit light spot on the sample. The back reflected or scattered light is collected by the same objective and pass back through the pinhole before the detector. The point light source is imaged at the focal point by the objective so the point source and the focal point are conjugate. Meantime, the focal point is imaged by the optics to the pinhole, so the focal point and the pinhole are also conjugate. This means that the point source, the focal point and the pinhole are mutually “confocal”. This is how the name of confocal microscopy comes from.

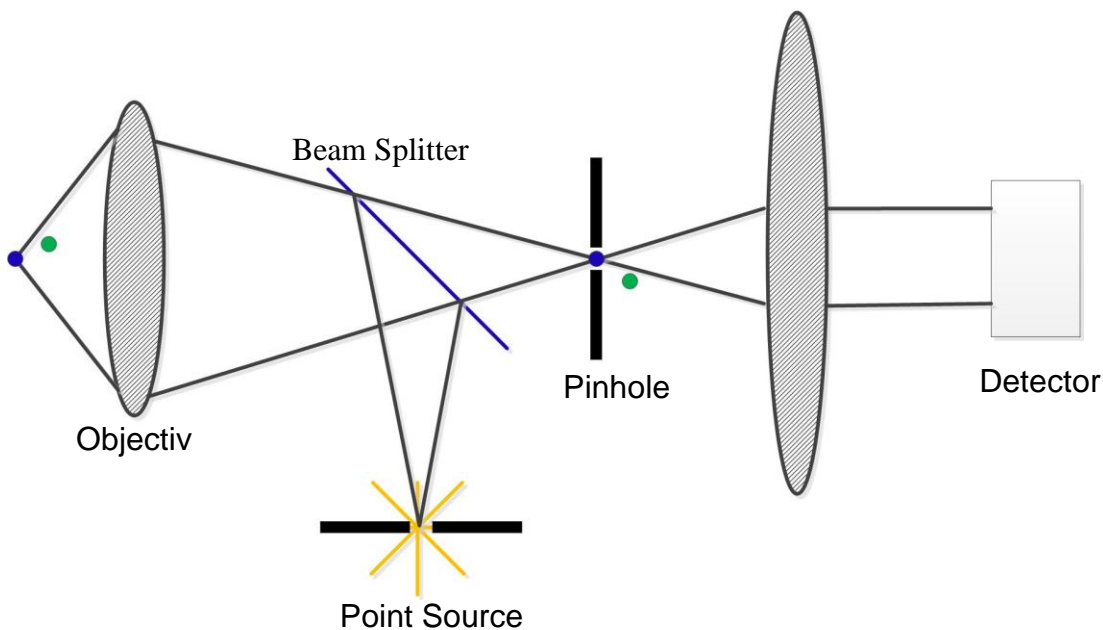


Figure 2-4. Schematic diagram of confocal scanning microscope

Different from the uniform illumination of the wide-field microscope, in confocal microscope the objects not in the focal volume may not be illuminated by the point light source. Furthermore, the objects outside the confocal volume will image at different points than the pinhole so most of the light from these objects will be screened out by

the pinhole from the detecting. Therefore, confocal microscope has the ability to collect the signal from only the confocal volume, suppress the stray background light from other points, and greatly enhance the image contrast of the each imaging points.

## 2.2.2 Imaging Properties

### 2.2.2.1 Resolution

The resolution of the microscopic systems is defined based on the point spread function (PSF), which is the response of an imaging system to a  $\delta$  (point) function. The diffraction effect determines that any lens will spread the image of a point object to a certain intensity pattern. For paraxial approximation, the amplitude PSF of a circular aperture at the focal plane is given by:

$$P(\rho) = \frac{J_1(\rho)}{\rho} \quad (2-22)$$

, where  $J_1$  is the Bessel function of the 1<sup>st</sup> kind,  $\rho$  is a radial variable perpendicular to the axis, also called optical unit or o.u.  $\rho$  is given by,

$$\rho(r) = \frac{2\pi nr \sin \theta}{\lambda} = rk \sin \theta \quad (2-23)$$

, where  $k$  is the wave number,  $\lambda$  is the wavelength and  $n \sin \theta$  is the numerical aperture (N.A.) of the lens.

For conventional wide-field microscopy that use incoherent light source, the phases of any points of the sample are uncorrelated, therefore the phase variations will be averaged to zero and the intensity instead of the amplitude would add at the detector. Therefore the intensity PSF instead of the amplitude PSF matters. The intensity PSF for a circular aperture can be expressed as:

$$I(\rho) = |P(\rho)|^2 = \frac{2J_1^2(\rho)}{\rho^2} \quad (2-24)$$

This is the diffraction pattern well-known as Airy disk with a central bright disk followed by dark and bright concentric rings surrounding the central disk. The radius of the Airy disk is defined as the radius of the first dark ring. The radius of the Airy disk  $r_{Airy}$  depends on the wavelength and the NA of the objective:

$$r_{Airy} = \frac{0.61\lambda}{NA} \quad (2-25)$$

Rayleigh criterion is a commonly used criterion to evaluate the resolution of an imaging system under the consumption of incoherent illumination. Rayleigh criterion considers two bright points as resolved if the distance between them is bigger or equal to the radius of the Airy disk. The lateral resolution of a conventional wide-field microscope by Rayleigh criterion is:

$$r_{Lateral} = r_{Airy} = \frac{0.61\lambda}{NA} \quad (2-26)$$

Under Rayleigh distance, the dip in between two bright peaks is about 26%. However, for the real imaging, there always exist noises. The 26% dip defined by Rayleigh criterion is not necessarily the line across which two separate bright points will be resolved or unresolved. When the noise level is low, a dip of 5% might be enough for two bright points to be distinguished. However, when the imaging system is very noisy, a 26% dip may not be enough for two points to be considered resolved. So the diffraction-limit resolution of an objective can be increased by increasing the NA of the objective, but the noise level limits the contrast level required and thereby limits the realizable resolution.

The axial resolution is customarily defined according to the 3D diffraction pattern of a point object, the 3D PSF. The PSF is actually a three dimensional function. The Airy disk is the cross-section of the 3D PSF at the focal plane. The PSF along the z axis under paraxial approximation is in the form of

$$I(\zeta) = \left( \sin\left(\frac{\zeta}{4}\right) / \frac{\zeta}{4} \right)^2 \quad (2-27)$$

, where  $\zeta$  is the o.u. along axis,

$$\zeta(z) = \frac{2\pi n}{\lambda} z \sin^2 \theta = zk \sin^2 \theta \quad (2-28)$$

The axial resolution can be defined similarly to the lateral resolution as the smallest distance between two points along the axis at which their images are resolved as two and quantified by the distance between the central peak and the first minimum along the axis:

$$z_{Axial} = \frac{2n\lambda}{NA^2} \quad (2-29)$$

The resolution of the confocal microscopy is different from the resolution of the conventional microscopy because their PSFs differ. The illumination of confocal microscopy, instead of being uniform on the sample, is at one point at one time. The amplitude of the light field at the sample is therefore given by the amplitude PSF of the objective,  $P(\rho, \zeta)$ . The same objective then images the focal point to the pinhole, which is also defined by the PSF of the objective. So the amplitude PSF of the system is given by  $P(\rho, \zeta) \times P(\rho, \zeta)$ . The intensity PSF of the confocal microscopy is the square of the amplitude PSF,

$$I_{con}(\rho, \zeta) = |P(\rho, \zeta)|^2 \times |P(\rho, \zeta)|^2 = I(\rho, \zeta) \times I(\rho, \zeta) \quad (2-30)$$

The fact that the intensity PSF of the confocal microscopy is the square of that of the conventional microscopy means that the PSF of the confocal microscopy is sharper than that of the conventional microscopy. Also the PSF of the confocal microscopy has suppressed subsidiary peaks.

The lateral resolution of the confocal microscopy following the 26% dip from the Rayleigh criterion is given by:  $r_{con} = 0.72r_{Airy} = 0.44 \frac{\lambda}{NA}$  (2-31)

We can find from Equation 2-31 that the lateral resolution of the confocal microscopy is slightly better than that of the conventional bright-field microscopy. However, in fact, the suppressed subsidiary peaks in confocal microscopy have more significance in imaging performance. For wide-field microscopy, when a dim object is located near a bright object, the subsidiary peaks of the bright object may obscure the dim object. Yet for confocal microscopy, the subsidiary peaks of the bright object are greatly suppressed, so they are less likely to spoil the contrast and the dim object are more likely to be seen. This further demonstrates the contrast enhancement capacity of the confocal microscopy. The contrast enhancement is important since it can make the best use of the resolution.

The axial resolution of the confocal microscopy following the 26% dip from the Rayleigh criterion is given by:  $z_{con} = 1.5 \frac{n\lambda}{NA^2}$  (2-32)

The axial resolution is often measured by translating a mirror axially through the focal plane and recording the distance between the half maximum points of the detected power. This resolution is also named FWHM axial resolution and it's given by

$$Z_{FWHM} = \frac{0.45\lambda}{1 - \cos \theta} \quad (2-33)$$

$$z_{FWHM} / z_{con} \approx 0.84 \quad (2-34)$$

### 2.2.2.2 Contrast

In microscopy, we need not only the high resolution to discriminate the fine details of the sample, but also enough contrast between pixels for an image to be perceivable by human eye. The contrast to the microscopy is as essential as the resolution.

The relative contrast is defined as the variation of the signal intensity divided by the average of the signal intensity:

$$C = \frac{\Delta I}{I_{Avg}} \quad (2-35)$$

In microscopy, the contrast of image comes from different sources: reflection, scattering, phase shift, single-photon and multi-photon fluorescence, fluorescence spectral shift, fluorescence lifetime, harmonic generation, polarization change, or absorption, all of which can be utilized to generate different modes of microscopy [91].

Contrast Transfer Function (CTF) is a particularly important tool for the confocal microscopy, or any microscopy in general. CTF plots the contrast of the image of the objects as the function of the size or the spatial frequency of the objects. The Rayleigh criterion merely represents a point in CTF where the contrast of the image is 26% at the Rayleigh resolution or spatial frequency. Note that the Rayleigh resolution is not an absolute limit beyond which nothing works or below which everything is perfect. CTF more comprehensively represent how the image contrasts are at different spatial frequencies. CTF is also a link of resolution and contrast because the resolution is actually defined in terms of contrast it represents. The basic mechanism behind CTF is

diffraction which determines that the contrast level will be higher for bigger features and lower for smaller features [91].

Contrast has to be considered relative to noise which is the real problem and the limiting factor. The noise sources faced by the confocal microscopy include: shot noise, background noise. Signal to noise ratio (S/N) is an important criterion for the overall image quality.

Shot noise is the most important source of noise in confocal microscopy that fundamentally limits the S/N. Shot noise is also called Statistic noise or poisson noise. It originates from the quantum behavior of photons striking the detector and the statistical variation in the number of photons detected by the detector. The shot noise follows the Poisson distribution and is given by the square root of the mean number of incident photons on detector as  $\sqrt{n_i}$ . Consider a detector with a quantum efficiency of  $Q_E$  and a noise from detector  $n_d$ , then the S/N is given by

$$\frac{S}{N} = \frac{Q_E n_i}{\sqrt{Q_E n_i + n_d^2}} \quad (2-36)$$

Background noise is the stray light mixed with the signal. In BSL mode, the stray light can come from the specular reflection from the surface of the optical components, or the scattered light within the microscope, or part of the scattered light from outside the confocal volume that pass through the pinhole. The background noise is directly related to the size of the pinhole: the bigger the pinhole, the more stray light pass through. Different models of the background noise have been reported [91].

### 2.2.3 Confocal Scanning Endomicroscopy

Confocal endomicroscopy is an emerging imaging technology valuable for in-vivo imaging of gastrointestinal mucosa, liver, and pancreatic duct, etc [186]. It is an extension of the confocal microscopy to endoscopic applications for in-vivo cancer diagnosis. Confocal endomicroscopy enables real time in-vivo imaging with sub-cellular resolution and optical sectioning capacity, and optical biopsy that allow in-vivo localizing, staging and grading of malignant precancerous lesions without physically removing tissue by excisional biopsy. It can greatly reduce the sampling errors from the random excisional biopsy, can guide surgical procedures, and can provide access to internal tissues where standard excisional biopsy is impossible or too dangerous.

Numerous studies have been conducted on confocal endomicroscopy in various clinical settings. Confocal endomicroscopy was used to examine various GI conditions, including neoplastic changes in colon polyps for colorectal cancer screen [39], celiac disease [36], gastric cancer [37], Barrett's esophagus [38], Helicobacter pylori infection [41], etc. Needle-based confocal endomicroscopy with a diameter of 0.85 mm was used to enable histology of liver tissues [40].

Up to now, the commercial systems of confocal endomicroscopy approved by FDA include the integrated endomicroscopy system by Pentax (Japan) and the probe-based endoscopy system by Manuna Kea Technologies (Paris, France). The Pentax endomicroscopy system (EG-3870CIK, Figure 2-5) includes a conventional white light video endoscope, and a blue laser confocal microscope integrated into the 12.8 mm distal tip of the endoscope. Confocal image slices of 7  $\mu\text{m}$  in thickness and 500  $\mu\text{m}$  by 500  $\mu\text{m}$  in field of view can be obtained along a depth range of 0-250  $\mu\text{m}$  with a

resolution of 0.7  $\mu\text{m}$ . The frame rate is 1.6 fs/sec or 0.8 fs/sec depending on the size of the image. The depth scan is step controlled with about 4  $\mu\text{m}$  increments [186].

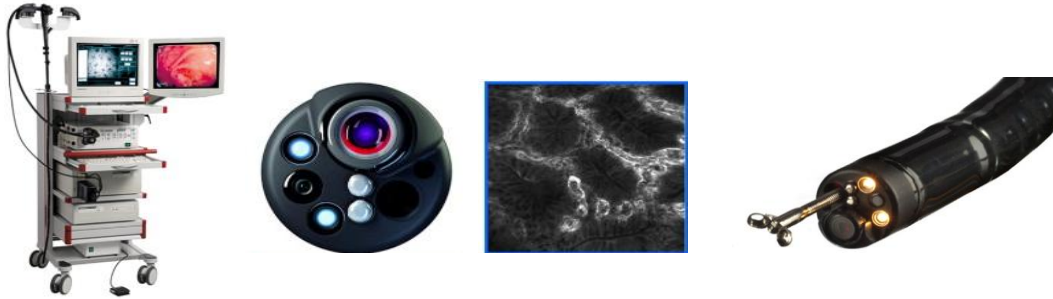


Figure 2-5. Integrated endomicroscopy system from Pentax

The stand-alone confocal endoscope probe from Manuna Kea Technologies (Paris, France) is the first commercial available probe-based confocal endomicroscopy system (Figure 2-6). Different confocal mini-probes are designed to work in different endoscopy including Eso-Gastro-Duodenoscopy, Concoal Cholangioscopy in ERCP, Colonoscopy, and Bronchoscopy and Alveoscopy (link). A high frame rate of 12 fs/s is realized for video confocal imaging. Various sizes of the probes are provided to be compatible with operating channels from 1.2 mm to 2.8 mm. Lateral resolution ranges from 1  $\mu\text{m}$  to 3.5  $\mu\text{m}$ , and the field-of-view ranges from 240  $\mu\text{m}$  to 600  $\mu\text{m}$  [186]. The imaging depth is fixed. Fiber bundle and laser scanning unit are used.

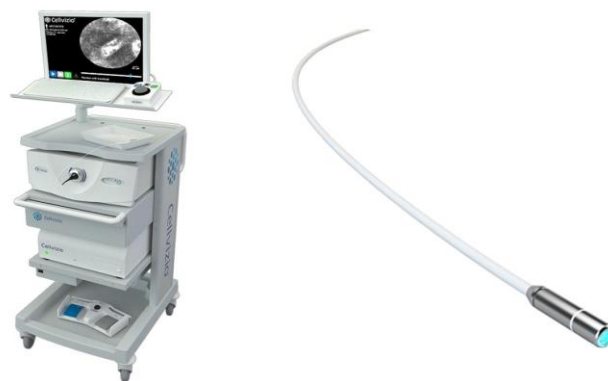


Figure 2-6. Confocal endoscope probe from Manuna Kea Technologies

To develop miniature endoscope probe suitable for in-vivo confocal microscopic imaging have been a goal for researchers for long. The challenges for 3D confocal endomicroscopy includes the miniaturization of optical scan engines especially for both lateral and axial scans, the requirement of large scan range under low drive voltage, and the miniaturization of the optics without largely sacrificing the optical performance. The diameter requirement ranges from less than one millimeter to several millimeters and the rigid length from millimeters to several centimeters.

Beam scanning mechanisms that have been adopted in endomicroscopy include vibrating the tip of a single fiber at the distal end [65, 66], scanning at proximal end across a fiber bundle [57-60], and scanning light beam by MEMS-based scan engines [187,188]. Using the fiber bundle avoids the scan at the distal end, thereby simplifying the miniaturization of the image head. However, since the fiber cores are spatially separated by the claddings, the image plane is sampled at discrete points. The limitations are the inherent pixilation artifact of fiber bundle because of the spacing between fibers, and the compromise among the sampling, the photo-efficiency and the resolution [90, 91]. Fiber distal vibration by piezoelectric element or other motors doesn't suffer from the sampling problems as the fiber bundle faces, because the scan is continuous, but it has the drawbacks of instability of light coupling especially for big angles. Optical beam scanning employing MEMS scanners provides an option to continuously scan beam at high speed and large range with high stability and multidimensional scan capability. Meantime MEMS scanners can be miniature enough to fit into the endoscope.

Confocal microscopes based on miniature MEMS scanners have been extensively studied and reported. Maitland *et al.* and Shin *et al.* reported confocal microscopes using 2D MEMS mirrors for the lateral scan [71, 72], but the depth scan was absent. MEMS-based confocal microscopes capable of 3D scan have been reported [73-76]. However, the systems reported in [74-76] relied on external motors and sliding stages for the axial scan. The instability from friction and the tradeoffs between size, speed and cost are the potential challenges of using external motor-based axial scanners. Jeong *et al.* presented a 3D dual-axis confocal microscope using a pair of electrostatic MEMS mirrors, with the 2D mirror for the lateral scan and the 1D mirror for the depth scan, but the axial displacement was only 10  $\mu\text{m}$  at 200 V dc or  $\pm 27.5 \mu\text{m}$  at resonance (4.69 kHz) under an ac voltage from 0-180 V [73]. The static displacement was too small even at high voltage, while at resonance, the frequency was too high for the axial scan. To develop a miniature 3D scanning system that could generate large scan range for both lateral and axial scan under low driving voltage is a research goal for this research.

### **2.3 Chapter Summary**

This chapter reviews the theory and important optical parameters of OCT and CSM. It also covers the confocal scanning endomicroscopy systems that have been reported, including the two commercial products under clinical use. The theoretical background in this chapter is the basis and design guidance for the endoscopic OCT system and the CSM systems developed in this research. The descriptions of the developed MEMS-based OCT system and CSM systems will be given in Chapter 3 and Chapter 5.

### CHAPTER 3 THROUGH-SILICON-VIAS MICROMIRROR AND ENDOSCOPIC OCT APPLICATIONS

As we introduced in Chapter 1 and Chapter 2, OCT is an imaging technology that holds great promises for optical biopsy and cancer *in vivo* detection. To develop miniature yet high-performance endoscopic OCT is an aim for many researchers. The technical difficulty, however, lies mainly in the optical scanning mechanism that could provide large-range high-speed scan at low driving voltage, and at the same time realize high-degree miniaturization to access the internal organs.

MEMS scanner is a better choice for endoscopic OCT than proximal end rotating/translating motor and distal end fiber-tip swing element, because MEMS scanner is capable of fast scan with uniform coupling. The size requirement of the MEMS-based OCT probe is stringent in many endoscopic imaging applications; however, to shrink the MEMS-base probe to size smaller than standard GI endoscope channel diameter (2.8 mm) is very challenging. In this Chapter we will introduce a novel design of through-silicon-via electrothermal micromirror that aims to push the limit of the miniaturization of MEMS-based endoscopic probe. By using a unique through-silicon-via interconnection in an electrothermal micromirror together with an ultra-compact probe design, the probe size has been reduced to only 2.6 mm in diameter, which is small enough to fit into most endoscope channels. A complete endoscopic OCT system integrating the miniature probe is developed and imaging results are presented in this chapter.

## **3.1 Electrothermal Bimorph Actuators**

### **3.1.1 Principles of Electrothermal Bimorph Actuation**

Stress in thin film is the sum of the residual internal stress and the extrinsic stress [189, 190]. Residual stress includes a thermal stress and an intrinsic stress. The thermal stress part of the residual stress is induced by changes of the temperature conditions during and after the film growth or deposition. The intrinsic stress is strongly dependent on the growth or deposition environment and the materials. It may arise from several origins including lattice mismatch, grain coalescence, accumulation of the crystallographic flaws, impurities incorporation, phase transformation, rapid film growth, and recrystallizing process [189-192]. The extrinsic stress is the stress induced after the film growth or deposition, which can be caused by external factors such as packaging, force from other materials, temperature change, material phase change, etc. The temperature change causes the thermal stress due to the different thermal expansion coefficients between the film and the substrate. The stress is either compressive that tends to expand, or tensile that tends to contract.

Bimorph is a structure with two layers of thin films stacked together. In an electrothermal bimorph structure, the two layers have different coefficients of thermal expansion (CTE). Bimorph cantilever can convert the strain differences between two layers to the bending displacement perpendicular to the strain. Electrothermal bimorph actuator uses the internal residual stress to set the bimorph cantilever to an initial curvature and elevation, and then use the Joule heating to induce the extrinsic thermal stress for the actuation.

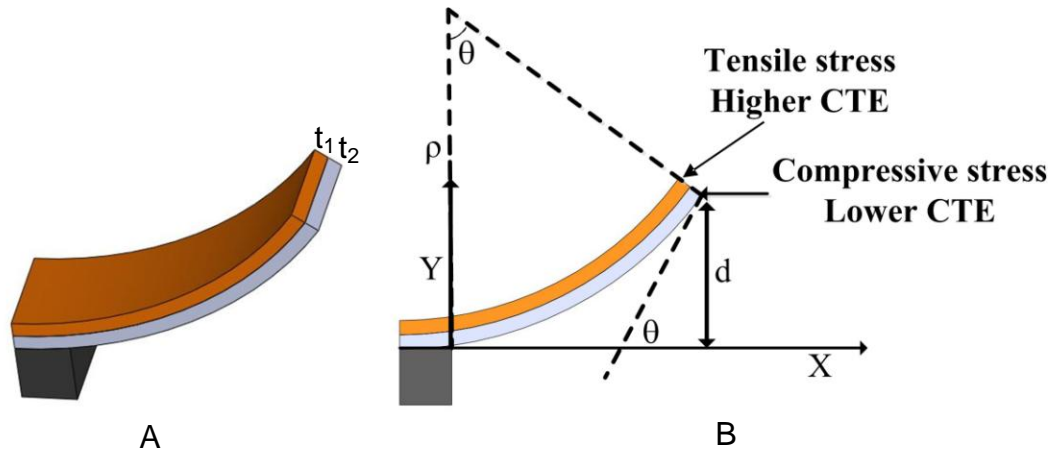


Figure 3-1. Structural views of a cantilevered bimorph beam. A) 3D view of the curvature of a cantilevered bimorph beam. B) Cross sectional view of the curvature of a cantilevered bimorph beam.

The initial curvature of a bimorph cantilever  $\rho_{in}$  due to the residual stress after release is given by [193]:

$$\frac{1}{\rho_{in}} = \frac{\beta}{t_1 + t_2} \Delta \varepsilon_{in} \quad (3-1)$$

, where

$$\beta = \frac{6(1 + \frac{t_1}{t_2})^2}{\frac{E'_1}{E'_2} \cdot \frac{t_1^3}{t_2^3} + \frac{E'_2}{E'_1} \cdot \frac{t_2}{t_1} + 4 \frac{t_1^2}{t_2^2} + 6 \frac{t_1}{t_2} + 4} \quad (3-2)$$

, where  $\Delta \varepsilon_{in}$  represents the initial strain difference induced by the residual stress,  $t_1$  and  $t_2$  are the thickness of the two layers, respectively.  $E'_1$  and  $E'_2$  are the biaxial elastic modulus of two layers related to Young's modulus E and Poisson ratio:

$$E'_i = \frac{E_i}{1 - \nu_i} \quad i = 1, 2 \quad (3-3)$$

Upon electrical current added to the bimorph, the temperature change induced by the Joule heating will introduce another bending curvature. The curvature due to the thermal expansion mismatch of two layers can be expressed as:

$$\frac{1}{\rho_{th}} = \frac{\beta}{t_1 + t_2} \Delta \varepsilon_{th} \quad (3-4)$$

, where  $\Delta \varepsilon_{th} = (\alpha_1 - \alpha_2) \cdot \Delta T$  denotes the strain mismatch caused by the Joule heating.

The initial curvature due to the residual stress and the curvature due to the Joule heating can be added to give the total bending radius as:

$$\frac{1}{\rho} = \frac{1}{\rho_{in}} + \frac{1}{\rho_{th}} \quad (3-5)$$

With the radius of curvature derived as Equation 3-5, the tangential angle at the tip of the bimorph beam  $\theta_{th}$ , can be laid out from geometry:

$$\theta = \frac{l_b}{\rho} = \frac{\beta l_b}{t_1 + t_2} (\Delta \varepsilon_{in} + \Delta \varepsilon_{th}) \quad (3-6)$$

, where  $l_b$  is the length of the bimorph beam.

If the temperature change induced by Joule heating is not uniformly distributed along the bimorph, the radius of curvature will also vary along the bimorph beam. The tangential angle at the tip of the bimorph can be deducted by the accumulation of curvature change along the bimorph beam:

$$\theta_{th-j} = \int_0^{l_b} \frac{dx}{\rho_{th}(x)} = \frac{\beta l_b}{t_1 + t_2} (\alpha_1 - \alpha_2) \frac{\int_0^{l_b} \Delta T(x) dx}{l_b} = \frac{\beta l_b}{t_1 + t_2} (\alpha_1 - \alpha_2) \overline{\Delta T} \quad (3-7)$$

, where  $\overline{\Delta T} = \frac{1}{l_b} \int_0^{l_b} \Delta T(x) dx$  is the average temperature rise along the beam.

### 3.1.2 Optimization and Materials Selection

The sensitivity of the bimorph beam is defined as the bending angle divided by the temperature change:

$$S = \frac{\theta_{th}}{\Delta T} = \frac{\beta l_b}{t_1 + t_2} (\alpha_1 - \alpha_2) \quad (3-8)$$

The bimorph sensitivity is proportional to the length of the bimorph beam  $l_b$ , the difference between two CTEs  $(\alpha_1 - \alpha_2)$ , and the curvature coefficient of the bimorph  $\beta$ . The sensitivity is inversely proportional to the total thickness of the bimorph  $(t_1 + t_2)$ .

Optimization of the materials and the geometry of the bimorph are essential in order to achieve optimal sensitivity. Since bimorph sensitivity is proportional to the difference between two CTEs  $(\alpha_1 - \alpha_2)$ , we should start with choosing two materials with large difference in CTE. Table 3-1 is a summary of the thermal and mechanical properties of commonly used MEMS materials [138-144].

Table 3-1. Thermal-mechanical properties of commonly used MEMS materials

Materials	CTE ( $10^{-6}/K$ )	Young's Modulus (GPa)	Poisson Ratio	Thermal Conductivity (W/m·K)
Si	3.0	179	0.27	150.0
SiO <sub>2</sub>	0.4	70	0.17	1.4
Si <sub>3</sub> N <sub>4</sub>	3.3	310	0.24	30.0
Poly-Si	1.6	160	0.22	-
Al	23.6	70	0.35	237.0
Au	14.5	78	0.44	318.0
Cu	16.9	120	0.34	401.0
Cr	5.0	279	0.21	93.9
Pt	8.9	168	0.38	71.6
Ti	8.6	116	0.32	21.9
Ni	12.8	200	0.31	90.9
SU8	52	4	0.22	0.2
PDMS	310	0.00075	0.5	0.15

We can see From Table 3-1 that Al and SiO<sub>2</sub> have very big CTE mismatch, which is favorable for large sensitivity. Besides, both materials are very commonly used materials in IC and MEMS with well-developed and cost-effective fabrication and processing techniques. Al is also a good coating material for mirror surface with high reflectivity over a wide band of light wavelengths. Polymer materials such as PDMS, as listed in Table 3-1, have very large CTE. However, their major drawbacks are that the Young's modulus is too low to make high-frequency scanner and they typically work under low temperature.

We can also see from Equation 3-8 that increasing the bimorph length to thickness ratio,  $l_b/(t_1+t_2)$ , can improve the sensitivity as well. However, these geometry parameters are closely related to the mechanical characteristics of the bimorph actuator including beam stiffness and resonant frequency, therefore subjected to constraints from mechanical characteristics. Comprehensive considerations have to be made in both mechanical properties and sensitivity.

Besides, we can know from Equation 3-8 that the sensitivity can also be optimized by maximizing the curvature coefficient  $\beta$ . Assuming a given total thickness  $(t_1+t_2)$ , the thickness ratio that yields the maximum value of  $\beta$  has been derived by S.

Todd as [194]:

$$\frac{t_1}{t_2} = \sqrt{\frac{E_2'}{E_1'}} \quad (3-9)$$

Under this thickness ratio,  $\beta$  reaches its maximum value of 1.5. The optimal thickness ratio for Al/SiO<sub>2</sub> as the bimorph materials is 0.91.

## 3.2 TSV Micromirror

### 3.2.1 TSV Micromirror Design

The TSV MEMS mirror is actuated by four electrothermal lateral-shift-free (LSF) large-vertical-displacement (LVD) actuators. The concept and design of the LSF-LVD actuator were first developed by L. Wu [136]. The design schematic the LSF-LVD actuator is shown in Figure 3-2 [136]. Each LSF-LVD actuator has three Al/SiO<sub>2</sub> bimorphs and two rigid silicon frames connected in between. The bimorphs and frames are arranged in a folded fashion to reduce the actuator area and thus increase the fill factor. Platinum (Pt) is selected as the heater materials and a thin layer of Pt is embedded along all bimorphs and frames for uniform heating. The up layer of the bimorph is Al with tensile stress and the bottom layer is SiO<sub>2</sub> with compressive stress. Therefore, after release, the bimorph beams curl up to an initial elevation height. Upon Joule heating is generated by the drive current, the bimorph beams bends down and actuates the mirror plate downwards.

The LSF-LVD actuator has three bimorph beams and two silicon frames connected in series in order to achieve large vertical displacement. The motions of the three bimorph beams and the two frames need to be balanced and controlled in a way that that the mirror plate remains parallel to the substrate during the vertical displacement, and the lateral shift of the actuator is minimized for stable actuation and small stress on mirror plate.

In order to have the mirror plate parallel to the substrate, the sum of the rotation angles of bimorph I  $\theta_1$  and bimorph III  $\theta_3$  should be equal to the rotation angle of bimorph II  $\theta_2$ :

$$\theta_1 + \theta_3 = \theta_2 \quad (3-10)$$

Assuming uniform heating on three bimorphs, the rotation angle will be proportional to the lengths of bimorphs. We set the lengths of bimorph I ( $l_1$ ) and bimorph III ( $l_3$ ) equal to one half of the length of bimorph II ( $l_2$ ).

$$l_1 = l_3 = l_2 / 2 \quad (3-11)$$

The lateral shift of the LSF-LVD actuator can be expressed as [136]:

$$LS = LS_{BimorphI} + LS_{FrameI} - LS_{BimorphII} - LS_{FrameII} + LS_{BimorphIII} = (L_1 - L_2)(1 - \cos \theta_1) \quad (3-12)$$

, where  $L_1$  and  $L_2$  are the length of Frame I and Frame II, respectively. To cancel out the lateral shift, we set  $L_1$  and  $L_2$  equal:

$$L_1 = L_2 \quad (3-13)$$

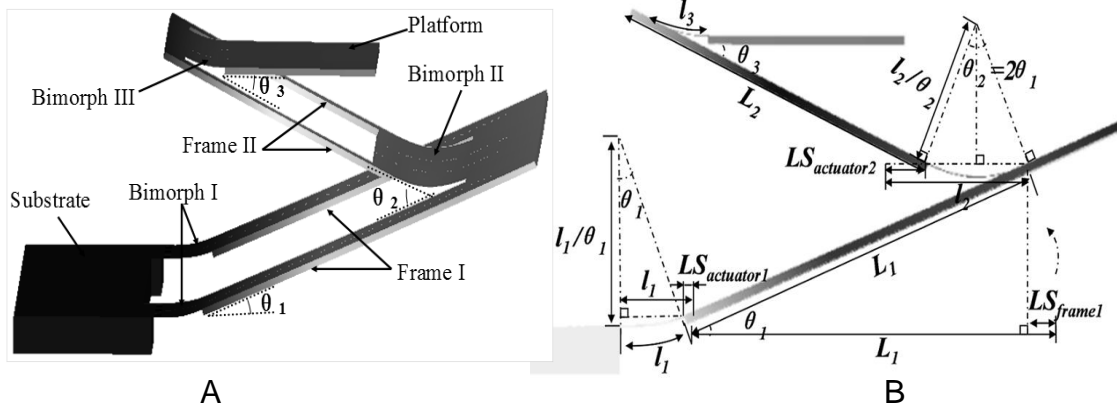


Figure 3-2. Design concept and geometry schematic of the LSF-LVD actuator. A) 3D model. B) Schematic of geometry.

FEM model of the LSF-LVD actuator has been built by Lei Wu *et al.* [136]. The TSV micromirror uses four LSF-LVD actuators illustrated above to support and actuate the mirror plate, and four through-silicon-vias for electrical interconnection. As shown in Figure 3-3, the TSV MEMS mirror is comprised of a mirror plate and four identical LSF-LVD actuators supporting the mirror plate on four sides. The four LSF-LVD actuators

are symmetrically arranged about the mirror plate. The symmetry and the confinement from the rigid mirror plate can further cancel out the lateral shift and the tilting. When a same driving voltage is simultaneously added to all four LSF-LVD actuators, the mirror plate will be moved downward vertically without lateral shift or tilt angle. When the four actuators are actuated by different driving voltages, tip-tilt scanning can be performed.

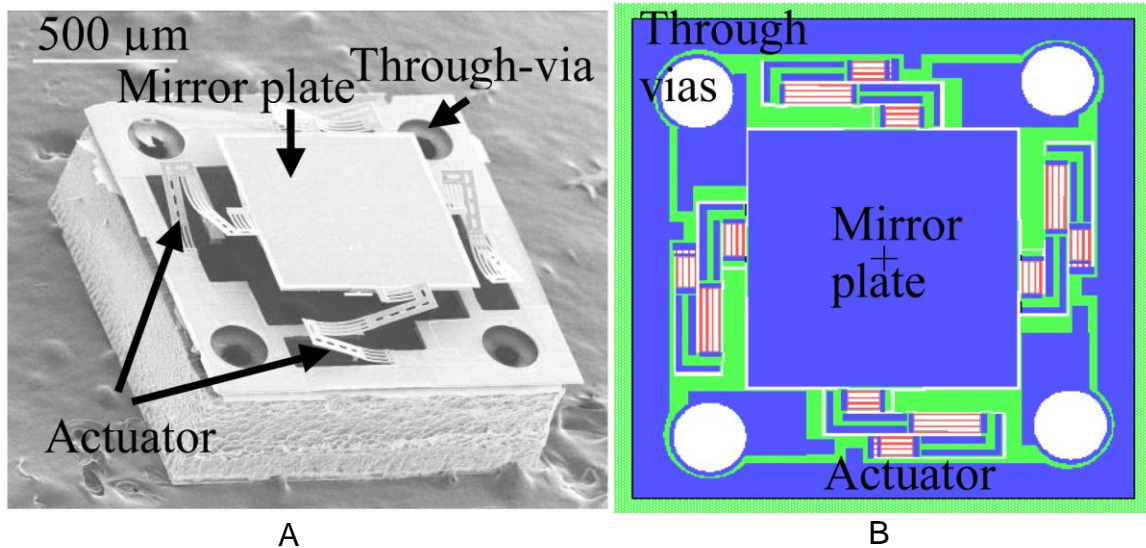


Figure 3-3. TSV micromirror design. A) SEM image. B) Design schematic.

There are four through-silicon vias symmetrically located at the four corners of the mirror device and four pads sitting next to the through vias. These TSVs are designed to allow the electrical wires to go through from backside and be bonded to the pads. When assembling the MEMS micromirror to the endoscopic OCT probe, no PCB board with printed pads for electrical connection is needed. The TSV mirror could simply sit on the probe base, having four wires inserted through from behind the mirror substrate and then connected by conductive epoxy to the four pads on the mirror plate. The through silicon vias connection eases the bonding process, and also saves space for wire-bonding because no extra PCB board with additional pads and wires are

needed by TSV electrical interconnection. A space saving of 1-2 millimeter may be a small number, but it matters when it comes to the endoscopic probe in which the miniaturization is essential but difficult. Shrinkage in probe diameter of one-to-two millimeter can make a big difference in medical applications.

The design parameters of the TSV micromirror are summarized in Table 3-2. The mirror plate is a square rigid plate with Al coating on top and Single-crystalline silicon on bottom and the size is set as 0.8 mm by 0.8 mm. The device footprint is only 1.5 mm by 1.5 mm and it can be fit into the 2.6 mm endoscopic probe described in next section. The thickness ratio of Al/SiO<sub>2</sub> is optimized as 0.91 for high sensitivity. The lengths of the three segments of bimorphs are set as 100 μm, 200 μm, 100 μm, respectively so that the angular rotations are balanced and the mirror plate can keep parallel to the substrate. Four parallel bimorph beams with a wide of 10 μm are grouped in parallel and separated by a gap of 8 μm.

Table 3-2. Design parameters summary of TSV micromirror

Structural Parameters	Value
Mirror plate size	0.8 mm by 0.8 mm
Device footprint	1.5 mm by 1.5 mm
Length of bimorph	100 μm, 200 μm, 100 μm
Length of frame	264 μm
Width of bimorph	10 μm
Width of Pt heater	6 μm
Diameter of via	220 μm
Thickness of Silicon dioxide	1.1 μm
Thickness of Al	1 μm
Thickness of Pt heater	0.25 μm

### 3.2.2 Device Fabrication

The device is fabricated using a combined surface- and bulk-micromachining process. The process flow is illustrated in Figure 3-4. The fabrication is based on a SOI wafer with 50  $\mu\text{m}$  device layer, 2  $\mu\text{m}$  buried oxide and 400  $\mu\text{m}$  handling layer. The first step is PECVD deposition of 1.1  $\mu\text{m}$  thick  $\text{SiO}_2$  on the SOI wafer A). This  $\text{SiO}_2$  layer serves as the bottom layer of bimorphs. Then a Cr/Pt/Cr film of 200  $\text{\AA}$ /0.2  $\mu\text{m}$ /200  $\text{\AA}$  is spluttered, and patterned by lift-off process on top of the 1.1  $\mu\text{m}$  thick  $\text{SiO}_2$  B). After that, a dielectric  $\text{SiO}_2$  layer of 0.15  $\mu\text{m}$  is deposited by PECVD and patterned by RIE dry etch for the electrical isolation C). Next, an Aluminum layer of 1  $\mu\text{m}$  is evaporated and lifted-off to form the top structure layer of bimorphs and the mirror plate surface D). A second  $\text{SiO}_2$  layer is then deposited by PECVD and dry etched by RIE plasma to form a hard mask for the front-side Silicon etch E). Then, a back-side bulk silicon etch is performed till the etch stop at the buried oxide, followed by the buried oxide etch by RIE plasma F). Finally, an anisotropic silicon etch is performed to etch through the device layer G), followed by an isotropic silicon etch to undercut and release the bimorphs H).

### 3.2.3 Device Characterization

The bimorph beams curl upward after release due to the residual stress and will bend downward under electrothermal actuation. The initial elevation at room temperature is 209  $\mu\text{m}$ . Tip-tilt motion can be generated by differentially driving two opposite actuators and the piston motion by simultaneously driving all four actuators. The mirror demonstrates optical scan angle of  $\pm 16^\circ$  at 3.6 V for both x- and y-axis as shown in Figure 3-5. The static scan angle was measured by first adding a pair of ac differential voltages,  $V + V \cos(\omega t)$  and  $V - V \cos(\omega t)$ , with a low frequency of 0.5 Hz to

one set of opposing actuators. A laser beam was deflected by the mirror plate to a screen with coordinate grids. The angle-versus-voltage response is not linear at low voltage, and becomes linear after a critical voltage. The linear response is caused by the combination of temperature-dependent resistance and voltage-squared dependence of the produced heating power, which can be explained by an electrothermalmechanical lumped element model reported in [195].

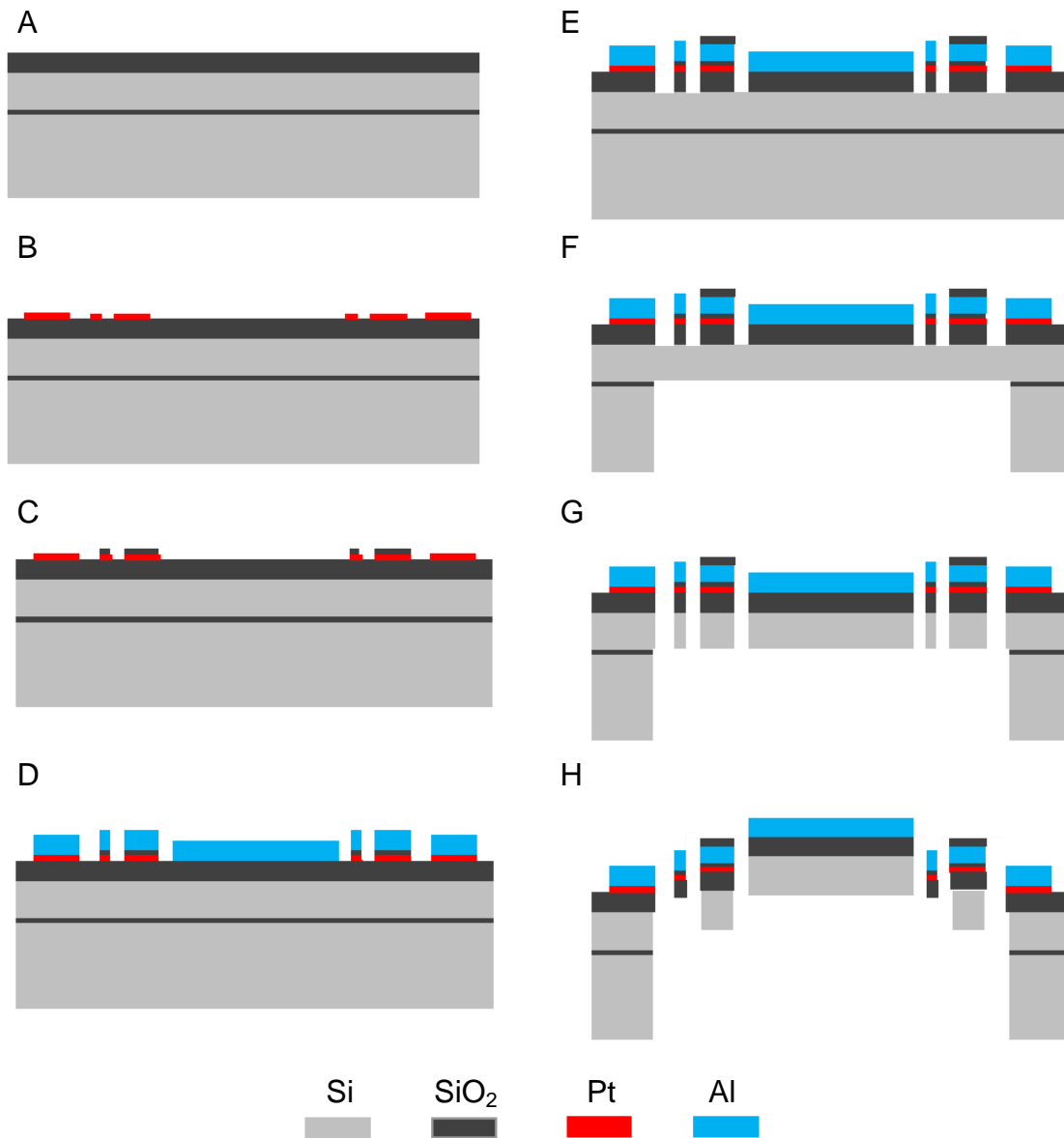


Figure 3-4. Process flow of the TSV micromirror

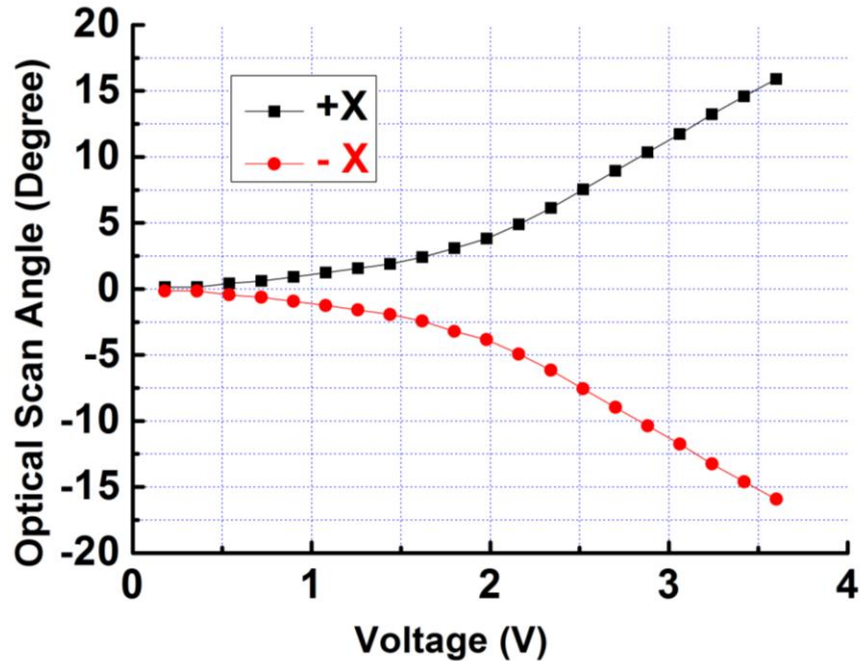


Figure 3-5. Static scan angle test result for the TSV micromirror

Static vertical displacement of the TSV micromirror was measured by an Olympus BX51 optical microscope and a Quadra-Chek 200 micro-position recorder. The micro-position recorder is able to track the x, y, and z position of the microscope with a resolution of 0.5  $\mu\text{m}$ . A dc voltage was applied to the four LSF-LVD actuators simultaneously. The vertical displacement of the mirror was measured by focusing the microscope on the mirror surface and reading the corresponding z coordinate from the micro-position recorder. The image was re-focused and the z-position was re-read after each increment of the dc voltage. The coordinates of multiple points on the mirror plate were recorded to calculate the vertical displacement as well as the lateral shift and tilt. The static vertical displacement measurement result is shown in Figure 3-6. The vertical displacement is 215  $\mu\text{m}$  at 4 V. The mirror plate has an initial tilting angle of approximately 0.17°. The resistances of the four LSF-LVD actuators were measured to be  $240 \pm 2 \Omega$ .

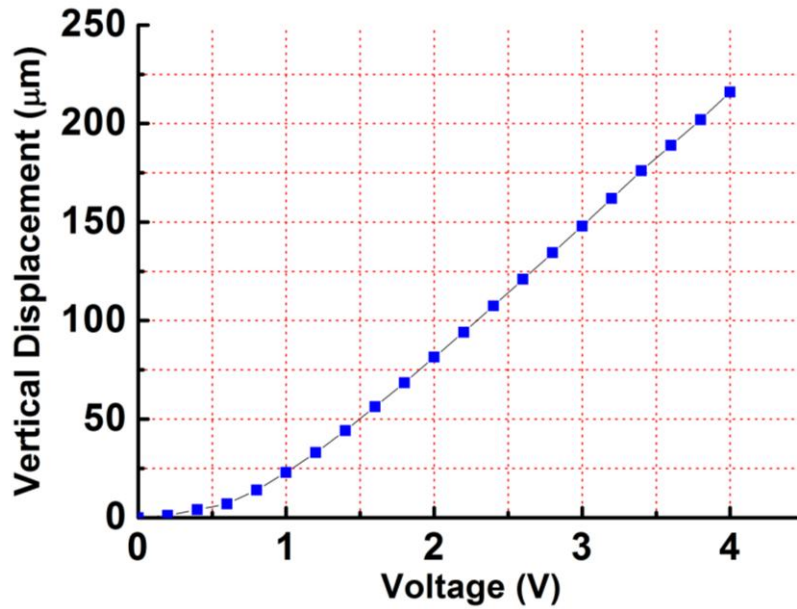


Figure 3-6. Static vertical displacement test result for the TSV micromirror

The frequency response of the tip-tilt mode was measured by adding a DC voltage to all four actuators and a pair of small differential AC voltages to one opposing actuators. Scan angles at different frequencies of the AC signal were recorded and plotted in Figure 3-7. The first resonance peak of 659 Hz was observed for the device.

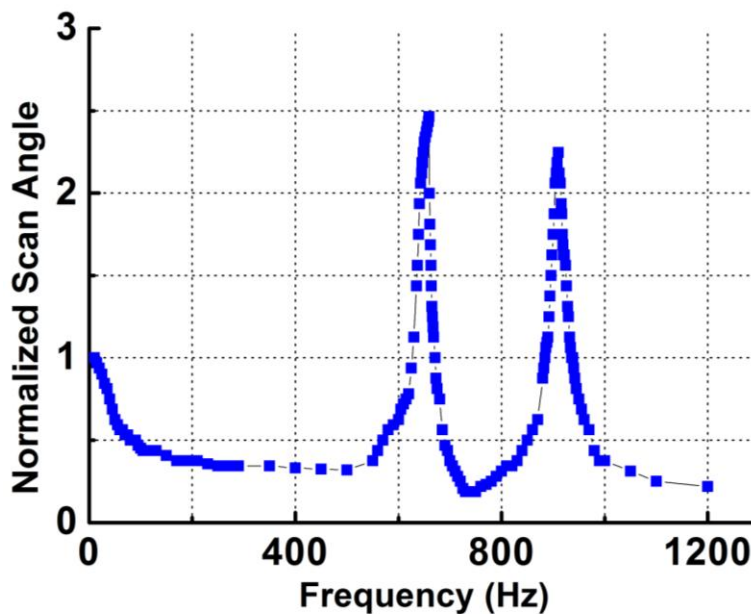


Figure 3-7. Frequency response test result for the TSV micromirror

### 3.3 Endoscopic OCT Imaging Using TSV Micromirror

#### 3.3.1 Endoscopic OCT System

A time-domain endoscopic OCT system using a TSV mirror for 2D beam scanning was developed and experimentally demonstrated. As shown in Figure 3-8, the endoscopic OCT system is comprised of a broadband light source, a 2 by 2 fiber-based beam splitter, a circulator, a balanced photodetector, a rapid scanning optical delay line (RSOD), and a MEMS-based imaging probe. The light source (DenseLight, DL-BX9-CS3159A) has a central wavelength of 1310 nm with the full width half maximum (FWHM) bandwidth of 75 nm, which corresponds to a 10  $\mu\text{m}$  axial resolution in air. Light is divided by the beam splitter into two paths, i.e., a reference arm and a sample arm. The RSOD in the reference arm provides the depth scan, with a scanning rate of 1 kHz and an effective optical path scan range of 1.6 mm. A carrier frequency of 500 kHz is generated by laterally shifting a rapid scanning mirror in the RSOD. The measured sensitivity of the system is 53 dB. Interference signals are acquired by a data acquisition card and processed by a computer. Two images are acquired for each period, one from the forward scan and one from the backward scan. The frame rate of this system is 2.5 fs/s.

A miniature OCT endoscopic probe in the sample arm performs the OCT imaging *in vivo*. The probe consists of a TSV interconnect MEMS mirror, a GRIN lens, a single-mode fiber and a metal mount base, as shown in Figure 3-9. The single mode fiber (corning SMF-28) delivers the light to the probe. The GRIN lens (NSG America ILW-0.7) focuses the light from the fiber to a small spot size. After the GRIN lens, the 2D MEMS mirror deflects the light out of the probe and scans the sample in x- and y- axis. The

returning light is collected by the MEMS mirror, which is directed to the GRIN lens and then coupled back to the single mode fiber.

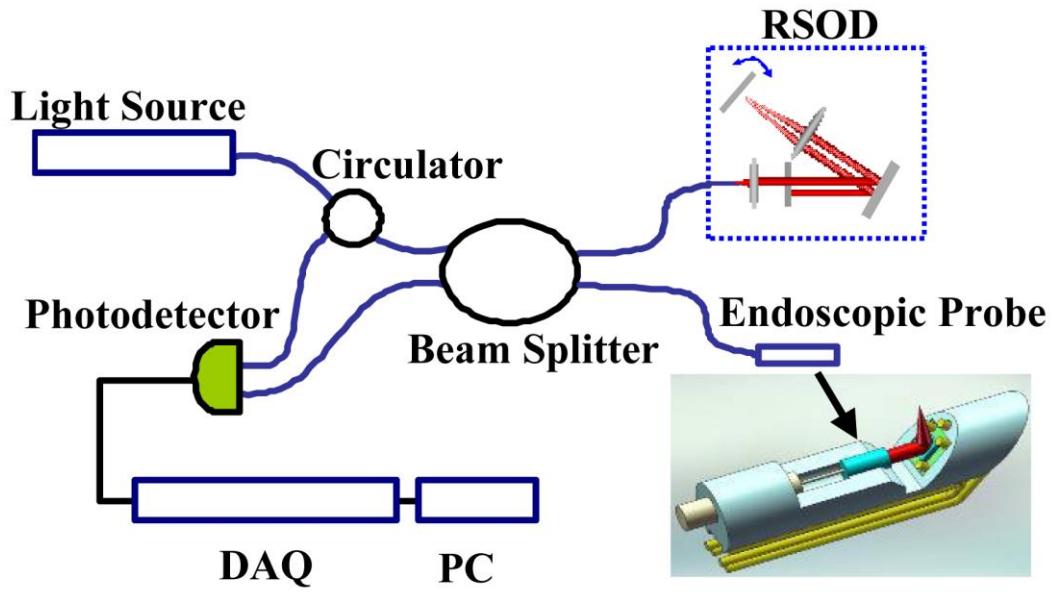


Figure 3-8. Schematic of the endoscopic OCT system

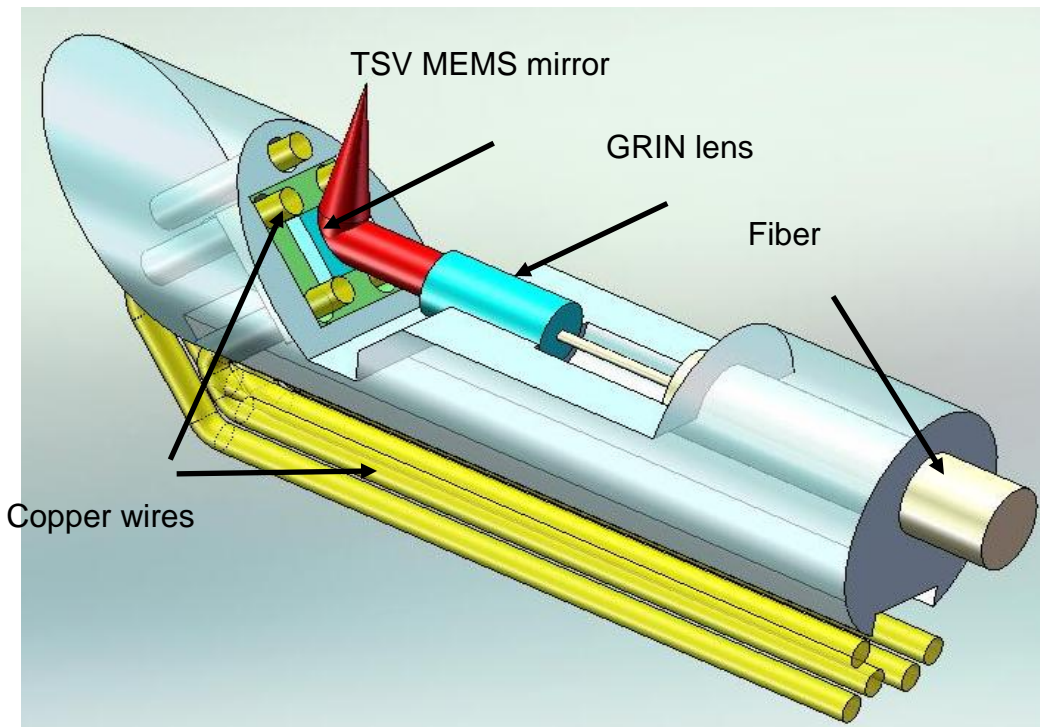


Figure 3-9. 3D model of the endoscopic OCT probe design

The fiber tip is cut with an  $8^\circ$  angle by an angle fiber cleaver to avoid the back-reflection. The fiber and GRIN lens are glued to their grooves in the probe and precisely aligned. The MEMS mirror is fixed into a 0.5 mm-deep square cavity which is slanted at  $45^\circ$  to the central axis of the probe. There are five through-holes in the metal mount. Five copper wires are inserted through these through-holes from the backside of the probe. Four of them go through the TSVs of the mirror chip from the backside and are connected to the pads of the four actuators on the front side. The fifth wire is also inserted from the backside of the probe base and then connected to the ground pad of the mirror. The electrical connection is accomplished using silver epoxy. After all these steps are finished, the loaded probe is slipped into a flexible biocompatible transparent fluorinated ethylene propylene (FEP) tube. The length of the metal mount is the 10.7mm. A wood stick is used to form a rigid part of the probe. The diameter and the length of the GRIN lens are 0.7 mm and 2 mm, respectively. The pitch number is 0.27. The focal length of the GRIN lens is 5 mm. The working distance, i.e., the distance from the outer wall of the probe to the focal point of the light beam, is designed to be 1.5 mm in air. The outer diameter of the probe is measured to be 2.6 mm. Figure 3-10A shows a loaded probe and Figure 3-10B shows a picture of a packaged probe inside the FEP tube.

### **3.3.2 Imaging Experiment and Results**

The MEMS-based imaging probe has been integrated into the sample arm of the time-domain OCT system for imaging experiments. The depth scan is done by the RSOD. The 2D lateral scan is performed by differentially driving one pair of opposite actuators for fast axis scan and the other pair for slow axis scan. The driving voltages for the fast axis and slow axis are respectively a 1.25 Hz 0-4 V ramp waveform and a

2 mHz 0-4 V ramp waveform. 2D and 3D OCT images of microspheres embedded in PDMS and an acute rat brain tissue have been performed to show the capability of this MEMS-based probe, which are shown in Figure 3-11 and Figure 3-12. The size of the polystyrene microspheres is about 20  $\mu\text{m}$ . The microspheres are embedded in a transparent PDMS. The corpus callosum region of the acute brain tissue is imaged. The brain tissue is sliced to about 400  $\mu\text{m}$  in thickness. The scan depth is 1.6 mm.

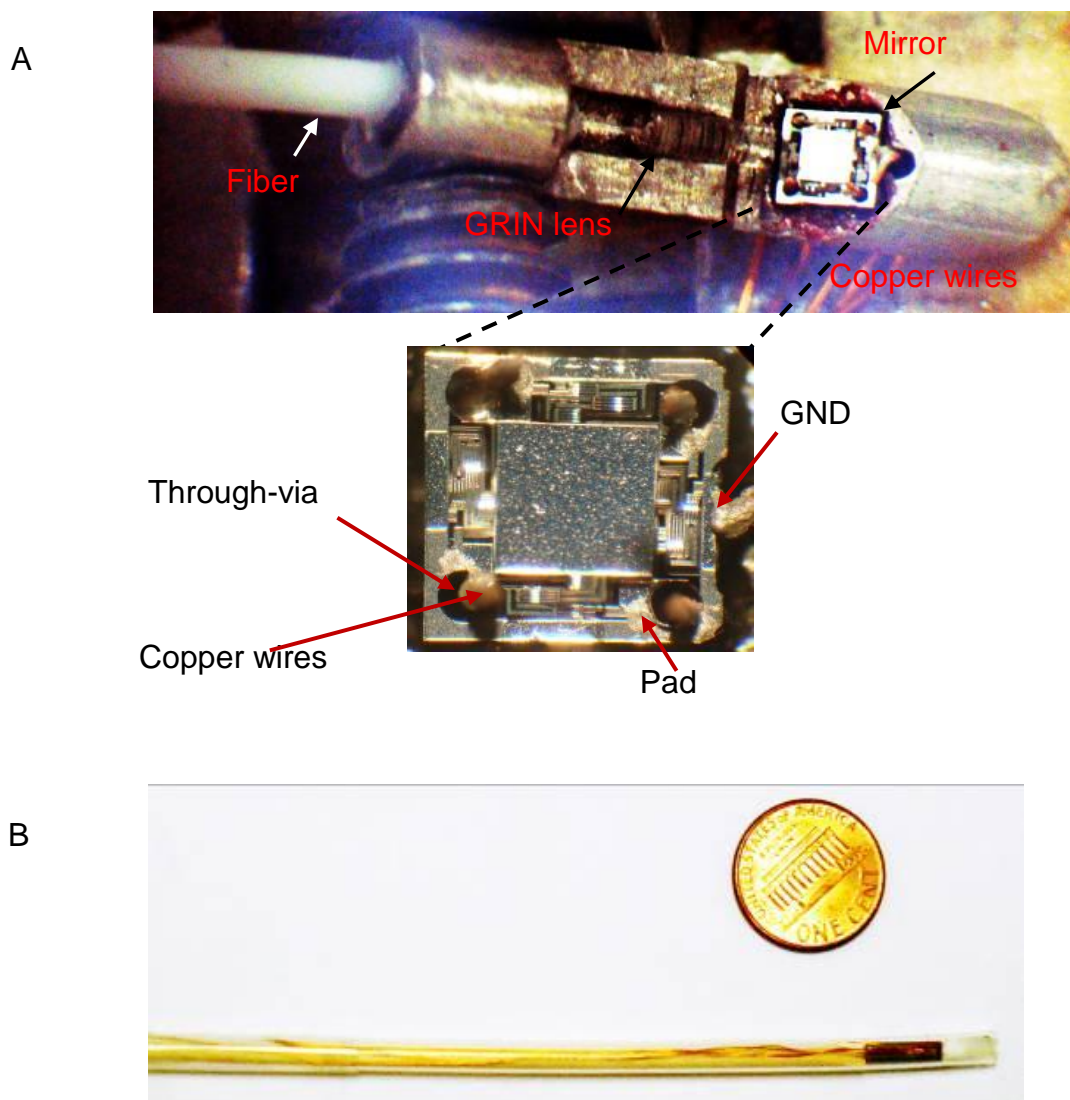
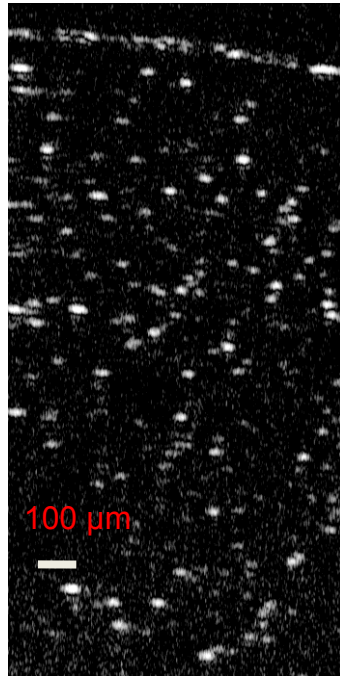


Figure 3-10. Photograph of the endoscopic OCT probe. A) Assembled OCT probe. B) Packaged OCT probe.

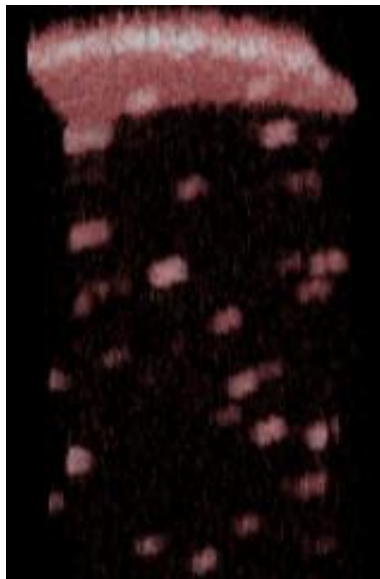


A

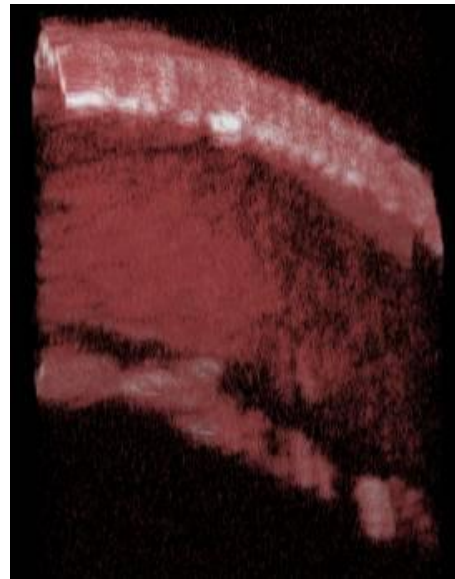


B

Figure 3-11. 2D cross-sectional OCT images by the endoscopic OCT system. A) Microspheres embedded in PDMS. B) Rat brain tissue.



A



B

Figure 3-12. 3D cross-sectional OCT images by the endoscopic OCT system. A) Microspheres embedded in PDMS. B) Rat brain tissue.

### 3.4 Chapter Summary

In this chapter, the design, process, and characterization of the TSV mirror has been presented. The TSV mirror is dedicated to further reduce the size of the endoscopic probe. An endoscopic OCT system with a compact probe design has been developed to demonstrate the capability of the TSV mirror. 2D and 3D OCT images of micro-particles and acute rat brain tissue with the endoscopic probe have been demonstrated. The MEMS mirror with through-silicon vias proves to be an effective way to shrink the endoscopic probe size as well as ease the wire bonding and probe assembling. This miniature probe, providing large scanning angle ( $\pm 16^\circ$ ) and fast scanning speed (resonance at 659 Hz) at low voltage (less than 3.6 V), is especially attractive for *in vivo* endoscopic OCT imaging.

## CHAPTER 4 MICROMIRRORS BASED ON A CURVED CONCENTRIC BIMORPH ACTUATOR

In this chapter, two new designs of electrothermal MEMS micromirrors with circular mirror plate and curved actuators will be present. These two mirrors are actuated by a curved actuator named curved concentric bimorph actuator (CCBA). The motivations for developing circular mirror and curved actuator will be first described. Then this chapter will show the design of CCBA, including the descriptions, analytical model and finite element model. After that the design, simulation results and characterization results of the two mirror design will be present.

### **4.1 Motivations for Circular Mirror and Curved Actuator**

Microelectromechanical system (MEMS) mirrors have gain wide applications in projection displays, optical switches, barcode readers, endoscopic biomedical imaging, Fourier transform spectrometers, tunable lasers, and adaptive optics, etc [95-104]. Among the major actuation mechanisms used in MEMS, electrothermal actuation stands out as a great fit for endoscopic optical scanner. Electrothermal actuators can provide large displacement and force at low voltage and achieve high fill factor.

Various bimorph-based electrothermal MEMS mirrors with different materials and fabrication processes have been reported [134-140]. These mirrors all have rectangular mirror plates and straight actuators. However, for optical applications where light beams are mostly circular or elliptical, circular or elliptical mirror plates are preferable, which can reduce the mass and thus increase the speed as well as leave more area for actuators for the same device footprint. Accordingly, instead of the conventionally used straight actuators, curved actuators can be utilized for higher area efficiency.

As illustrated in Figure 4-1, when a circular mirror plate is used, the straight actuators shown in Figure 4-1A leave some spare space unused, while the curved actuators in Figure 4-1B use the area more efficiently by matching the shape of the circular mirror plate. Also the circular chip (as shown in Figure 4-1B) could be utilized to match the shapes of the circular mirror plate and the curved actuators, so as to maximize the area efficiency. Circular mirror chips are preferred in applications that require MEMS mirrors to be integrated into miniature probes with circular cross-sections. For example, MEMS-based miniature endoscopic probes with stringent size requirements often have circular cross-sections and the sizes of the MEMS mirrors are often the limiting factors for the probe miniaturization. As illustrated in Figure 4-1C, a square mirror chip is not favorable as the shape mismatch limits the shrinking of the probe size, while a circular mirror chip would better fit into the probe and allow for the maximum miniaturization as shown in Figure 4-1D.

This work is dedicated to explore the feasibility of using curved bimorph actuators and circular mirror plates to maximize area efficiency and minimize lateral shift and tilting of the mirror plate without sacrificing the scan range.

## **4.2 Electrothermal CCBA Design**

### **4.1.1 Design Descriptions**

The schematic of the CCBA design are illustrated in Figure 4-2A in top view and Figure 4-2B in side view. Figure 4-2C shows a SEM of a CCBA of a fabricated device. For each CCBA, there are three segments of curved Aluminum/Tungsten bimorph beams, Bimorph I, Bimorph II and Bimorph III, and two rigid frames, Frame I and Frame II. The bimorphs and frames are both concentric arcs and they share a common arc center which is also the center of the mirror plate. There is a 20  $\mu\text{m}$ -thick single-crystal

silicon under Frame I and Frame II to provide rigidity to the frames. The rigid frames act as the vertical displacement amplifier.

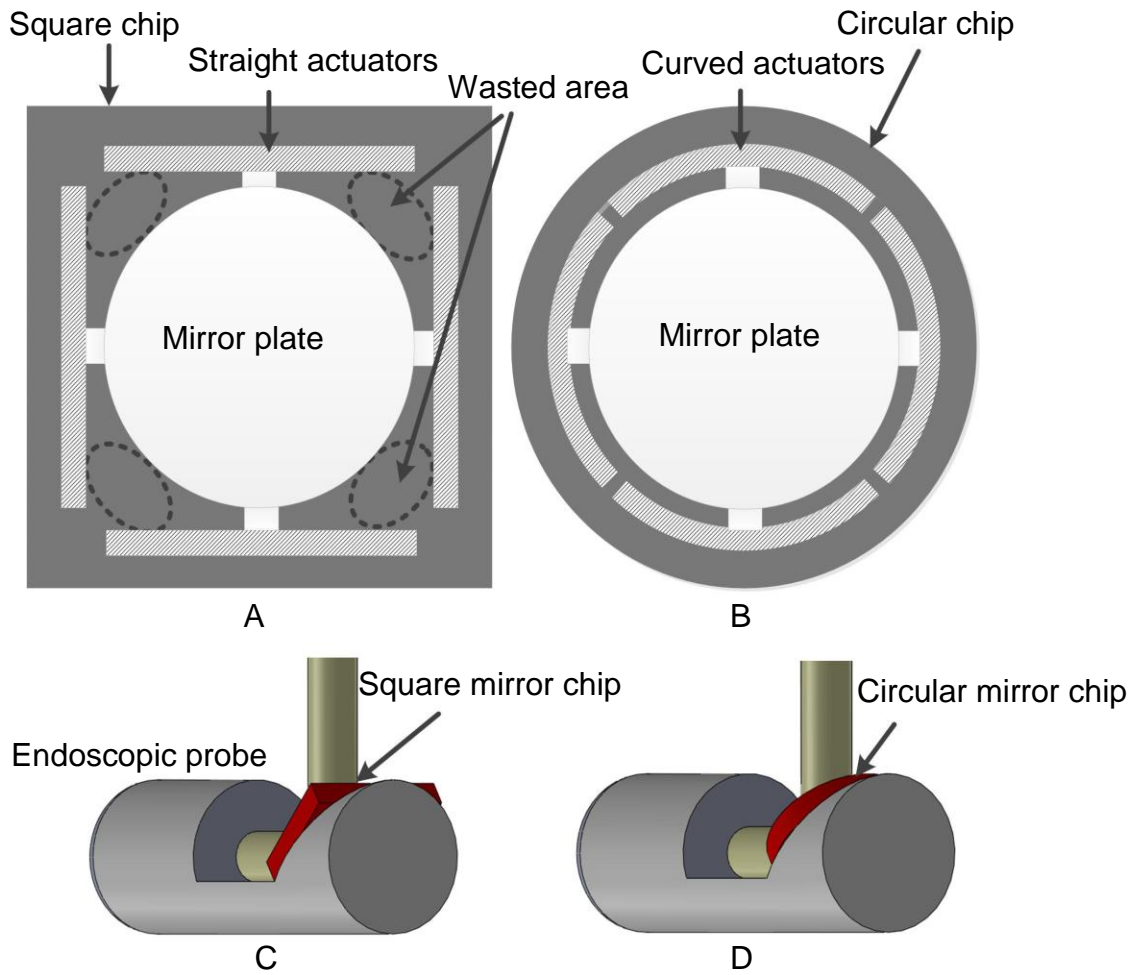


Figure 4-1. Schematic diagram to illustrate the advantages of curved actuators with circular mirror plate. A) Circular mirror plate with straight actuators. B) Circular mirror plate with curved actuators. C) An endoscopic probe with a square mirror chip. D) An endoscopic probe with a circular mirror chip.

The three bimorphs and two frames connect in a folded fashion and in series so as to save space and realize large displacement at the same time. The bimorphs will curl up after release, thus holding the mirror plate at an initial elevation. Upon a current passing through the heater embedded in the bimorphs, the induced Joule heating will cause the bimorphs to bend downward. Since the bending of Bimorph I and Bimorph III

is opposite to that of Bimorph II, the lengths of the three bimorphs can be carefully designed to cancel out the bending at the end of the actuator, resulting in a flat mirror plate with zero tilt. Meanwhile, the lengths of the two frames are set equal to cancel the lateral shift. The detailed analysis on the tilt and lateral shift compensation will be described in Section 4.1.2 of this chapter.

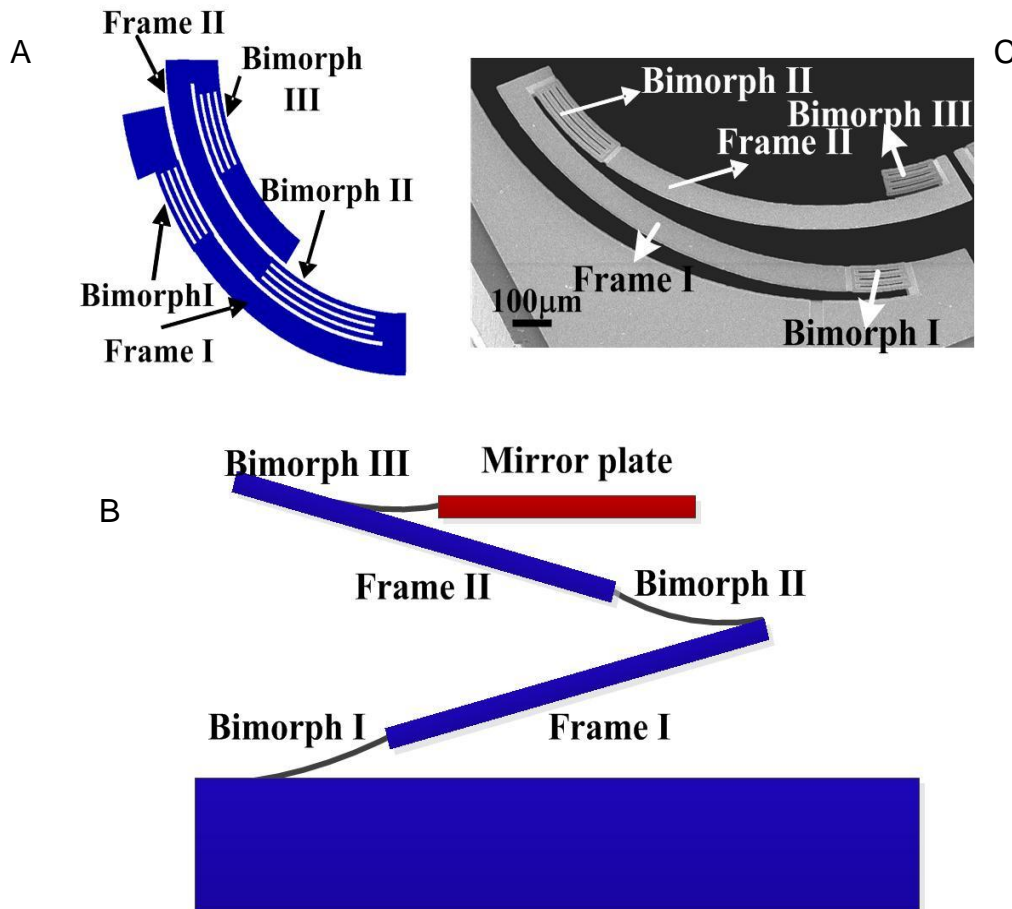


Figure 4-2. Schematic of design and SEM picture of the CCBA. A) Top-view schematic of the CCBA. B) Side-view schematic of the CCBA. C) SEM of a fabricated CCBA.

This curved concentric electrothermal actuator is designed based on a previously reported straight lateral-shift-free (LSF) actuator [136], but with different materials and different shape and arrangement. In previous straight LSF actuator design, Al and SiO<sub>2</sub> are used as the bimorph materials and Pt as the heater. In this new curved beam

design, Al and W are used as the bimorph materials for faster thermal response and better robustness, and W is also used for the heater, which simplifies the fabrication process.

#### 4.1.2 Analytical Model

The curved bimorphs used in the CCBA, compared with straight bimorphs, have certain unique characteristics, and show different actuation performances. The small deflection analysis of curved bimorphs was reported in [196]. For straight bimorphs, because of the different coefficients of thermal expansion of the two materials, the heating will produce out-of-plane bending of the bimorph beams. For curved bimorphs, upon temperature change, both out-of-plane bending and twisting occur, and the out-of-plane bending and twisting deformations are coupled. The analysis in [196] solves the curved beam deformation equations [197], the force and moment balance equations, and the strain continuity equation, and then gives the analytical expressions for the vertical deflection  $u(s)$  and twisting angle  $\beta(s)$  as follows:

$$u(s) = \frac{R^2 \left( -1 + \cos\left(\frac{s}{R}\right) \right) (\alpha_1 - \alpha_2) \Delta T}{\left( \frac{I_1 t_1}{2J_1} + \frac{I_2 t_2}{2J_2} + \left( \frac{1}{A_1 E_1} + \frac{1}{A_2 E_2} \right) \left( \frac{2}{t_1 + t_2} \right) (E_1 I_1 + E_2 I_2) \right)} \quad (4-1)$$

$$\beta(s) = u(s) / R \quad (4-2)$$

where  $R$  is the in-plane radius of curvature of the curved bimorph,  $s$  is the arc length along the bimorph,  $\alpha_i$  is the coefficient of thermal expansion of the  $i^{\text{th}}$  layer,  $\Delta T$  is the temperature rise,  $I_i$  is the area moment of inertia for out-of-plane bending of the  $i^{\text{th}}$

layer,  $E_i$  and  $t_i$  are the Young's modulus and thickness of the  $i^{\text{th}}$  layer, respectively, and  $J_i$  is defined as,

$$J_i = \iint_{A_i} \frac{u^2 dA_i}{1 - \frac{r}{R}} = \frac{t_i^3 R}{12} \ln \left( \frac{2R + w_i}{2R - w_i} \right) \quad (4-3)$$

, where  $w_i$  is the width of the  $i^{\text{th}}$  layer.

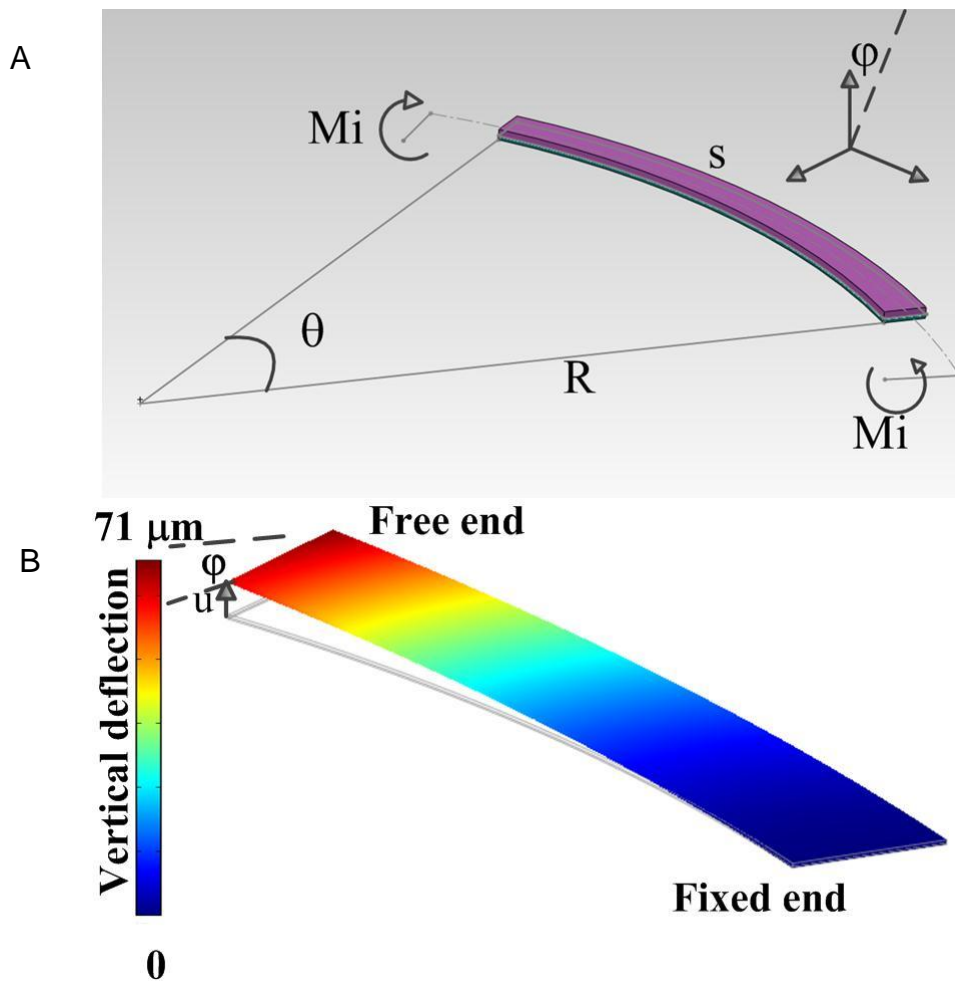


Figure 4-3. Schematic and FEA simulation results of a curved bimorph. A) Schematic of a curved bimorph. B) FE simulation results. Width of the bimorph:  $W= 60 \mu\text{m}$ , length of the bimorph  $S= 292 \mu\text{m}$  (center line); in-plane radius of curvature  $R=670 \mu\text{m}$  (center line). The maximum tip deflection under 100 K uniform temperature change is 71  $\mu\text{m}$ .

Figure 4-3A shows a curved bimorph with an in-plane radius of curvature  $R$  subject to the bending moment  $M_i$ . Figure 4-3B shows the finite element simulation of a curved bimorph under a uniform heating. Note that the simulation shows that the out-of-plane deflection of the bimorph beam varies along the radius direction, indicating a twisting deformation during the out-of-plane bending. The simulation results also show in-plane displacement, which may be due to the twisting motion. These inherent different characteristics of curved bimorph are demonstrated both in analysis and in simulation.

The schematic of the CCBA is shown in Figure 4-4. Bimorph I, Frame I, Bimorph II, Frame II and Bimorph III are all concentric with a common center, O. The in-plane radius of curvature of Bimorph I and Frame I is denoted by  $R_1$ . The in-plane radius of curvature of Bimorph II and Frame II is  $R_2$ . And the in-plane radius of curvature of Bimorph III is denoted by  $R_3$ . The in-plane central angles of Bimorph I, Frame I, Bimorph II, Frame II and Bimorph III are  $\phi_{1b}, \phi_{1f}, \phi_{2b}, \phi_{2f}, \phi_{3b}$ , respectively.  $u_i$  denotes the out-of-plane deflection of the  $i^{\text{th}}$  bimorph, while  $\beta_i$  denotes the twisting angle of the  $i^{\text{th}}$  bimorph.  $u_i$  and  $\beta_i$  can be calculated by Equation 4-1 and Equation 4-2.

For small deflection, the out-of-plane tilt angle  $\theta_i$  at the tip of the  $i^{\text{th}}$  bimorph can be approximated by as:

$$\theta_i = \frac{du_i(s)}{ds} = \frac{du_i(s)}{R_i d\phi} = \eta_i(R_i) \sin\left(\frac{s}{R_i}\right) \quad (4-4)$$

$$\text{, where } \eta_i(R_i) = \frac{-R_i^2(\alpha_1 - \alpha_2)\Delta T}{\left(\frac{I_1 t_1}{2J_{1i}} + \frac{I_2 t_2}{2J_{2i}} + \left(\frac{1}{A_1 E_1} + \frac{1}{A_2 E_2}\right)\left(\frac{2}{t_1 + t_2}\right)(E_1 I_1 + E_2 I_2)\right)} \quad (4-5)$$

To cancel out the bending at the end of the actuator for a flat mirror plate, the balancing condition  $|\theta_1| + |\theta_3| = |\theta_2|$  needs to be met. We set the combined length of the first and third bimorph beams to equal to that of the second bimorph beam, and then select the proper  $R_i$  accordingly using Equation 4-4 and Equation 4-5.

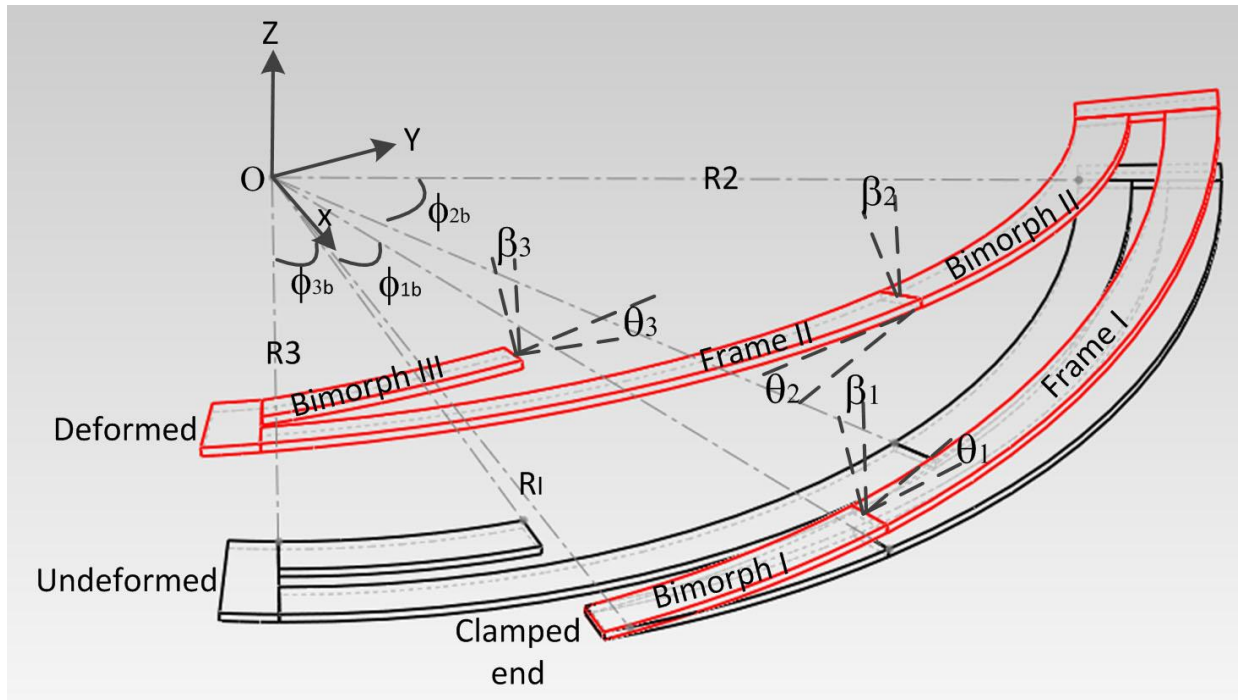


Figure 4-4. Schematic of the CCBA

Since the frames between the bimorphs are supported by a thick single-crystal silicon layer, we assume that the frames are rigid without any deformations during the actuation. The spatial coordinates of points along the frames and bimorphs are determined by the bending and twisting of the three bimorphs, and the dimensions and 3D spatial relations of all the beams. Several linear translations and rotations of the coordinate system are performed in order to obtain the 3D shape of the center line of the CCBA under uniform heating. In the original Cartesian system, the origin is the

common center of the concentric arcs, and the starting point of Bimorph I is on the x axis. The coordinate system is first linearly translated to the end tip of the center line of Bimorph I by matrix  $M_1$ , and it is then rotated about the local z axis by  $\phi_{1b}$  to align to the radius direction of the bimorph I by  $M_2$ . This is followed by a rotation about the local x axis by  $\theta_1$  for the bending behavior of Bimorph I by  $M_3$ , and another rotation about the local y axis by  $\beta_1$  to lead to the post-twisting state by  $M_4$ . The linear translation matrix  $M_5$  and three rotation matrices  $M_6$ ,  $M_7$  and  $M_8$  are applied to Bimorph II in a same way as above for Bimorph I. After applying  $M_8$ , we have the coordinates of the end tip of the bimorph III in the local coordinate system, and then transform them back to the original coordinate system to obtain the final (x, y, z) of the end tip of the CCBA. Any point along the 3D curve (center line) can be expressed in the local coordinates and then translated back to the original coordinates using these transform matrices.

The matrices discussed above are as follows:

$$M_1 = \begin{pmatrix} R_1 \cos(\phi_{1b}) \\ R_1 \sin(\phi_{1b}) \\ u_1 \end{pmatrix} \quad (4-6)$$

$$M_2 = \begin{pmatrix} \cos \phi_{1b} & -\sin \phi_{1b} & 0 \\ \sin \phi_{1b} & \cos \phi_{1b} & 0 \\ 0 & 0 & 1 \end{pmatrix} \quad (4-7)$$

$$M_3 = \begin{pmatrix} 1 & 0 & 0 \\ 0 & \cos \theta_1 & -\sin \theta_1 \\ 0 & \sin \theta_1 & \cos \theta_1 \end{pmatrix} \quad (4-8)$$

$$M_4 = \begin{pmatrix} \cos \beta_1 & 0 & -\sin \beta_1 \\ 0 & 1 & 0 \\ \sin \beta_1 & 0 & \cos \beta_1 \end{pmatrix} \quad (4-9)$$

$$M_5 = \begin{pmatrix} -(R_1 - R_2 \cos(\phi_{1f} - \phi_{2b})) \\ R_1 \sin(\phi_{1f} - \phi_{2b}) \\ u_2 \end{pmatrix} \quad (4-10)$$

$$M_6 = \begin{pmatrix} \cos(\phi_{1f} - \phi_{2b}) & -\sin(\phi_{1f} - \phi_{2b}) & 0 \\ \sin(\phi_{1f} - \phi_{2b}) & \cos(\phi_{1f} - \phi_{2b}) & 0 \\ 0 & 0 & 1 \end{pmatrix} \quad (4-11)$$

$$M_7 = \begin{pmatrix} 1 & 0 & 0 \\ 0 & \cos \theta_2 & \sin \theta_2 \\ 0 & -\sin \theta_2 & \cos \theta_2 \end{pmatrix} \quad (4-12)$$

$$M_8 = \begin{pmatrix} \cos \beta_2 & 0 & \sin \beta_2 \\ 0 & 1 & 0 \\ -\sin \beta_2 & 0 & \cos \beta_2 \end{pmatrix} \quad (4-13)$$

The coordinates of the end tip of Bimorph III at the local coordinate system after  $M_1$  to  $M_8$  transformations are:

$$N_8 = \begin{pmatrix} x_8 \\ y_8 \\ z_8 \end{pmatrix} = \begin{pmatrix} -R_2 + R_3 \cos(\phi_{2f} - \phi_{3b}) \\ -R_3 \sin(\phi_{2f} - \phi_{3b}) \\ u_3 \end{pmatrix} \quad (4-14)$$

Then, we can transform  $N_8$  to the original coordinates,

$$N = \begin{pmatrix} x \\ y \\ z \end{pmatrix} = M_1 + M_2 M_3 M_4 (M_5 + M_6 M_7 M_8 N_8) \quad (4-15)$$

, where  $z$  is the total vertical displacement at the tip of the CCBA, and the in-plane movement of the actuator can be calculated from  $x$  and  $y$ .

The 3D curve for the center line is calculated based on the above analysis and plotted in Figure 4-5 using Matlab.

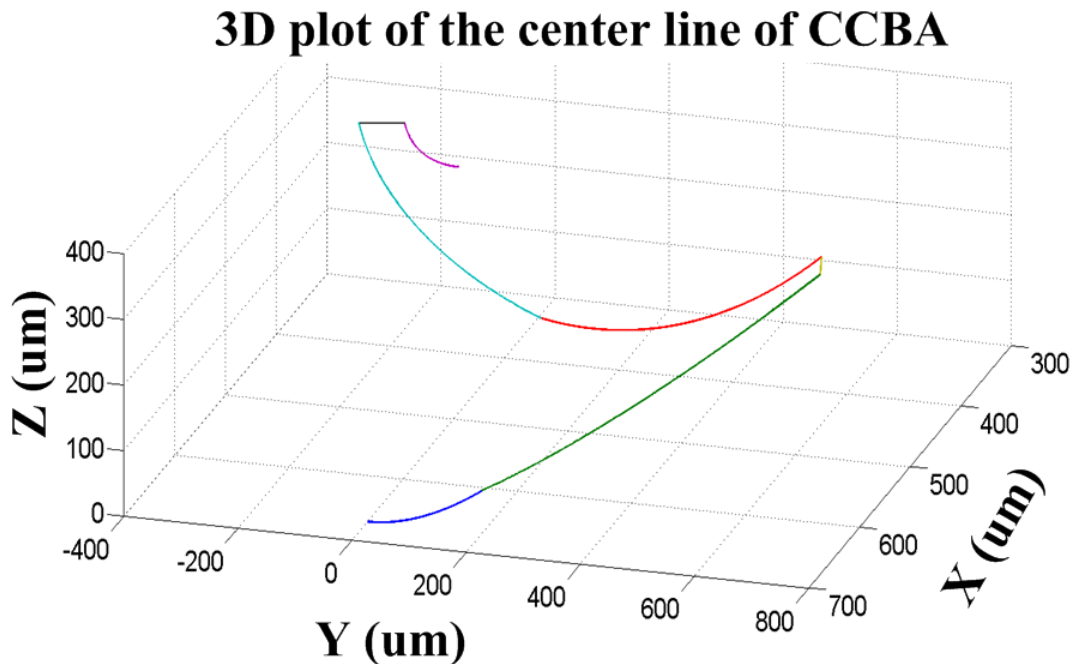


Figure 4-5. 3D plot of the center line of the CCBA. The calculated out-of-plane deflection is 311.5  $\mu\text{m}$  under 150 K temperature change.

#### 4.1.3 Finite Element Analysis

Finite element modeling and simulations were performed using COMSOL Multiphysics to better understand the behavior of the CCBA actuator. The FE model is shown in Figure 4-6. The tip of the Bimorph III where the mirror plate is attached is nearly flat in the lateral bending direction, but the twisting is quite obvious in the CCBA and the end tip also twists. The out-of-plane displacement versus temperature change from both analysis and FE simulation are shown in Figure 4-7. There is certain discrepancy between the analytical and FE simulation results. The discrepancy is small at low temperature, but becomes noticeable at high temperature. This is mainly because of the small deflection approximation in the analytical model.

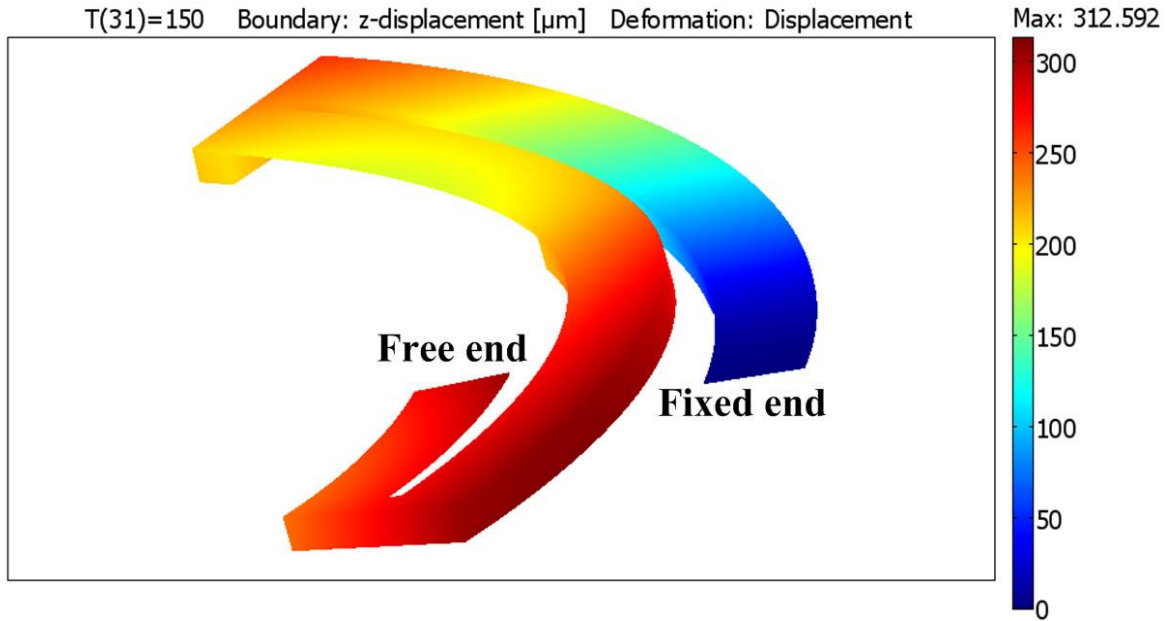


Figure 4-6. 3D finite element model of the CCBA. The out-of-plane displacement at the free end of the center line is  $289.8 \mu\text{m}$  under 150 K temperature change.

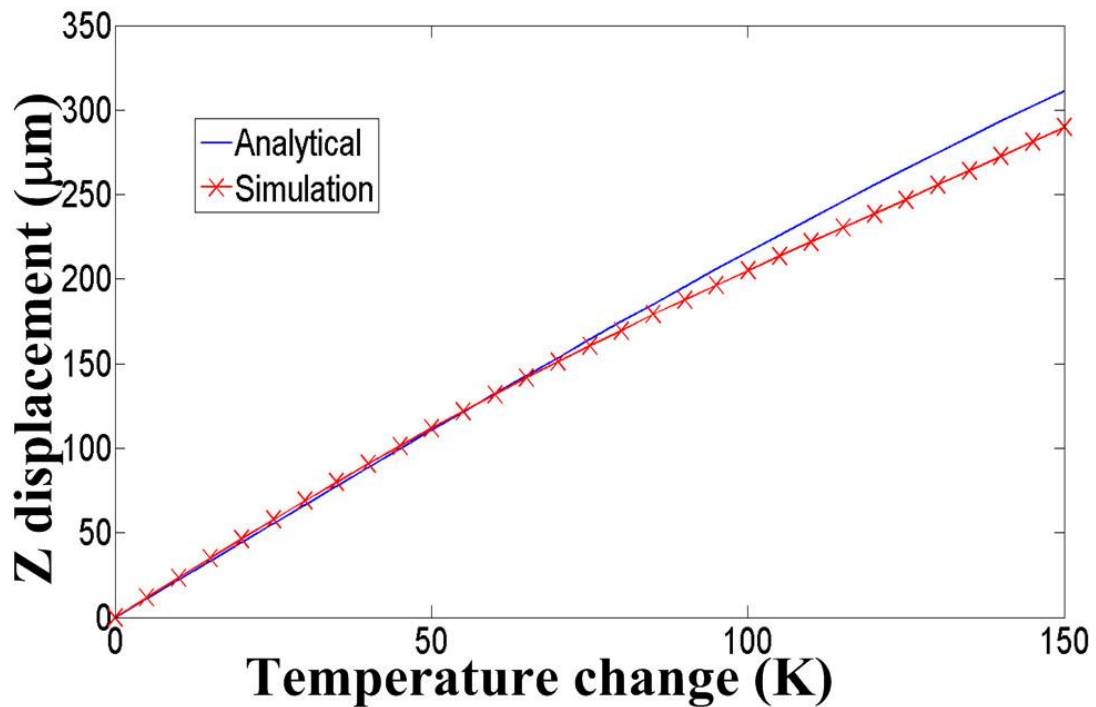


Figure 4-7. Out-of-plane displacement of the CCBA vs. temperature change

### 4.3 MEMS Micromirrors Based on CCBA

#### 4.3.1 Design and Simulation

Two MEMS mirrors based on this CCBA actuator are designed, fabricated and tested to demonstrate the capability of this actuator. Type I mirror is a tip-tilt-piston mirror with large tip-tilt scan angle and large piston displacement at low voltage. Type II mirror, a piston-only mirror, shows slightly smaller piston scan range than Type I mirror, but achieve even smaller lateral shift and tilt, and is especially attractive for applications where tilt tolerance is tight, for example, for MEMS-mirror based Fourier transform spectrometers.

Figure 4-8A and Figure 4-8B show the schematic and SEM picture of the Type I tip-tilt-piston micromirror. The diameter of the mirror plate is 1 mm. The footprint of the device is 2 mm × 2 mm. Note that the corners of this mirror can be etched away during the fabrication to form a circular chip. In this paper, we only packaged and characterized square chips for easy handling.

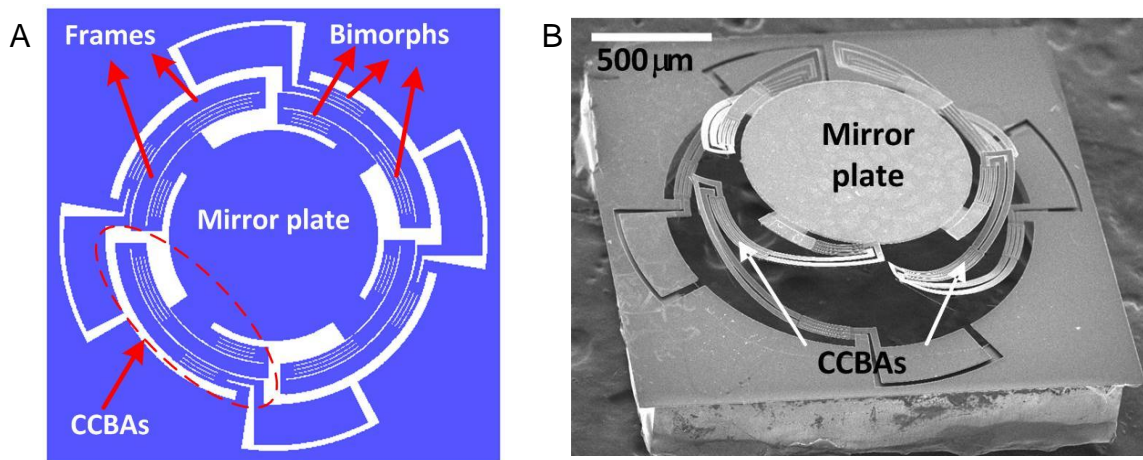


Figure 4-8. Schematic design and SEM picture of Type I tip-tilt-piston mirror. A) Schematic of design. B) SEM of a fabricated device.

There are four sets of symmetric CCBA's supporting the circular mirror plate. The four actuators surround the circular mirror plate and share the center of the mirror plate as the common center. The complete symmetry of the layout together with the confinement by the rigid mirror plate cancels out the components of the in-plane movement that is directed towards the center of the mirror plate. At the same time, due to the symmetry, the twisting moments of the opposing CCBA pairs balance each other, resulting in zero tilt of the mirror plate. By comparing the FEM simulations of a CCBA actuator only (Figure 4-6) and a complete micromirror supported by the same four CCBA actuators (Figure 4-9A), it is found that the vertical displacement of the mirror plate (Figure 4-9A) is larger than that of the individual free-ended CCBA (Figure 4-6). With the same temperature change of 150 K, the individual free-ended CCBA shows a 289.8  $\mu\text{m}$  out-of-plane deflection at the free end of the CCBA, while the mirror plate supported by the four of the same CCBA shows a 344  $\mu\text{m}$  out-of-plane deflection at the CCBA end that is connected to the mirror plate. This may prove that the complete symmetry and the confinement by the rigid mirror plate reduce the pushing-down effect of individual CCBA actuators from twisting. It is also found that although the end tip of the free-ended individual CCBA (Figure 4-6) is twisted, the mirror plate is completely flat when supported by four symmetrically distributed CCBA's (Figure 4-9A). This demonstrates that the symmetry cancels out the twisting moment and keeps the mirror plate flat without initial tilting. Also, in spite of the in-plane displacement shown in individual CCBA's, no lateral shift of the mirror center is observed from the simulation. The inherent issues of curved actuators can be addressed to a large extent by proper symmetric arrangement of the actuators during the mirror device design.

Note that there is small in-plane rotation of the mirror plate about the mirror plate center, which is due to the component of the in-plane movement that is in the direction of the tangent of the mirror plate as illustrated by the arrows in Figure 4-9A. The in-plane rotation angles are calculated as the degrees that the points on the mirror plate are rotated about the mirror center at different temperatures plotted in Figure 4-9B.

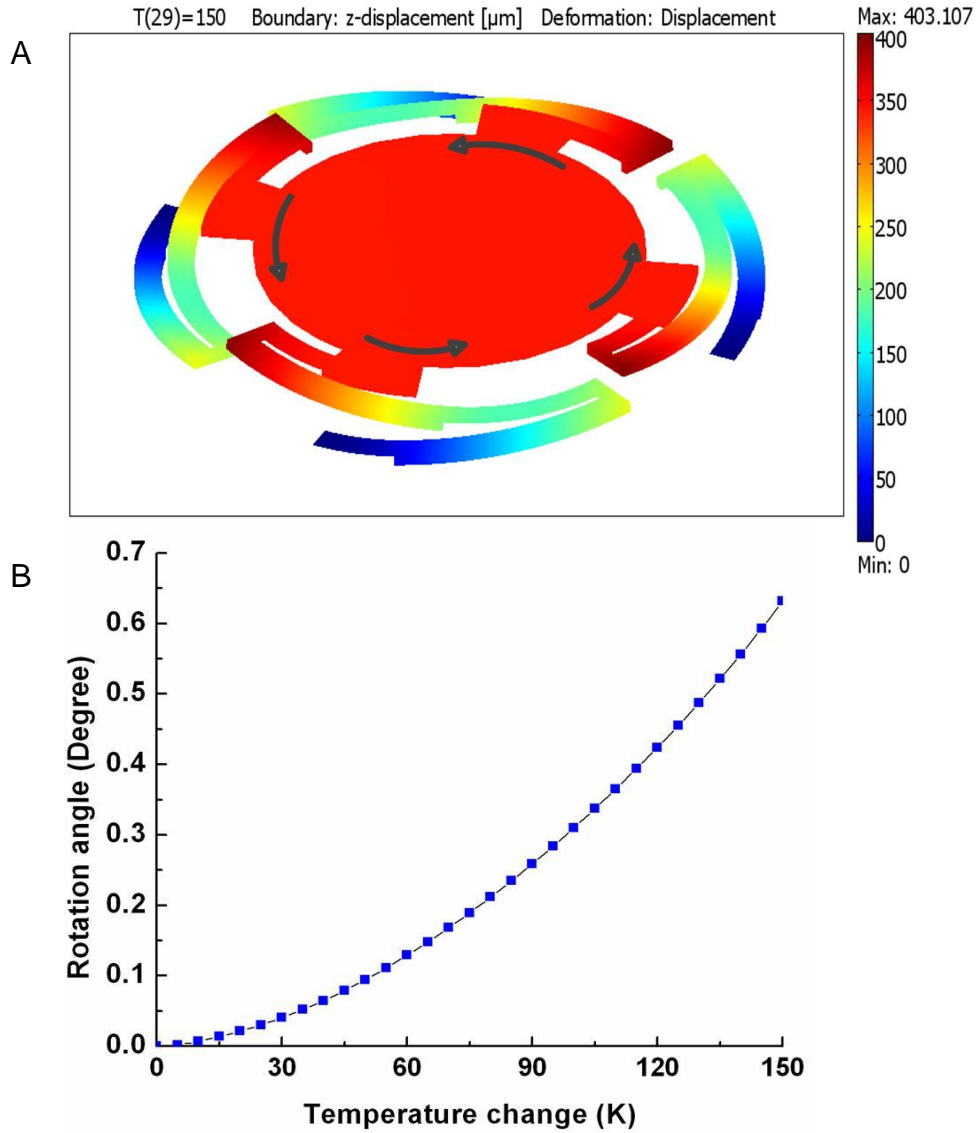


Figure 4-9. FEM simulation results of Type I mirror. A) 3D finite element model of Type I mirror by COMSOL. The out-of-plane deflection of the mirror plate is 344  $\mu\text{m}$  under 150 K temperature change. The arrows show the direction of the in-plane rotation. B) In-plane rotation angle of the mirror plate vs. temperature change.

As shown in Figure 4-10A and Figure 4-10B, the piston-only micromirror has four CCBAs and two radial bimorph beams. The four CCBAs are grouped into two pairs. Each pair is connected in series and linked by a set of radial bimorph beams. Each set of radial bimorph beams surrounds about one half of the mirror plate. Different from Type I mirror in which the four CCBAs are connected to the mirror plate at four separate spots, Type II mirror has almost the whole mirror plate surrounded and supported by radial bimorph beams. The enhanced constraint and support to the mirror plate improves the stability and robustness of the mirror plate and leads to smaller lateral shift and tilt.

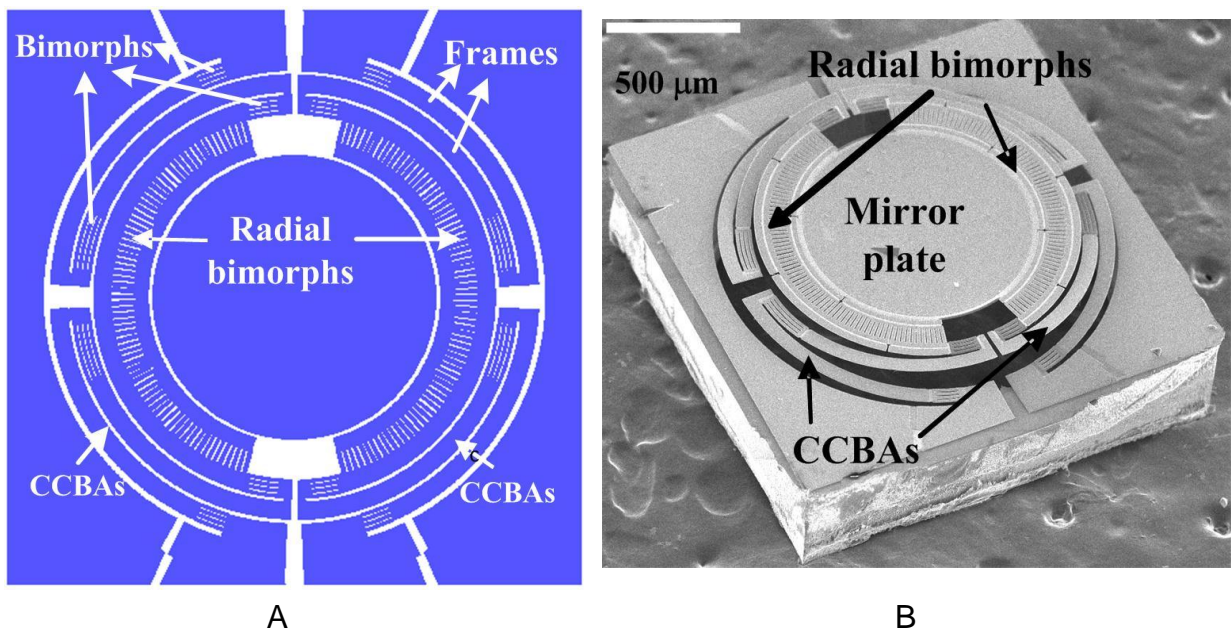


Figure 4-10. Schematic design and SEM picture of Type II piston-only mirror. A) Schematic of design. B) SEM of a fabricated device.

The lateral shift and tilting of Type II mirror are only  $3\ \mu\text{m}$  and  $0.4^\circ$  through the entire  $200\ \mu\text{m}$  vertical range. While the symmetrical layout of these two pairs of CCBA already help cancel out the in-plane motion of the CCBA, the radial bimorph beams further offset the in-plane motion. The in-plane movement of the CCBA is towards the

center of the mirror plate when the CCBA's are bended up and the mirror plate is elevated. Under the same condition, the radial bimorphs will curl up. The out-of-plane bending of the radial bimorphs will induce a vertical displacement, as well as an in-plane displacement at the tip of the radial bimorphs that points away from the center of the mirror plate. The in-plane displacements introduced by the radial bimorphs are in opposite directions to the in-plane movements caused by the CCBA's. Therefore the in-plane movements are compensated to some extent. The radial bimorph also helps cushion the stress on the mirror plate. The finite element model of the Type II mirror is shown in Figure 4-11. Different from Type I mirror, there is no in-plane rotation of the mirror plate in this Type II\_mirror. This is because that for Type II mirror, the CCBA's are in mirrored arrangement and the inverse in-plane rotation directions of these CCBA's cancel out each other. The diameter of the mirror plate is 0.9 mm and the footprint is 2 mm × 2 mm.

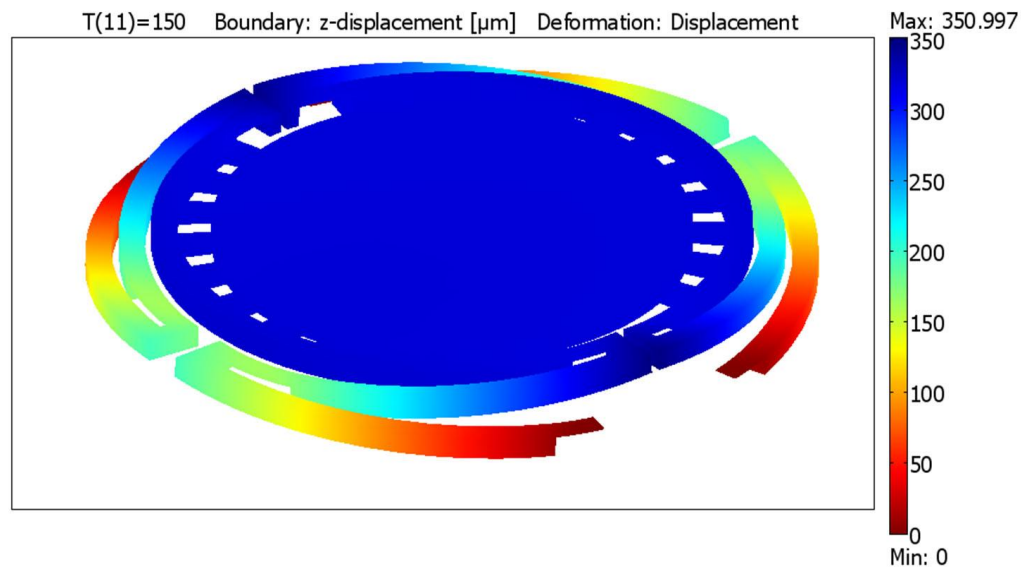


Figure 4-11. 3D finite element model of Type II mirror. The out-of-plane deflection of the mirror plate is about 320 μm under 150 K temperature change.

### 4.3.2 Device Fabrication

The MEMS mirrors are fabricated by a combined surface and bulk micromachining process, which is outlined in Figure 4-12.

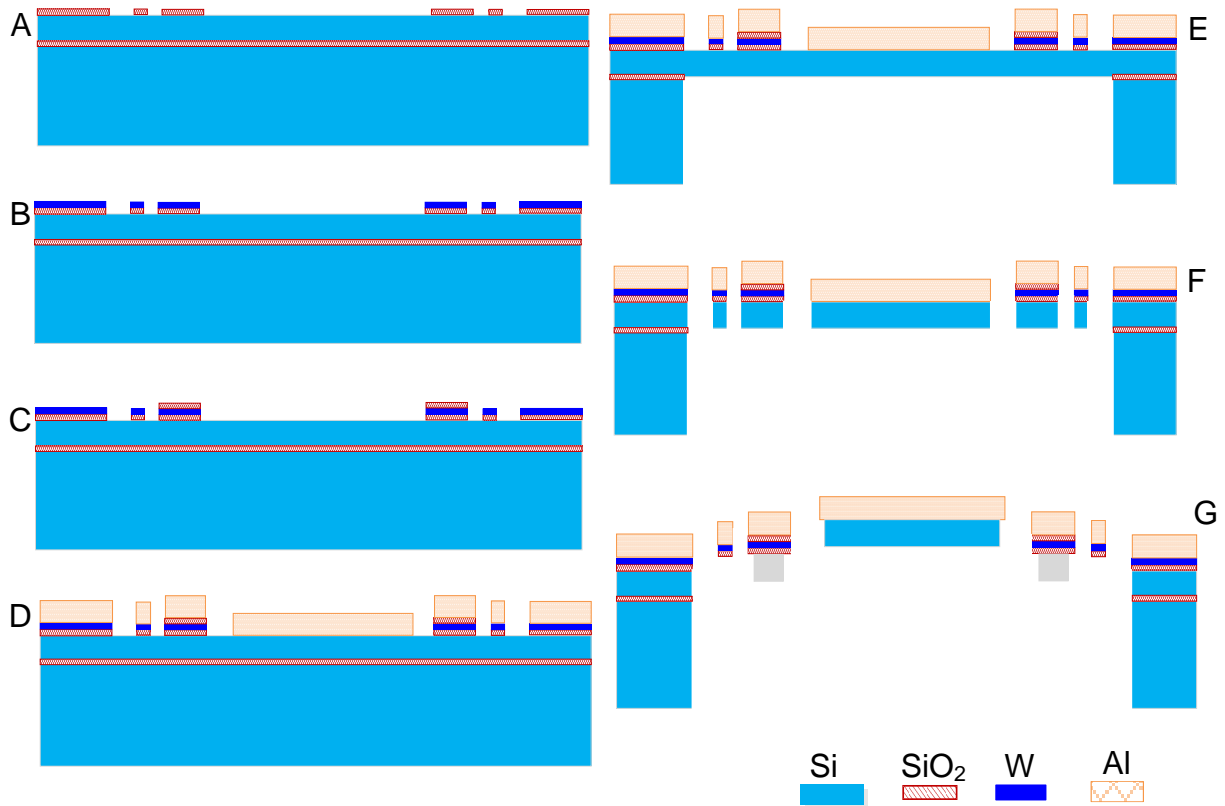


Figure 4-12. Process flow of MEMS mirrors based on CCBA.

The process starts with a 0.1  $\mu\text{m}$ -thick PECVD SiO<sub>2</sub> isolation layer deposition and patterning on a SOI wafer A), followed by a 0.6  $\mu\text{m}$ -thick W heater layer patterning by sputtering and lift-off B). A 0.2  $\mu\text{m}$  dielectric SiO<sub>2</sub> layer is then deposited and etched C), followed by a 1  $\mu\text{m}$  e-beam evaporated Al layer and Al lift-off for the top layer of bimorph beams as well as the mirror plate surface D). After that, a back-side DRIE silicon etch is done, followed by a SiO<sub>2</sub> RIE dry etch, leaving the 20  $\mu\text{m}$  single crystal silicon as the support for the frames and the mirror plate E). Then, an anisotropic silicon

etch is carried out from the front-side until the device layer silicon is etched through F). The final step the releasing step is done by the front-side silicon isotropic etching which undercuts the device layer single crystal silicon underneath the bimorphs to finally release the whole structure G).

Al and W are chosen as the active layer of the bimorphs because they have large difference in CTE to achieve high responsivity. The CTE difference of Al/W is about  $19.1 \times 10^{-6}/\text{K}$  [198]. However, lower responsivity is expected when compared with Al/SiO<sub>2</sub> bimorph. The CTE difference of Al/W is smaller than that of Al/SiO<sub>2</sub> ( $22.6 \times 10^{-6}/\text{K}$ ) [199]. Both Al and W are metal materials with high thermal diffusivities, which means a faster response and shorter thermal delay compared to Al/SiO<sub>2</sub> or polymer-based bimorphs. In addition, W can serve as both an active layer of the bimorphs and the heater, which simplifies the process and reduces the cost. These materials are also standard materials for IC fabrication with easy processing.

### **4.3.3 Device Characterization**

To measure the vertical displacement, as well as the lateral shift and tilting through the vertical scan, the mirror was operated at the piston mode by simultaneously driving all the actuators with a same dc voltage, and gradually changing the voltage by small steps. The device was placed under an Olympus BX51 microscope equipped with a QC200 microposition recorder. After each voltage change step, the microscope was refocused onto the mirror plate and the coordinates of multiple points on the mirror plate were recorded. Those recorded coordinates were used to determine the vertical displacement, lateral shift, and tilting, which are plotted in Figure 4-13 for a Type I tip-tilt-piston mirror. The measured vertical displacement of the tip-tilt-piston mirror was

227  $\mu\text{m}$  at 0.8 V (Figure 4-13A) and 275 mW (Figure 4-13B). It is shown in Figure 4-13C that the lateral shift and the tilt angle of the mirror plate were less than 7  $\mu\text{m}$  and 0.7° through the whole 227  $\mu\text{m}$  piston movement.

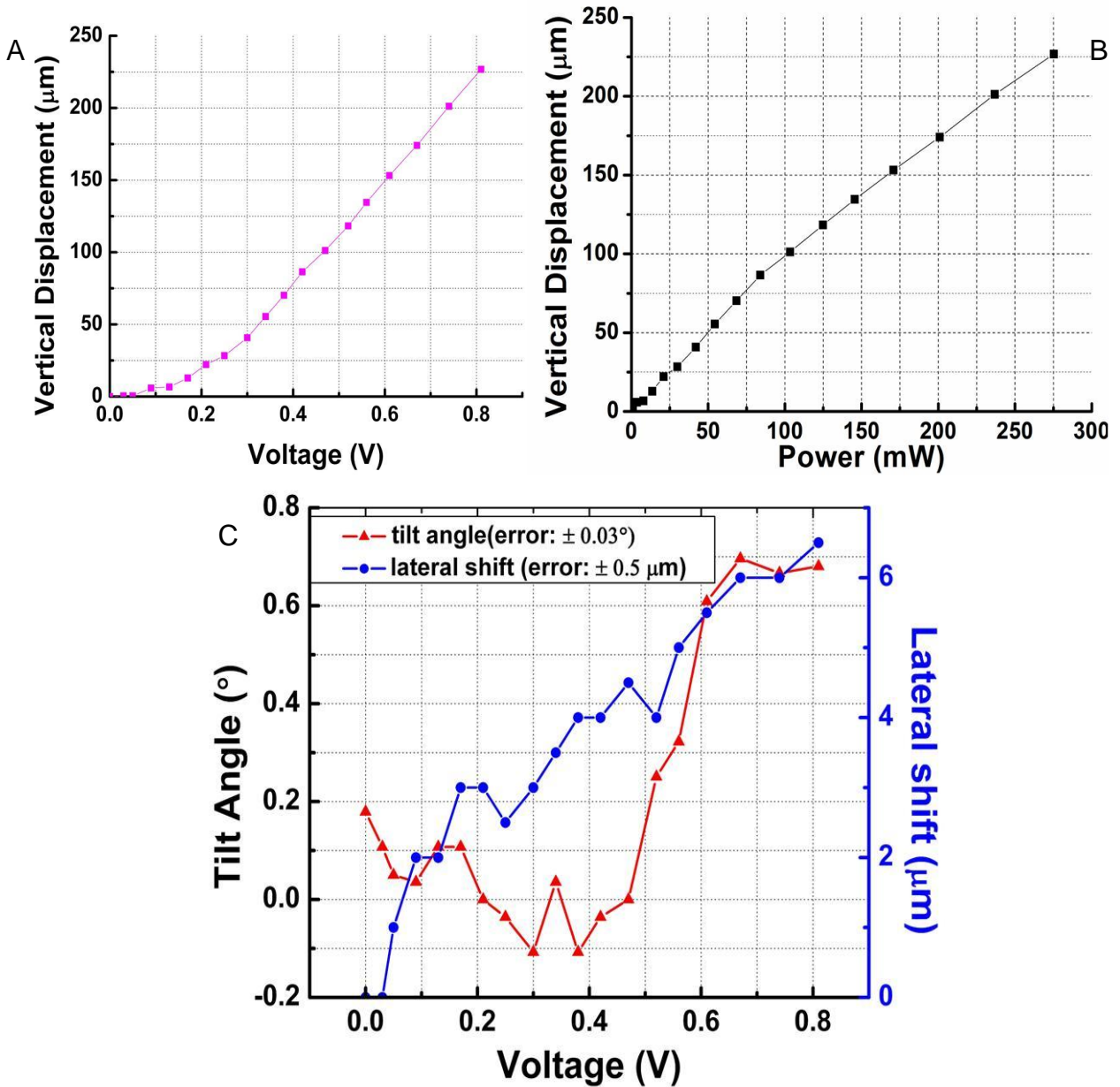


Figure 4-13. Type I Tip-tilt-piston mirror static measurement of piston movement. A) Vertical displacement vs. dc voltage. B) Vertical displacement vs. power. C) Tilt and lateral shift.

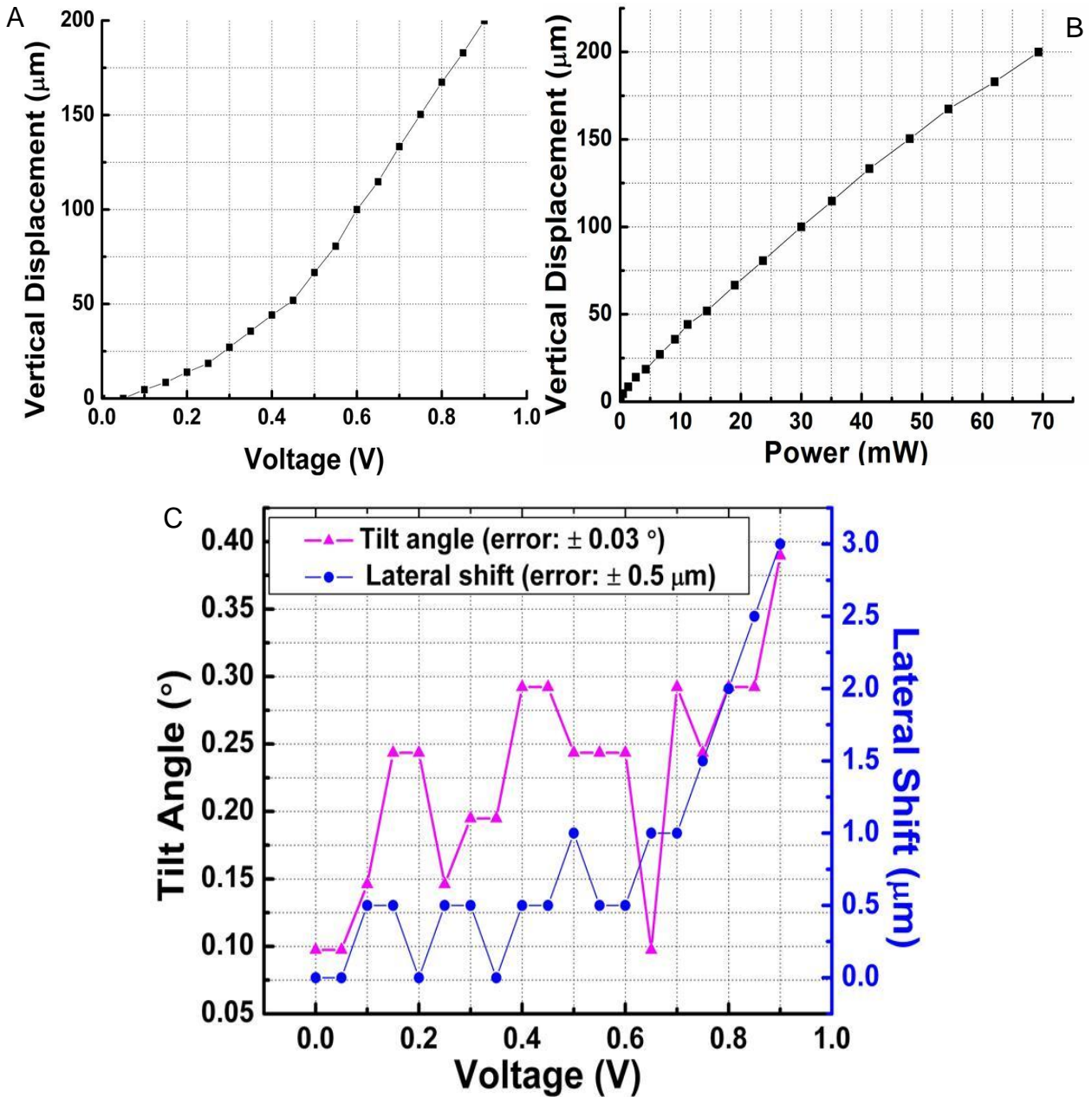


Figure 4-14. Type II piston-only mirror static measurement of piston movement. A) Vertical displacement vs. dc voltage. B) Vertical displacement vs. power. C) Tilt and lateral shift.

The measurement error of the tilt angle is about  $\pm 0.03^\circ$  determined by the accuracy of the QC200 microposition recorder equipped with an Olympus BX51 microscope. Six devices have been tested and each device was tested 3 or 4 times. The repeatability of each single device was within 1%, while from device to device, the

variations were within 5%. Figure 4-13C also shows that both the lateral shift and tilt angle increase with increasing drive voltage. This indicates that the lateral shift and tilt did not change randomly but the four actuators had different responsivities, which are mainly caused by process variations. The process variations lead to both mechanical and electrical variations.

The piston displacement, lateral shift and tilting measurement for Type II mirrors was done in a same way as in Type I mirrors. As shown in Figure 4-14A, a large vertical displacement of about 200  $\mu\text{m}$  was achieved by a Type II mirror at only 0.9 V driving voltage.

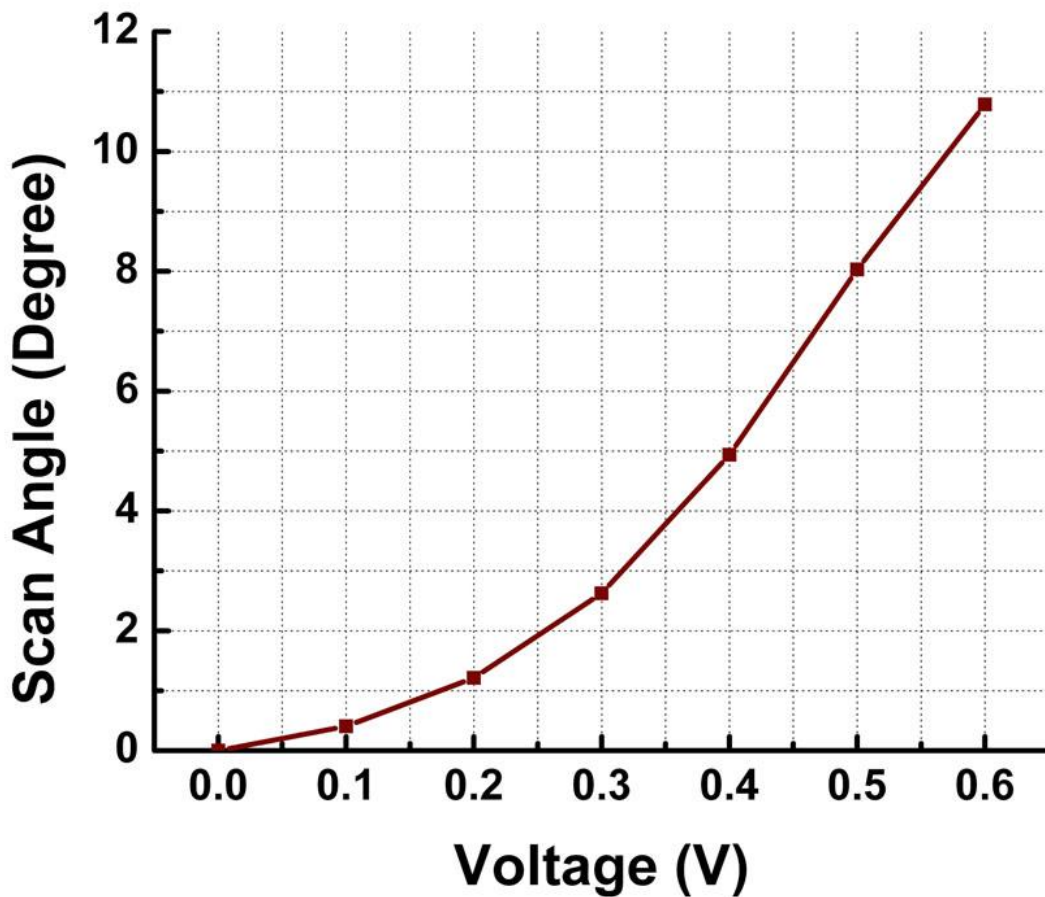


Figure 4-15. Type I Tip-tilt-piston mirror: scan angle vs. applied voltage

The power consumed at 0.9 V is 69 mW (Figure 4-14B). Note that the curved actuator design reported here has smaller actuation range than that of the straight lateral-shift-free (LSF) actuator design as reported in [136]. This is mainly due to the twisting deformation coupled with the bending deformation in the curved actuators. The lateral shift and tilting of this mirror design are only  $3\ \mu\text{m}$  and  $0.4^\circ$  through the entire vertical range (shown in Figure 4-14C). The lateral shift and the mirror tilt of this design and straight LSF actuator based mirror design [136] are in the same range.

Figure 4-15 is the measurement result for the rotation angle versus the applied voltage of a Type I mirror. Optical scan angles of  $\pm 11^\circ$  in both x- and y-axis are achieved at only 0.6 V for this mirror.

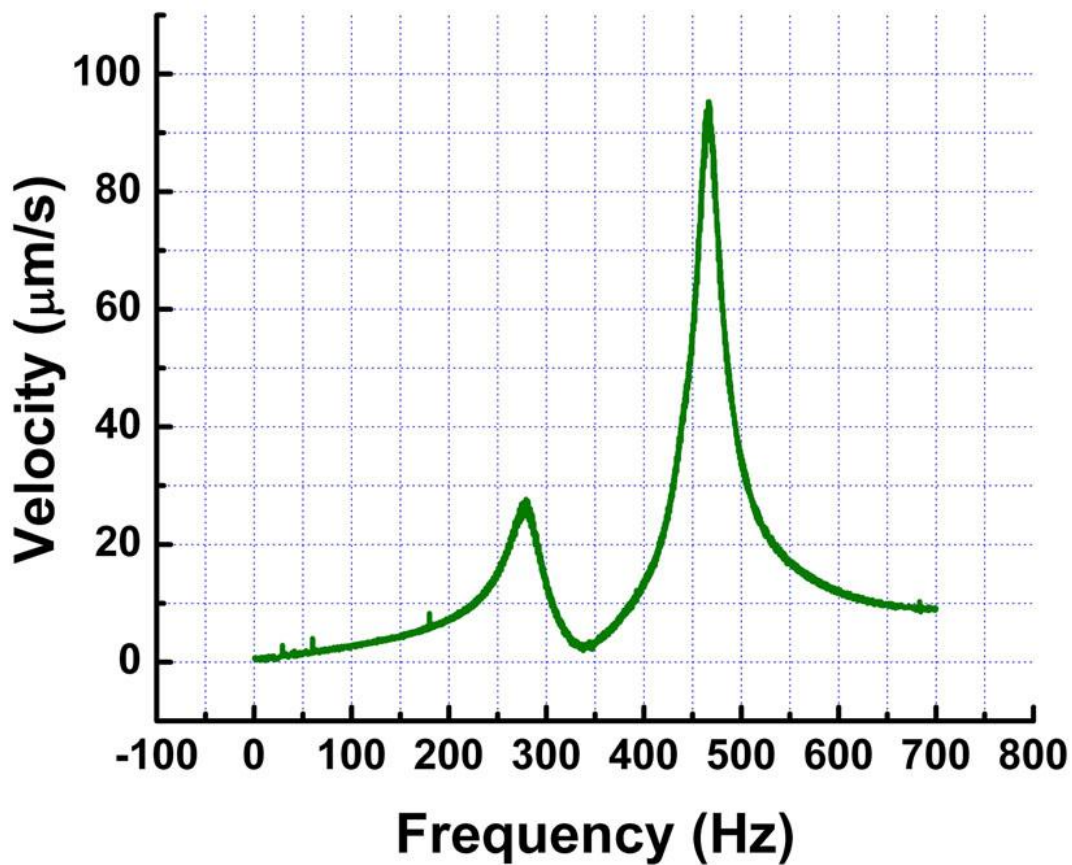


Figure 4-16. Frequency response of Type I tip-tilt-piston mirror

The frequency responses of Type I mirrors were measured using a Polytec OFV-511 laser Doppler vibrometer. The resonance frequencies of the piston mode and tilt mode of the Type I mirror were found to be 272 Hz and 464 Hz, respectively, as shown in Figure 4-16.

The frequency responses of Type II mirror was also measured with a Polytec OFV-511 laser Doppler vibrometer. A first mechanical resonance of 197 Hz is observed for the Type II mirror as plotted in Figure 4-17.

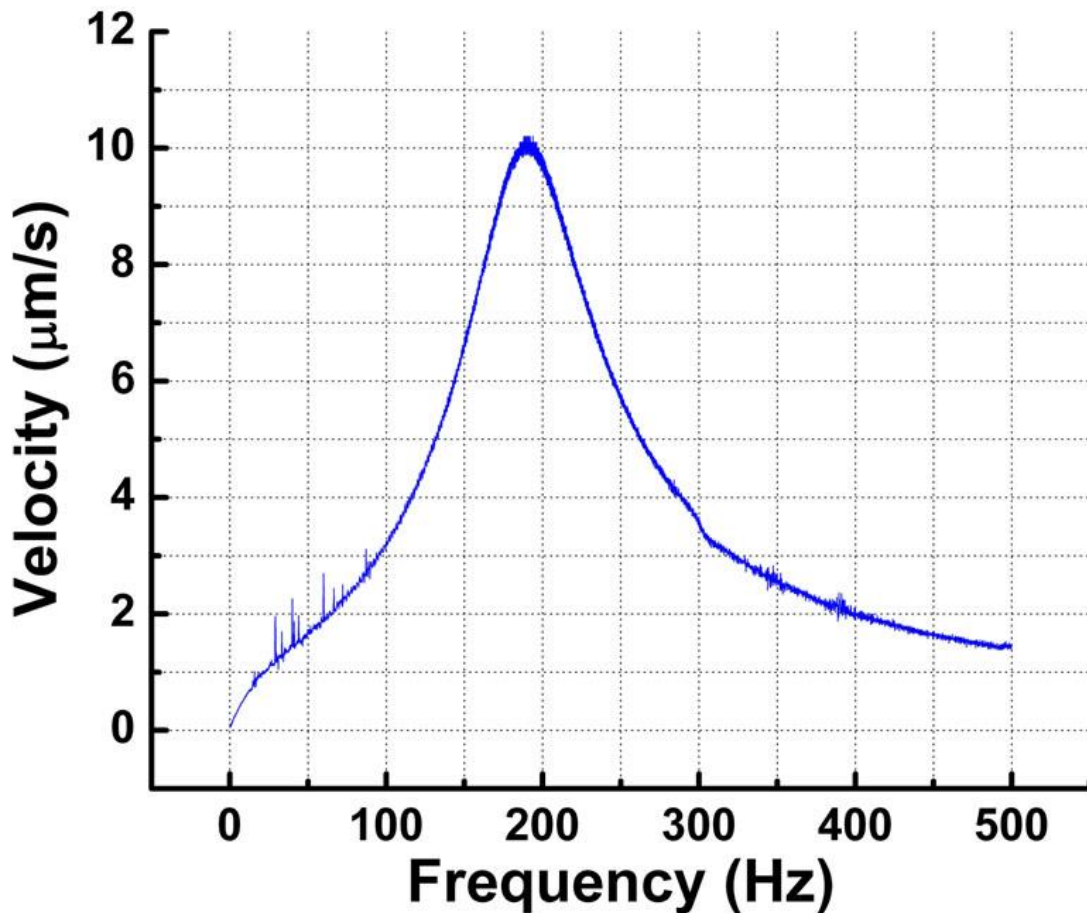


Figure 4-17. Frequency response of Type II piston-only mirror

#### 4.4 Chapter Summary

A new type of curved actuator has been designed and developed to actuate circular micromirrors with improved area efficiency, while at the same time achieving large scan range at low voltage. This CCBA actuator consists of three curved concentric Aluminum/Tungsten bimorphs for fast thermal response and high responsivity, and two rigid frames connected in between for scan range amplification. CCBA shows unique characterizations of the coupled bending and twisting motion, and also the in-plane movement because of the twisting. Both analytical and finite element models have been built to analyze these special characteristics of the CCBA. It has also been found that the symmetry of the mirror itself will reduce the twisting and the in-plane movement. The unique characteristics of CCBA may be useful for generating special scanning patterns by utilizing the bending, twisting and in-plane movement. 2D or even 3D scan patterns can be potentially generated by a single CCBA or its modifications.

Two types of the CCBA-based MEMS mirrors have been designed and fabricated. Large scan range at low driving voltage has been demonstrated. A tip-tilt-piston micromirror with a circular mirror plate based on this actuator design has been proposed and fabricated. The mirror is capable of scanning  $\pm 11^\circ$  at 0.6 V, and generating a 227  $\mu\text{m}$  piston displacement at only 0.8 V. The measured lateral shift and tilt angle of the mirror plate are less than 7  $\mu\text{m}$  and  $0.7^\circ$ , respectively, through the entire piston displacement. A piston-only micromirror has also been demonstrated, and it has even smaller lateral shift of less than 3  $\mu\text{m}$  and tilt of less than  $0.4^\circ$  through the piston scan range. This mirror generates large vertical displacement of about 200  $\mu\text{m}$  at 0.9 V.

## CHAPTER 5 MICROLENS SCANNERS AND CONFOCAL MICROSCOPY APPLICATIONS

As discussed in Chapter 1, adaptive and tunable optical components and systems have extensive applications and have been a hot research field for years. Focal tunable microlens is one kind of adaptive optical components for dynamic focusing of light when it goes out-of-focus. Liquid or polymer microlens uses deformable shapes to change the focal length in large range [151,160,161], but they have large driving voltages and/or large size and very slow response time. Also the aberrations and the changing numerical aperture make them not good choices for endoscopic imaging applications.

This chapter will start with presenting multiple designs of electrothermal microlens scanners and focal tunable microlens enabled by such scanners. Miniature electrothermal microlens scanners have been developed to actuate microlens with large tunable range from hundreds of microns to 1 mm under low driving voltage. The developed microlens scanners add a new and very promising depth scan mechanism for endoscopic imaging, including confocal endomicroscope, endoscopic OCT, and endoscopic NLOM.

Three generations of MEMS-based confocal imaging systems will be discussed in details. The 1st-generation MEMS-based 2D CSM uses a microlens scanner for the depth scan and a 1D stage for lateral scan. The 2nd-generation MEMS-based 3D CSM employs a microlens scanner and a 2D mirror for 3D raster scan. The 3<sup>rd</sup>- generation MEMS-based confocal endomicroscope is enabled by a confocal endoscopic probe that integrates MEMS microlens scanner, MEMS mirror, fiber and micro-optics to realize high-performance 3D confocal imaging *in vivo*.

## 5.1 Electrothermal Microlens Scanners

Several microlens-scanners based on LSF-LVD actuators have been designed and fabricated. The microlens-scanners are designed to hold different sizes and weights of microlens. As shown in Figure 5-1A, the LSF-LVD actuator is comprised of three Al/SiO<sub>2</sub> bimorphs with two rigid frames connected in between. The actuation mechanism is electrothermal actuation, with a thin layer of Pt embedded along the bimorphs as the heater. The large initial elevation due to residual stresses in the bimorph beams provides space for the platform to displace vertically in large range.

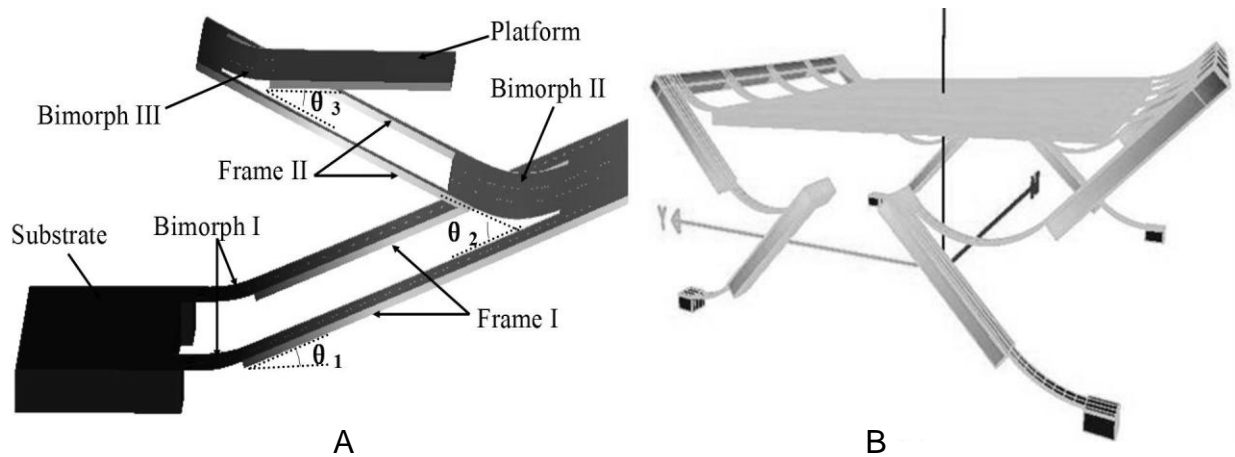
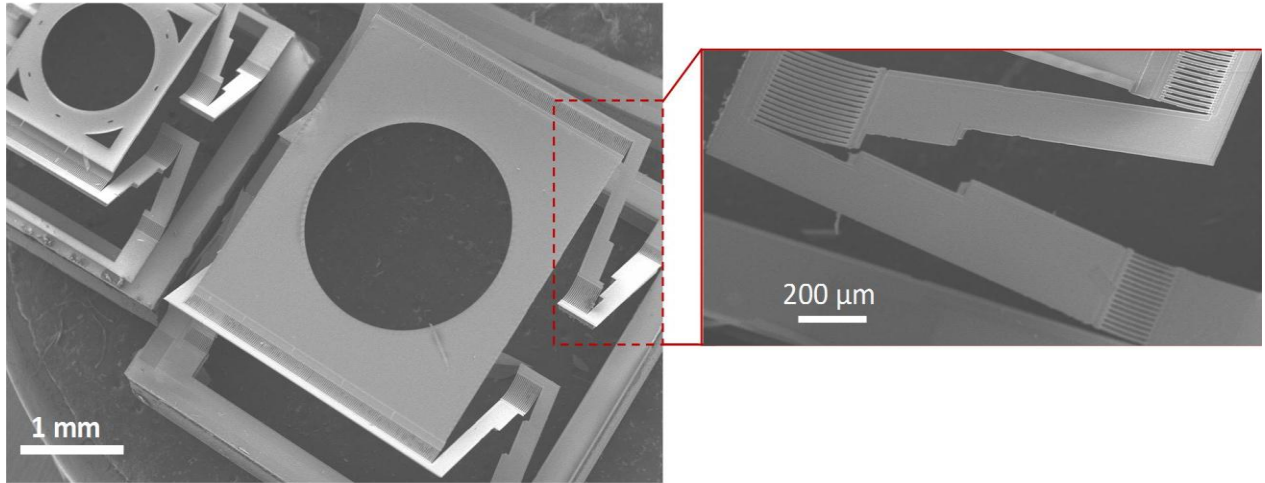
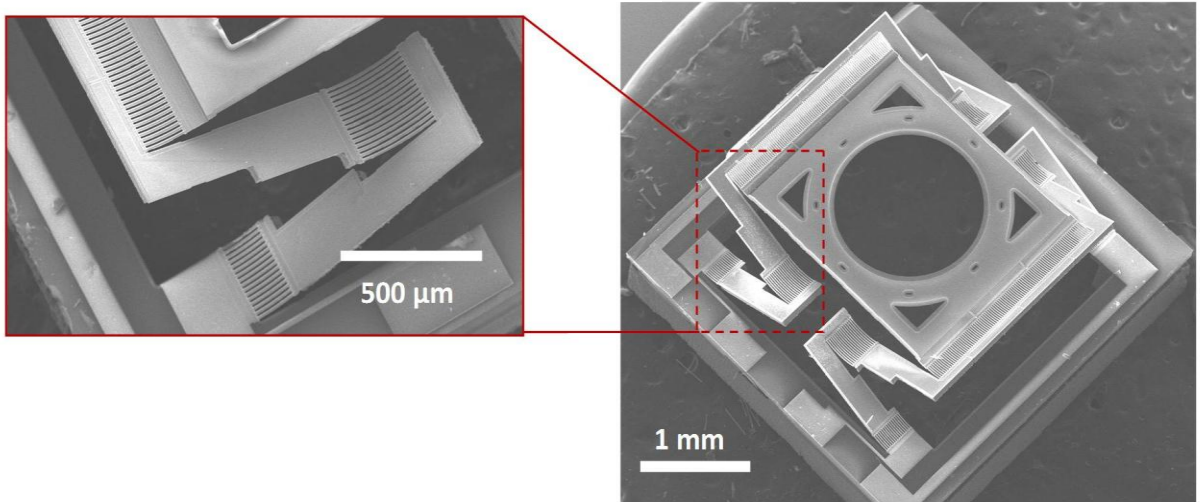


Figure 5-1. Schematic of LSF-LVD based microlens scanner. A) Schematic of LSF-LVD actuator design. B) Schematic of LSF-LVD based microlens scanner.

The microlens scanners use two sets of LSF-LVD actuators symmetrically located at two sides as shown in Figure 5-1B. The last bimorphs of both actuators are line-anchored to the edge of the platform to ensure a stable actuation. The platform used to hold the microlens has a central hole to allow light to pass through. The device is fabricated using a combined surface- and bulk-micromachining process shown in Figure 3-4. Multiple types of microlens scanners with various device footprints and opening sizes have been fabricated as shown in Figure 5-2.



A



B

Figure 5-2. SEM images of fabricated microlens scanners. A) Type I lens scanner. The chip size is 4.4 mm and the opening diameter is 2 mm. B) Type II lens scanner, the chip size is 3.3 mm and the opening diameter is 1.2 mm.

The design parameters of type I and type II microlens scanners are listed in Table 5-1.

Table 5-1. Design parameters of microlens scanners

Structural Parameters	Type I	Type II
Opening diameter	2 mm	0.8 mm or 1.2 mm
Device footprint	4.4 mm by 4.4 mm	3.3 mm by 3.3 mm
Length of bimorph	150 $\mu\text{m}$ , 300 $\mu\text{m}$ , 150 $\mu\text{m}$	150 $\mu\text{m}$ , 300 $\mu\text{m}$ , 150 $\mu\text{m}$
Length of frame	1300 $\mu\text{m}$	900 $\mu\text{m}$
Width of bimorph	10 $\mu\text{m}$	10 $\mu\text{m}$
Width of Pt heater	6 $\mu\text{m}$	6 $\mu\text{m}$
Thickness of Silicon dioxide	1.1 $\mu\text{m}$	1.1 $\mu\text{m}$
Thickness of Al	1 $\mu\text{m}$	1 $\mu\text{m}$
Thickness of Pt heater	0.2 $\mu\text{m}$	0.2 $\mu\text{m}$

The assembling of the microlens scanner involves integrating a microlens to the microlens scanner holder. First, optical UV glue is dropped on the platform. Then, the microlens is put onto the platform and the aperture of the microlens is aligned to the central opening in the platform. After that, UV lamp is used to illuminate and cure the UV glue. Various commercial microlenses have been integrated with the microlens scanners as shown in Figure 5-3. The microlens selection is flexible depending on the requirements of specific applications. Glass lens is preferred due to the temperature stability and also the wide choices from commercial suppliers. Figure 5-3A shows an assembled spheric glass lens with a diameter of 1 mm, a thickness of 0.8 mm, and a focal length of 1 mm and Figure 5-3B shows an assemble aspheric glass lens with a diameter of 2.4mm, a thickness of 1 mm, and a focal length of 0.88 mm. Detailed testing results of the microlens scanners will be shown in Section 5.2.

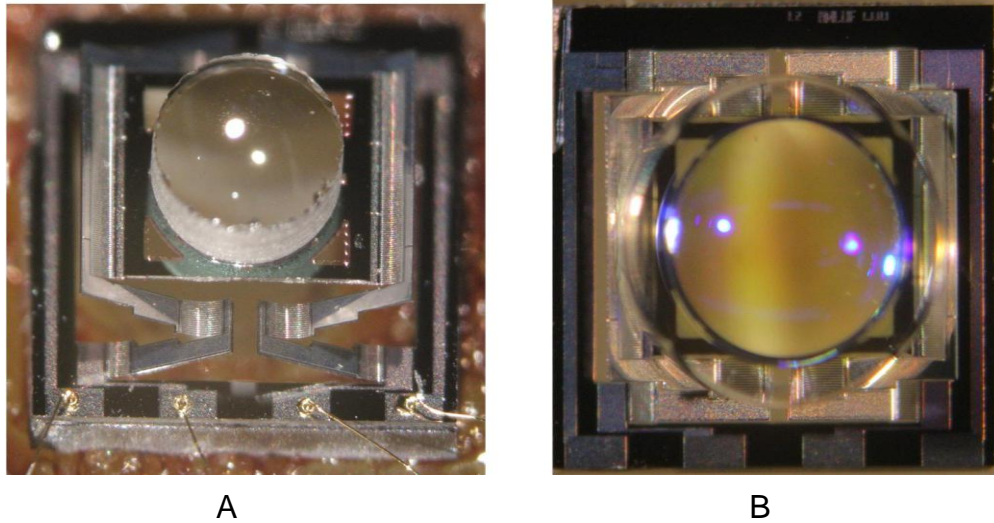


Figure 5-3. Photos of assembled tunable microlenses. A) An assembled spherical microlens with 1 mm-diameter. B) An assembled aspheric lens with 2.4-mm diameter.

Upon adding driving voltage/current, the Joule heating generated by the current will increase the temperature, and the actuators will bend downward, together with the platform and the microlens integrated with the platform. Figure 5-4A ~ Figure 5-4C show the piston motion of an assembled microlens scanner under different DC voltages.

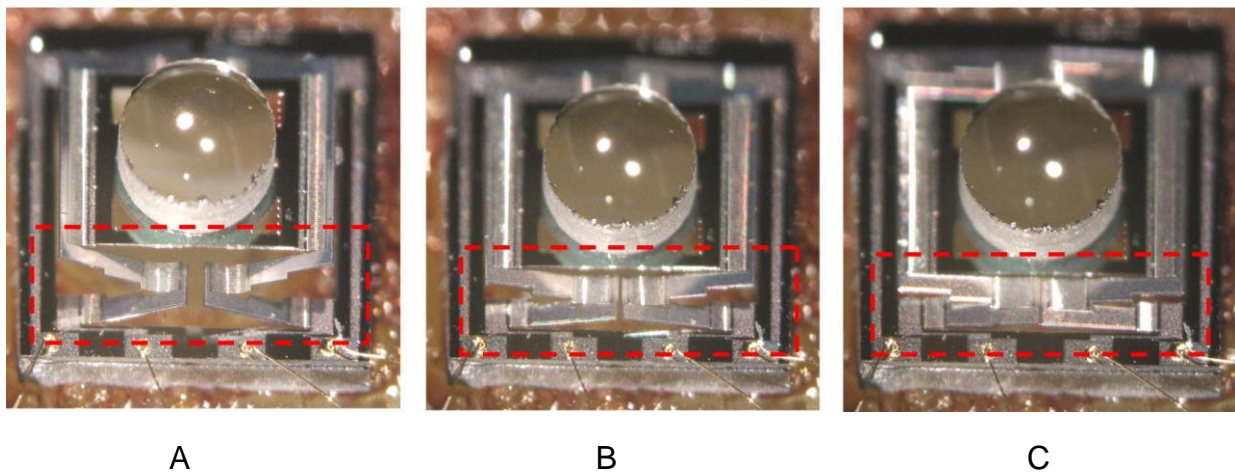


Figure 5-4. Photos of a tunable microlens driven at different voltages. A) Microlens scanner driven at 0 V. B) Microlens scanner driven at 0.8 V. C) Microlens scanner driven at 1.6 V.

## 5.2 MEMS-Based 2D Confocal Scanning Microscope

### 5.2.1 2D CSM System

A 2D CSM system using an electrothermal MEMS microlens scanner for large-tunable-range axial scan has been demonstrated. The schematic diagram of the CSM using a MEMS microlens scanner is shown in Figure 5-5.

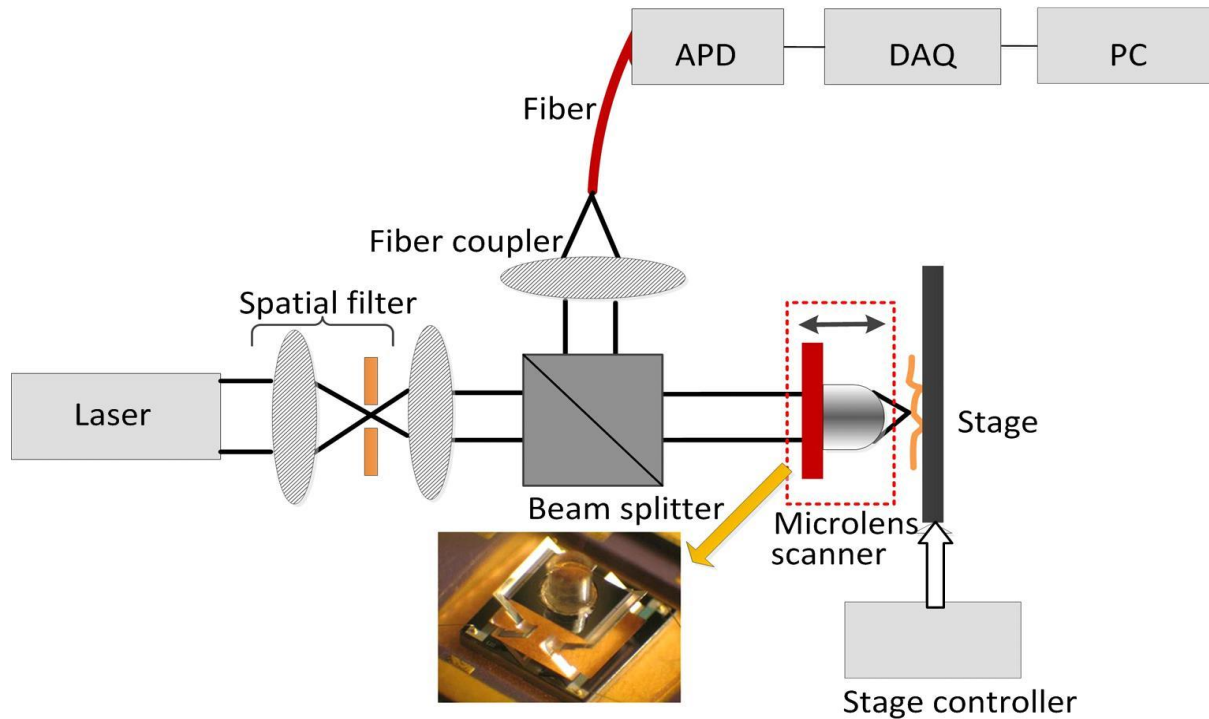


Figure 5-5. Schematic design of the 2D CSM

Laser beam from an argon-ion laser with a center wavelength of 514.5 nm is first cleaned up by a spatial filter and then collimated by a lens to 1 mm beam in diameter. The collimated light is then split into two paths by a 50/50 beam splitter. Half of the light is directed into the sample arm, and focused by the micro-objective integrate with a MEMS microlens scanner into the sample. At the same time, the microlens scans the focal point axially, thereby imaging at different depths of the sample. The lateral scan is accomplished by laterally translating the sample by a motor-controlled stage with sub-

micron resolution. The back-reflected/back-scattered light from the sample is then collected by the microlens, deflected by the beam splitter, then coupled into a fiber by a fiber collimator. The fiber core acts as a pinhole to eliminate the light returned from outside the confocal volume. The single-mode fiber has a mode-field diameter of 3.3  $\mu\text{m}$  and N.A. of 0.13. Light transmitted by the single mode fiber is detected by a high-sensitivity avalanche photodiode (APD) with an integrated amplifier (Hamamatsu, C5460-01). The amplified signal is acquired into a PC using Labview through a MCC data acquisition card.

### **5.2.2 MEMS Microlens Scanner for Automatic Depth Scan**

The required large depth scan for the confocal microscopy is obtained by axially actuating a lens by a LSF-LVD MEMS actuator to demonstrate the axial scan capacity of the LSF-LVD MEMS lens-scanner. The SEM images of a microlens scanner only and an assembled microlens scanner with a spherical glass lens are shown in Figure 5-6. The microlens has a diameter of 1 mm and a thickness of 1 mm. The working distance is 3 mm in this lens with a NA of 0.17.

A 0.9 mm vertical actuation range of the glass lens has been obtained at only 6.3 V dc as shown in Figure 5-7. The frequency response of the device is shown in Figure 5-8 and a mechanical resonance of 79 Hz is observed. There are small tilting and lateral shift during axial actuation, mainly due to some small differences among the bimorph actuators caused by fabrication variations. The tilting and lateral shift could be minimized to below  $0.4^\circ$  and 10  $\mu\text{m}$ , respectively, by controlling the driving voltages ratios of the two actuators.

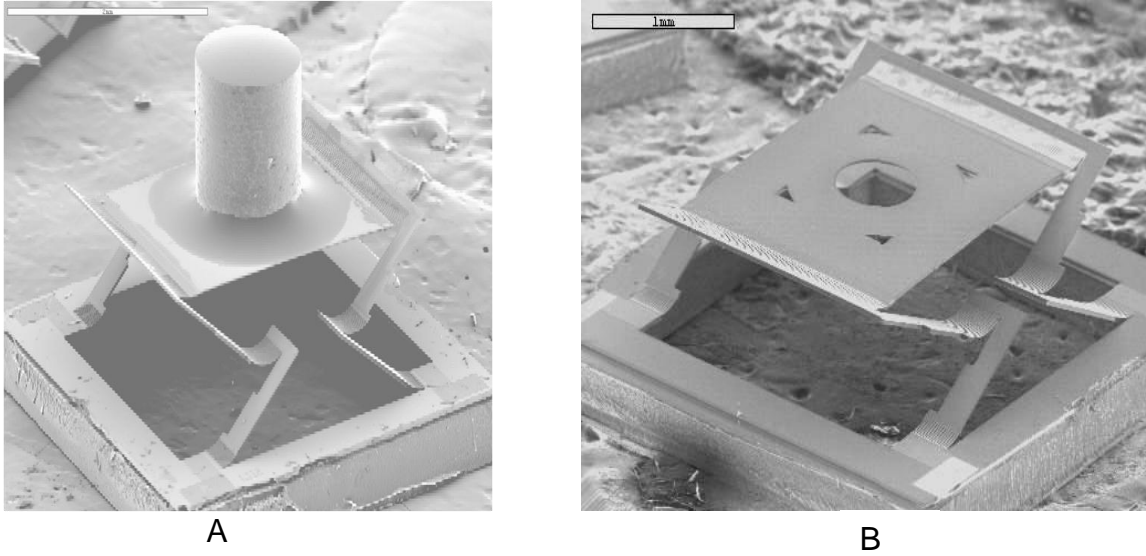


Figure 5-6. SEM images of loaded and unloaded microlens scanner used in the 2D CSM. A) SEM of an assembled microlens scanner. B) SEM of an unloaded microlens scanner.

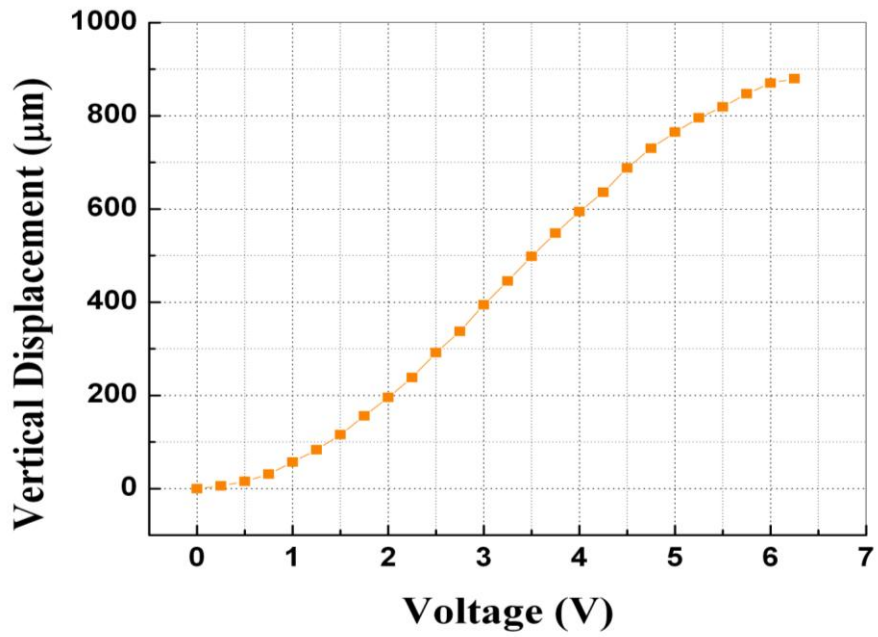


Figure 5-7. Static measurement of the microlens scanner used in the 2D CSM: vertical displacement vs. voltage

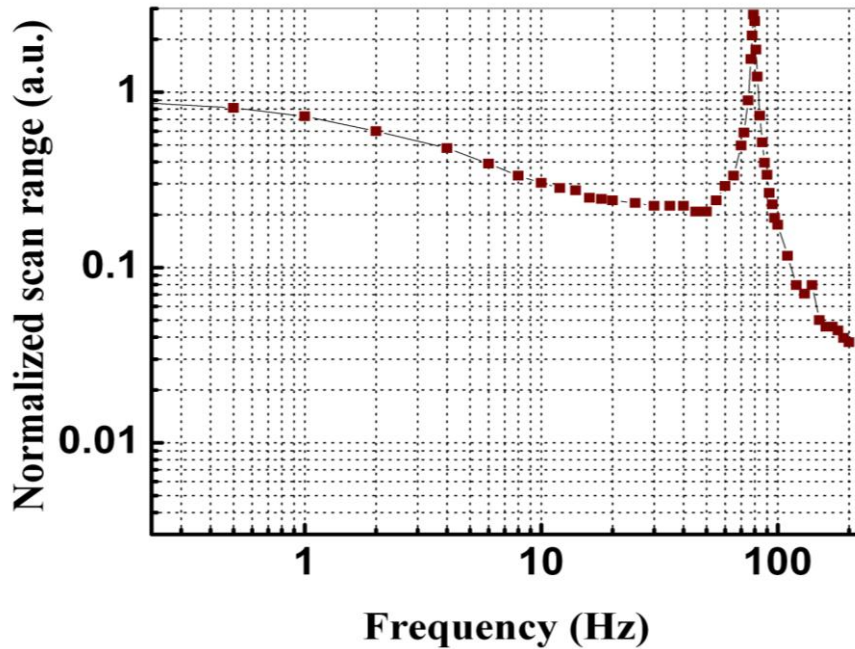


Figure 5-8. Frequency response of the microlens scanner used in the 2D CSM

### 5.2.3 System Characterization

System characterizations including the axial resolution and lateral resolution have been measured for this confocal microscope. The axial resolution is measured by using a mirror as the sample and moving the mirror's surface through the microlens' focal plane. The detected signals at various mirror positions are plotted in Figure 5-9A, which indicate that the FWHM of the axial resolution is 38.0  $\mu\text{m}$ . The lateral resolution is obtained by placing a sample with strip patterns at the focal plane and moving the sample laterally. Figure 5-9B shows the detected signals when a sharp edge on a USAF resolution test target passes the focal point of the microlens. Using the 10%-90% edge width, the measured lateral resolution is about 1.25  $\mu\text{m}$ .

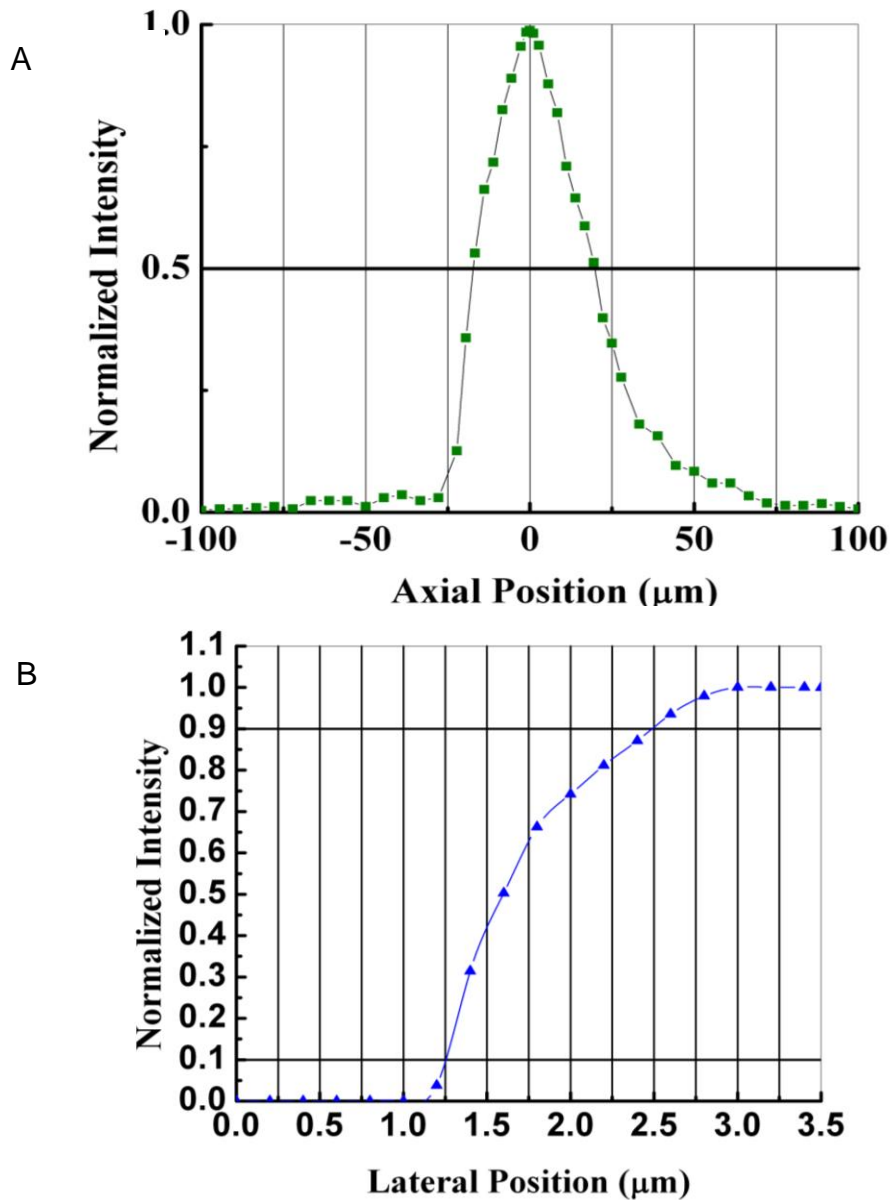


Figure 5-9. Resolution measurement results of the 2D CSM. A) Axial resolution measurement. FWHM=38  $\mu\text{m}$ . B) Lateral resolution measurement. 10%-90% rise distance is about 1.25  $\mu\text{m}$ .

#### 5.2.4 Imaging Experiments and Results

Confocal imaging experiments have been performed on various samples including alloy micro-particles embedded in polymer and rat skin. A 2D cross-sectional image of the micro-particles in polymer is shown in Figure 5-10. The image size is 200  $\mu\text{m}$  by 200  $\mu\text{m}$ . The diameters of the micro-particles are around 25  $\mu\text{m}$ . It is obvious

that the axial resolution is higher than the lateral resolution. A 2D image of a piece of rat skin is shown in Figure 5-11.

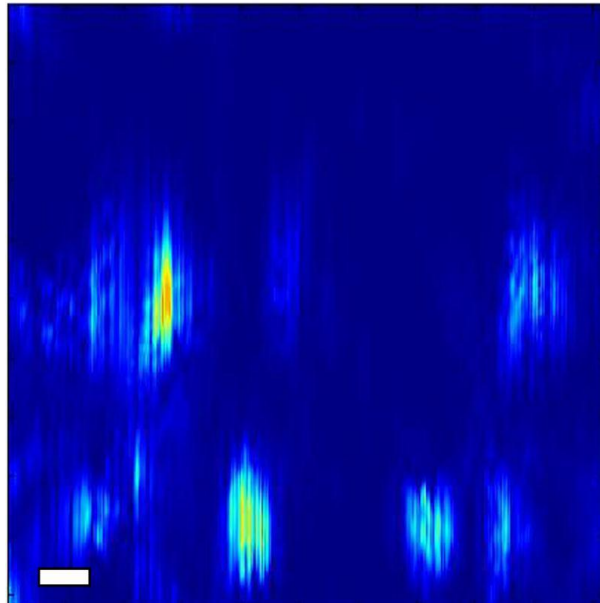


Figure 5-10. 2D confocal reflectance image of micro-particles embedded in polymer taken by the 2D CSM. 200- $\mu\text{m}$  depth scan by microlens scanner with a driving voltage of 3 Vp-p at 2Hz. 200- $\mu\text{m}$  lateral scan by stage. Scale bar is 20  $\mu\text{m}$ .

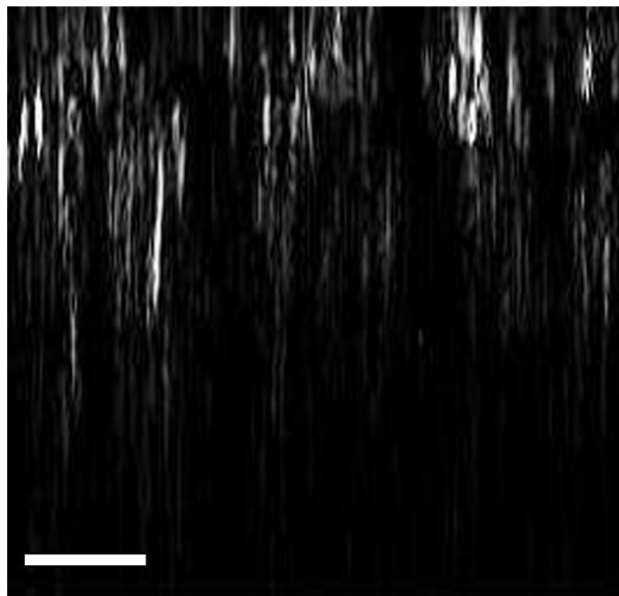


Figure 5-11. 2D confocal reflectance image of rat skin taken by the 2D CSM. 250- $\mu\text{m}$  depth scan by microlens scanner with a driving voltage of 3.5 Vp-p at 2Hz. Scale bar is 50  $\mu\text{m}$ . The image size is 250  $\mu\text{m}$   $\times$  250  $\mu\text{m}$ .

## 5.3 MEMS-Based 3D Confocal Scanning Microscope

### 5.3.1 3D CSM System

In this section, a 3D CSM using a full-MEMS scanning system to perform both depth and lateral scan will be present. The full-MEMS 3D scanning system includes a MEMS lens scanner that can axially scan for a large displacement at a small voltage and a MEMS 2D mirror that can scan large angles at both lateral directions at low voltage. This scanning system, which can realize 3D scan at low voltage with a small footprint, is especially appealing for confocal endoscopic imaging.

The schematic diagram of the 3D CSM system is shown in Figure 5-12. The system incorporates a laser diode with an output of a collimating beam at 638 nm, a spatial filter to clean up the laser diode output beam and focus the beam to a pinhole to form a point source, a collimating lens to collimate the light to a beam diameter of about 1 mm, a beam splitter to separate the light path, a MEMS 2D scanning mirror, a MEMS lens scanner, a focusing lens followed by a pinhole, an avalanche photodiode (APD) and a data acquisition card. The collimated laser beam ( $\lambda=638\text{nm}$ ) emitted from a laser diode (Blue Sky Research) passes through a spatial filter to form a point source. Then the light is collimated to a 1 mm-diameter beam. After passing through a beam splitter, the light beam is scanned laterally in x- and y- directions by the 2D MEMS mirror that is initially tilt by  $45^\circ$ . After that, the MEMS lens scanner with an integrated aspheric objective lens (Thorlabs) focuses the beam into the sample, and at the same time axially scans the objective lens in z-direction. The back-reflected light from the sample is then collected by the objective lens on the lens scanner and deflected consequently by the MEMS mirror and the beam splitter. Finally the light beam is focused to the

pinhole by another lens and picked up by the APD (Hamamatsu). The APD output signal is acquired into a PC via a data acquisition card (DAQ).

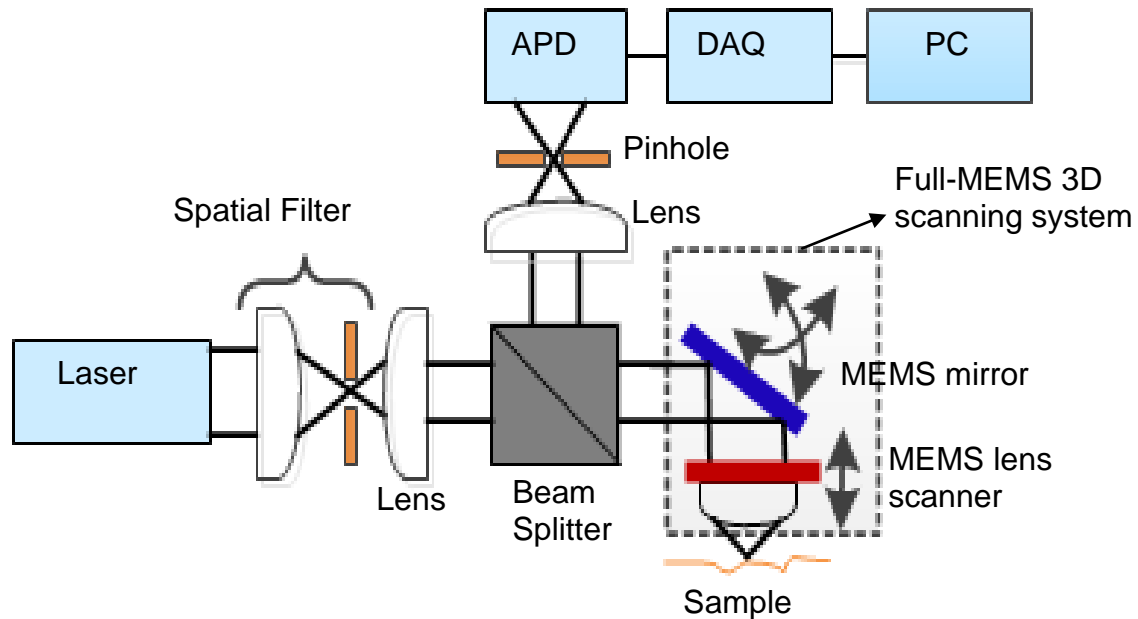


Figure 5-12. Schematic design of the 3D CSM

### 5.3.2 MEMS Scanning Devices

The full-MEMS 3D scanning system (shown in Figure 5-12) includes two MEMS devices: an MEMS mirror for the lateral scan and an MEMS lens for the axial scan. The MEMS lens scanner has two components: MEMS scanning platform (Figure 5-13A) and a miniature aspheric objective lens assembled onto the MEMS scanning platform (Figure 5-13B). The platform has an etched opening in the center for the light to pass through. The platform is symmetrically supported by four LSF-LVD actuators at the two sides. The device is fabricated on a SOI substrate with a 40  $\mu\text{m}$ -thick device layer. The platform is elevated upward at about 800  $\mu\text{m}$  after the device release due to the residual

stresses in the actuator beams. A commercial miniature glass lens was selected as the objective lens for this system. The lens is an aspheric lens (Thorlabs) with a diameter of 2.4 mm, a NA of 0.55 and a back focal length of 0.88 mm. The lens has diffraction-limit performance at  $\lambda=638$  nm. The lens is glued by UV glue to the platform with the clear aperture of the lens aligned to the central opening on the platform.

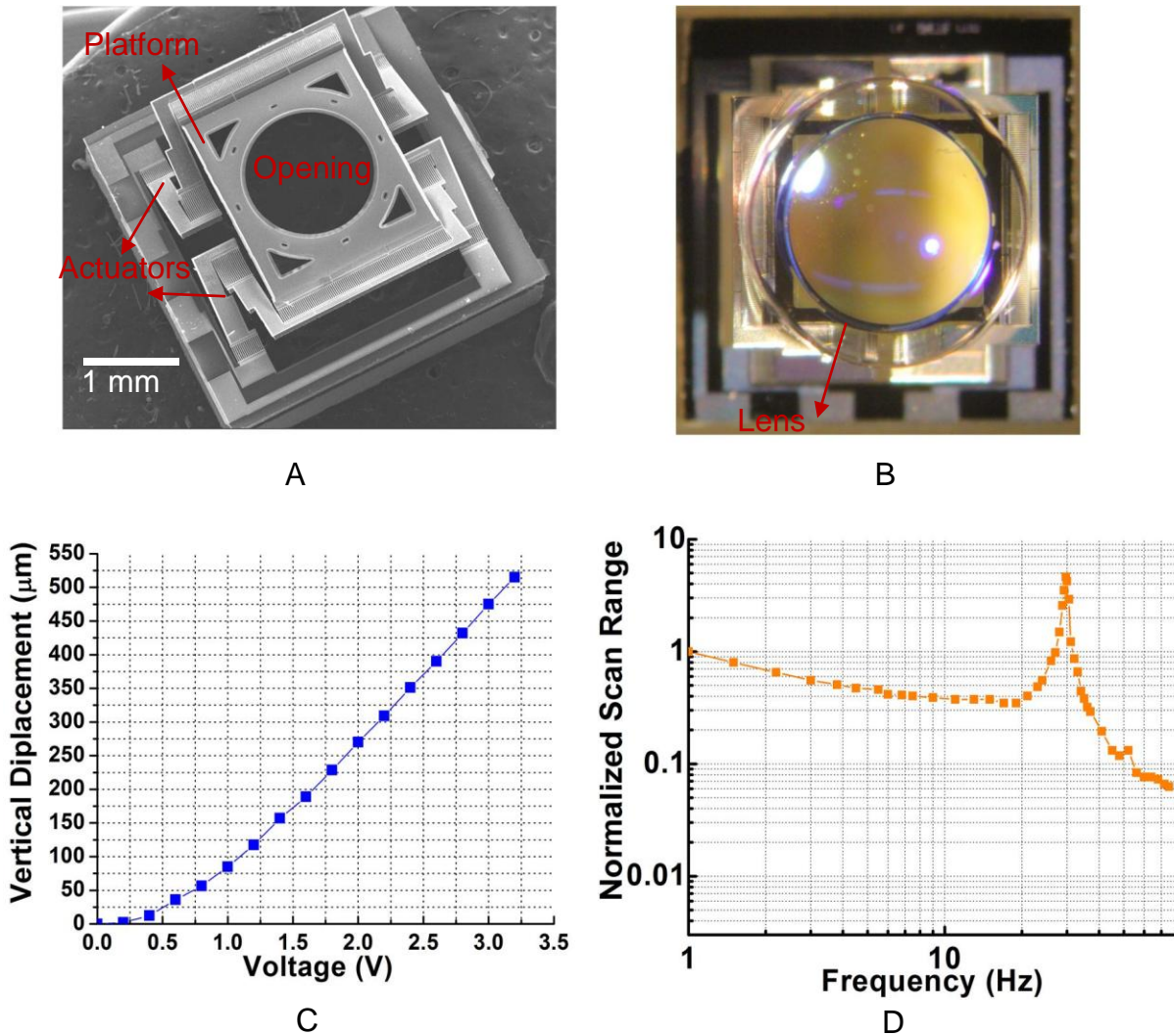


Figure 5-13. Photos and characterizations of the tunable microlens used in the 3D CSM. A) SEM of a lens scanning platform. B) Microscopic picture of an assembled lens scanner. C) Z displacement vs. voltage of the assembled lens holder. D) Frequency response of the assembled lens scanner.

The vertical elevation of the platform after the lens being assembled is  $550\ \mu\text{m}$ . The device footprint of the lens scanner is  $3.3\ \text{mm} \times 3.3\ \text{mm}$ . The fabrication process is the same as that described in Figure 3-4.

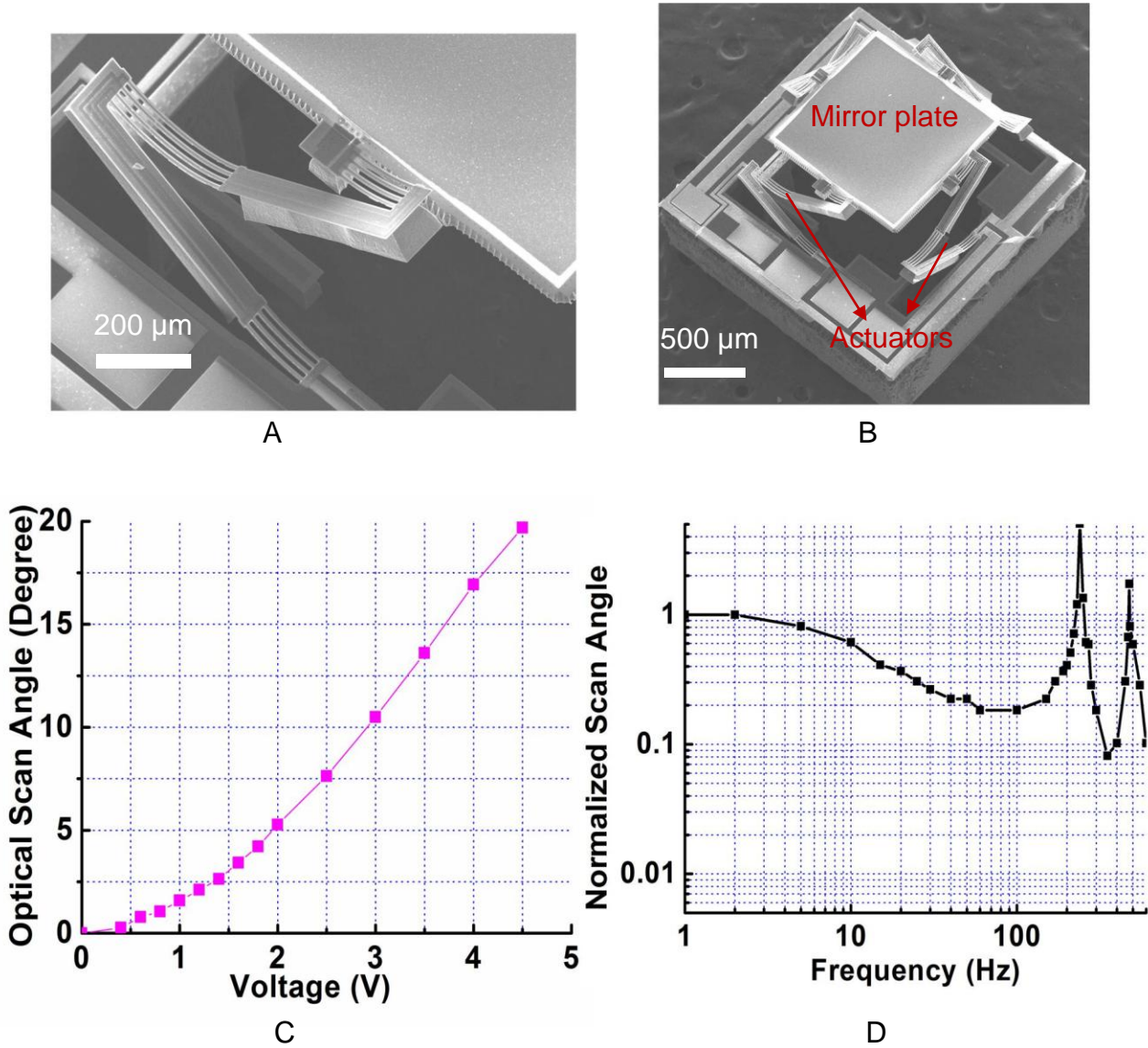


Figure 5-14. Photos and characterizations of the 2D micromirror used in the 3D CSM. A) SEM of a LSF-LVD actuator. B) SEM of a MEMS mirror. C) Optical scan angle vs. driving voltage of the MEMS mirror. D) Frequency response of the MEMS mirror.

The characteristics of the lens scanner are shown in Figure 5-13C and Figure 5-13D. A vertical actuation range of 515  $\mu\text{m}$  was obtained at only 3.2 V. The frequency response of the assembled lens scanner is shown in Figure 5-13D with the first resonance peak at about 30 Hz. The speed of the MEMS lens scanner is adequate for the z-scan which is the slowest axis scanning. Also the z-scan range is sufficiently large for the depth scan of confocal imaging.

The MEMS mirror is a two-dimensional scanning mirror with a square mirror plate. The 1mm $\times$ 1mm mirror plate is supported by four identical and symmetrically arranged LSF-LVD actuators. Figure 5-14A and Figure 5-14B show an SEM picture of one LSF-LVD actuator and an SEM picture of the MEMS mirror, respectively. The device footprint of the MEMS mirror is 2 mm  $\times$  2 mm. The mirror scans optical angles of  $\pm 20^\circ$  at the driving voltage of 4.5 V as shown in Figure 5-14C. The frequency response of the MEMS mirror is shown in Figure 5-14D. The first peak is at 240 Hz while the second peak is at 475 Hz.

### **5.3.3 System Characterization**

Both the lateral and axial resolutions have been characterized. Figure 5-15A and Figure 5-15B show the measurement results of the axial resolution and the lateral resolution, respectively. The axial resolution is measured by translating a mirror surface in z-direction and recording the change of the optical power detected by the APD detector. The FWHM axial resolution is found to be 9.0  $\mu\text{m}$ . The lateral resolution is measured by laterally translating a reflective edge on the focal plane and the 10%--90% edge width is measured as 1.2  $\mu\text{m}$ . Figure 5-16 is an en face scan image of the elements in Group 7 of a USAF resolution target obtained by the system.

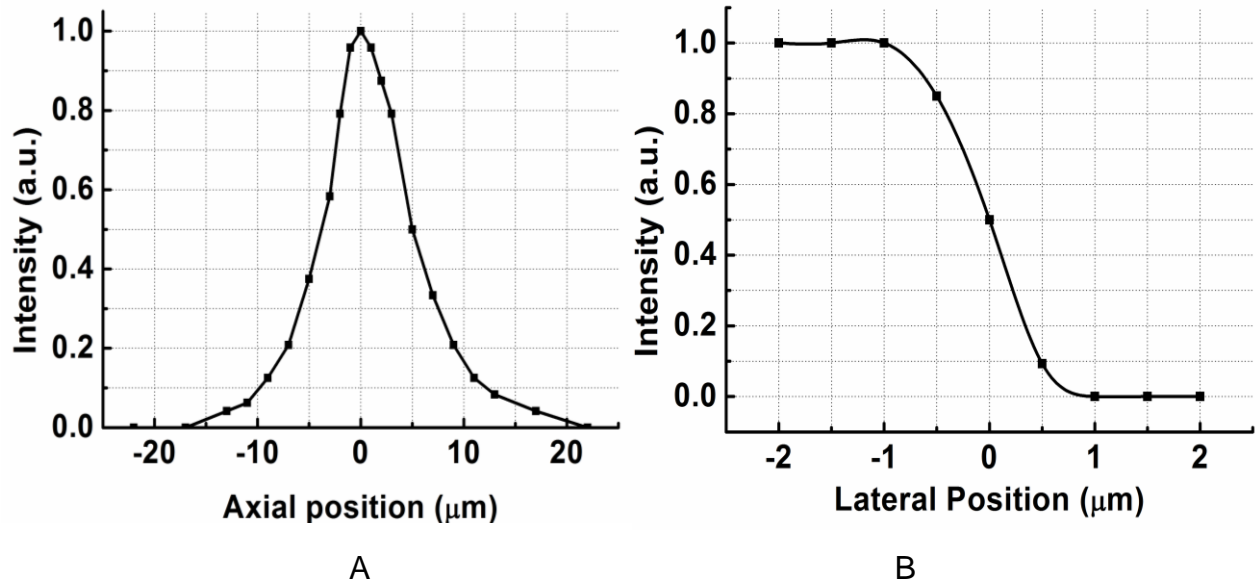


Figure 5-15. Characterizations of the 3D CSM system. A) Axial resolution measurement. B) Lateral resolution measurement.

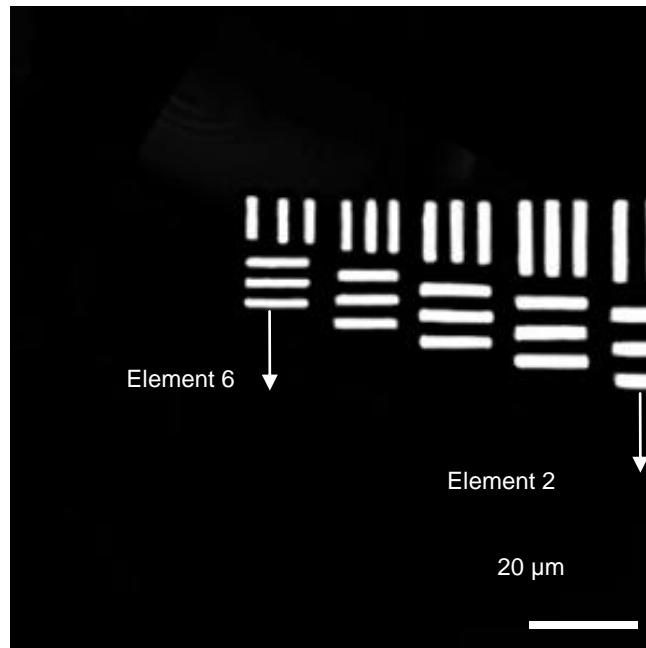


Figure 5-16. Reflectance image of group 7 elements in a USAF resolution target by the 3D CSM. The field-of-view is about  $120 \mu\text{m} \times 120 \mu\text{m}$ . The smallest elements are 2.2  $\mu\text{m}$  wide.

### 5.3.4 Imaging Experiments and Results

Confocal imaging experiments have been performed using this MEMS-based CSM system. 2D and 3D reflectance images have been taken on a PDMS sample with micro-particles embedded inside. The micro-particles are alloy particles with the sizes ranging from around 1  $\mu\text{m}$  to tens of microns. The particles are randomly distributed inside the transparent PDMS.

The four actuators of the MEMS mirror are grouped into two pairs with each pair including two actuators at the opposite sides of the mirror plate. The actuator pair controlling the x-scan is differentially driven with a ramp waveform of 0 ~ 4.2 V at 500 Hz. The scan in x- direction is driven near the second resonance peak for large scan angle and for high scan speed. The actuator pair for the y-direction scan is differentially driven with a ramp waveform of 0 ~ 3.5 V at 1 Hz. Meanwhile, the z- direction scan is performed by simultaneously driving all the actuators of the MEMS lens scanner with a ramp waveform of 0 ~ 2 V at 2 mHz.

Figure 5-17A shows the photograph of the PDMS sample and Figure 5-17B ~ Figure 5-17E show the 2D reflectance confocal images acquired with the CSM at different depths of the sample. The driving voltages of the MEMS lens scanner from Figure 5-17B to Figure 5-17E are 0.5 V, 0.6 V, 0.7 V and 0.8 V, respectively.

Figure 5-18 is a stack of the slices of images shown in Figure 5-17. As shown in Figure 5-18, different particles appeared and disappeared at different imaging depths. Particles are labeled to give a clear view. The optical sectioning capacity is demonstrated. Only the signals from the focal plane contribute to the image at that depth while the background signals from outside the focal plane are excluded.

Figure 5-19 is the 3D image of the sample reconstructed by stacking the 2D image slices by Amira 3D imaging software. The imaging volume is  $120\ \mu\text{m} \times 120\ \mu\text{m} \times 270\ \mu\text{m}$ .

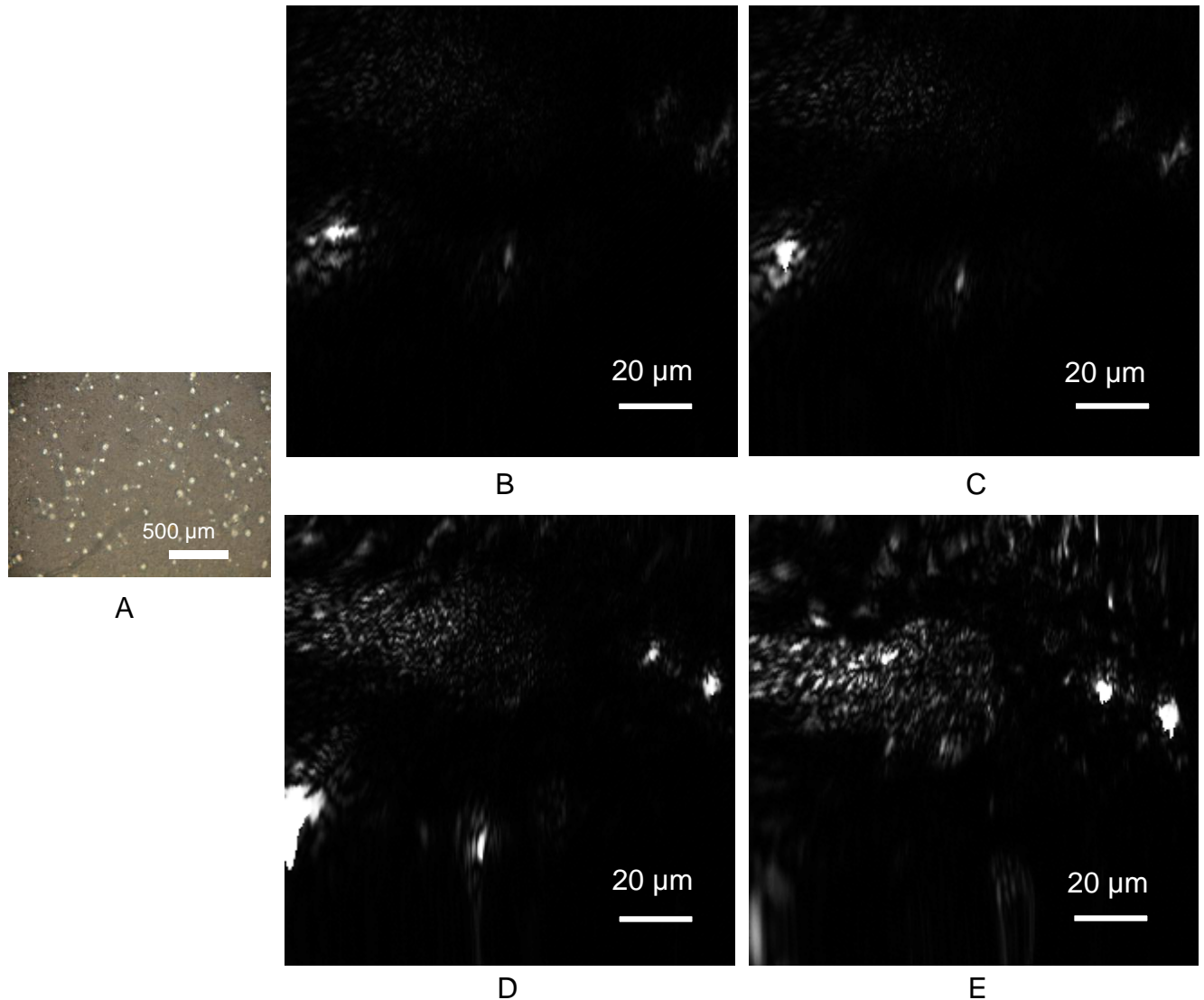


Figure 5-17. 2D confocal reflectance images of micro-particles embedded in PDMS taken by the 3D CSM. A) Photographs of the PDMS sample. B)-E): 2D confocal reflectance images of the sample at different depths. The driving voltages of the MEMS lens scanners are at: B) 0.5 V; C) 0.6 V; D) 0.7 V; E) 0.8 V. The image sizes are  $120\ \mu\text{m} \times 120\ \mu\text{m}$ .

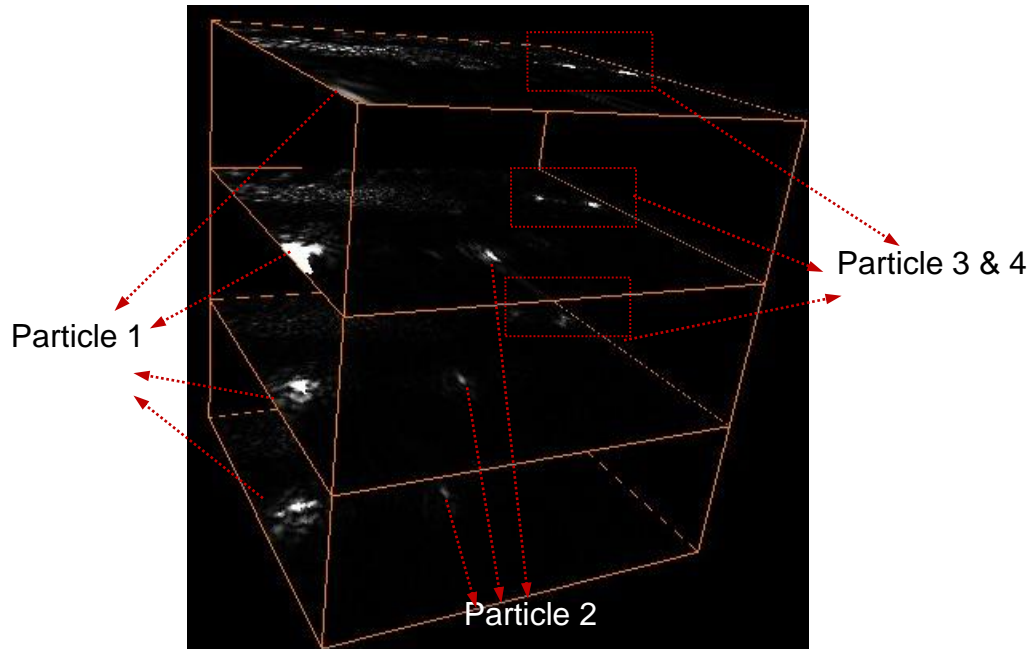


Figure 5-18. A stack of Figure 4-17B~ Figure 4-17E with some particles labeled. Various particles show up and disappear at different depths.

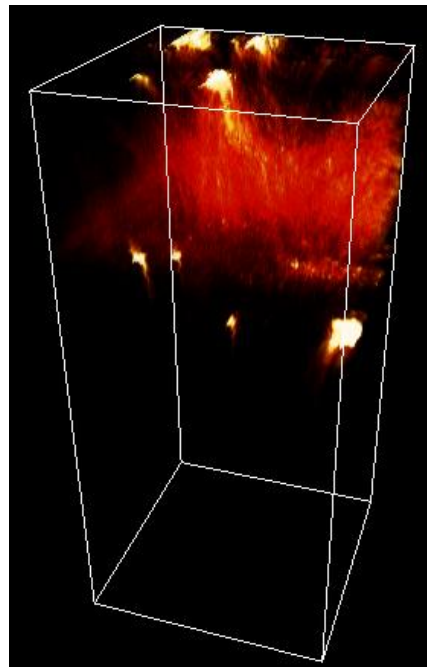


Figure 5-19. 3D volume-rendered image of micro-particles embedded in PDMS obtained by the 3D CSM

Confocal reflectance imaging has also been performed on an acute rat brain tissue by this system. The brain tissue is cut with a thin slice of 200  $\mu\text{m}$ . Figure 5-20

shows the 2D image and 3D image of the sample, respectively. The 3D image is volume rendered by stacking the 2D image slices by Amira 3D imaging software. The imaging volume is  $120\ \mu\text{m} \times 120\ \mu\text{m} \times 500\ \mu\text{m}$ .

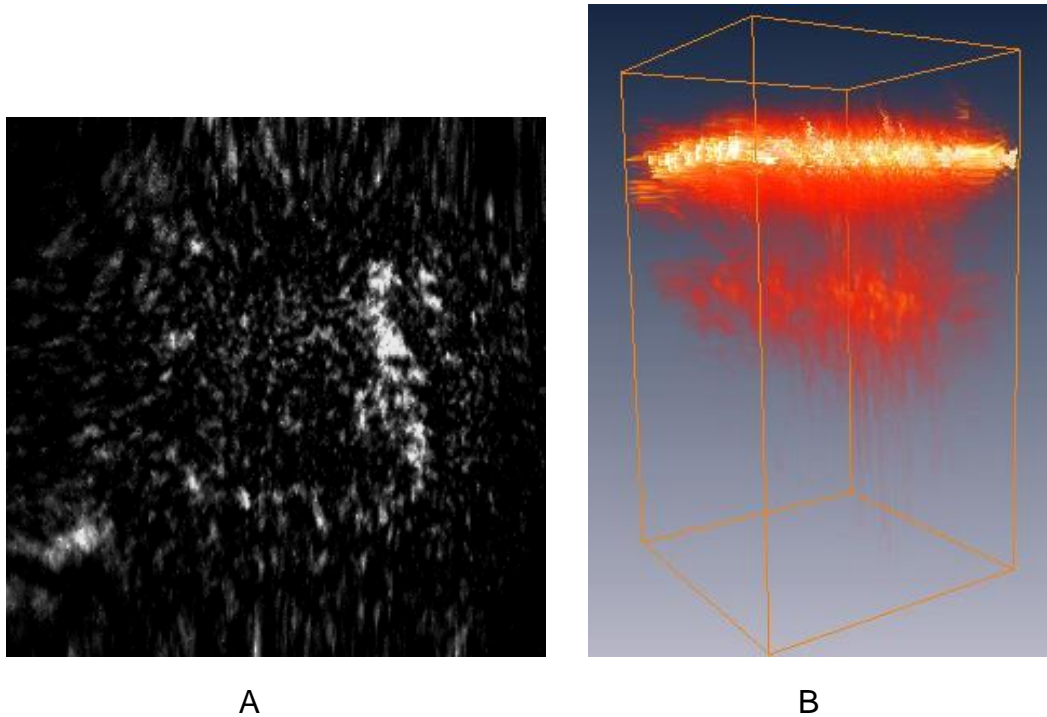


Figure 5-20. 2D and 3D confocal reflectance image of rat brain tissue by the 3D CSM. A) A 2D confocal reflectance image of the rat brain tissue. B) A 3D volume-rendered image of the rat brain tissue.

#### 5.4 MEMS-Based 3D Confocal Scanning Endomicroscope

Confocal endomicroscope is an emerging imaging technology valuable for *in-vivo* imaging of gastrointestinal mucosa, liver, and pancreatic duct, etc [186]. It is an extension of the well-established confocal microscopy to endoscopic applications for *in-vivo* cancer diagnosis. The challenges for 3D confocal endomicroscope include miniaturization of optical scan engines especially for both lateral and axial scans, requirement of large scan range under low drive voltage, and miniaturization of the optics without largely sacrificing optical performance.

MEMS-based miniature scanners are promising to enable confocal endomicroscopy. Several confocal microscopes employing MEMS scanners have been reported, but a confocal endoscopic system with effective 3D scanning inside the probe hasn't been reported yet. Maitland *et al.* and Shin *et al.* reported confocal microscopes using 2D MEMS mirrors for the lateral scan [71, 72], but the depth scan was absent. The 3D confocal systems reported in [74-76] relied on external motors and sliding stages for the axial scan which suffer from the instability with friction and the tradeoffs between size, speed and cost. The 3D dual-axis confocal microscope developed by Jeong *et al.* used a pair of electrostatic MEMS mirrors for the lateral scan and the depth scan [73], but it had small static axial displacement (10  $\mu\text{m}$ ) at high voltage (200 V) and the displacement was still limited ( $\pm 27.5 \mu\text{m}$ ) even at resonance.

This study develops a 3D confocal scanning endomicroscope with full-MEMS 3D scan engines to realize large scan ranges under low voltages, compact fiber-optic probe to access internal organs, and high-quality micro-optics to realize high-performance confocal imaging.

#### **5.4.1 3D Confocal Endomicroscope System**

The schematic design and the photograph of the confocal endomicroscope are shown in Figure 5-21A and Figure 5-21B, respectively. Polarization is controlled to suppress unwanted back-reflections. The laser beam at 638 nm from the laser diode (Blue Sky Research) first propagates through a spatial filter (Newport), which uses a pinhole to filter out the high spatial frequencies, clean up the laser output beam and produce a clean Gaussian beam to launch into the system. A lens after the spatial filter collimates the beam to 1 mm in diameter. A polarizing beam splitter (PBS) then reflects

the s-polarized light at  $90^\circ$  while transmitting the p-polarized light. The reflected s-polarized light is coupled into a single-mode polarization maintaining (PM) fiber (Thorlabs) by a fiber coupler (Thorlabs). The PM fiber maintains the light polarization direction along the fiber cord and then delivers the linearly-polarized light into an endoscopic probe (Figure 5-22A).

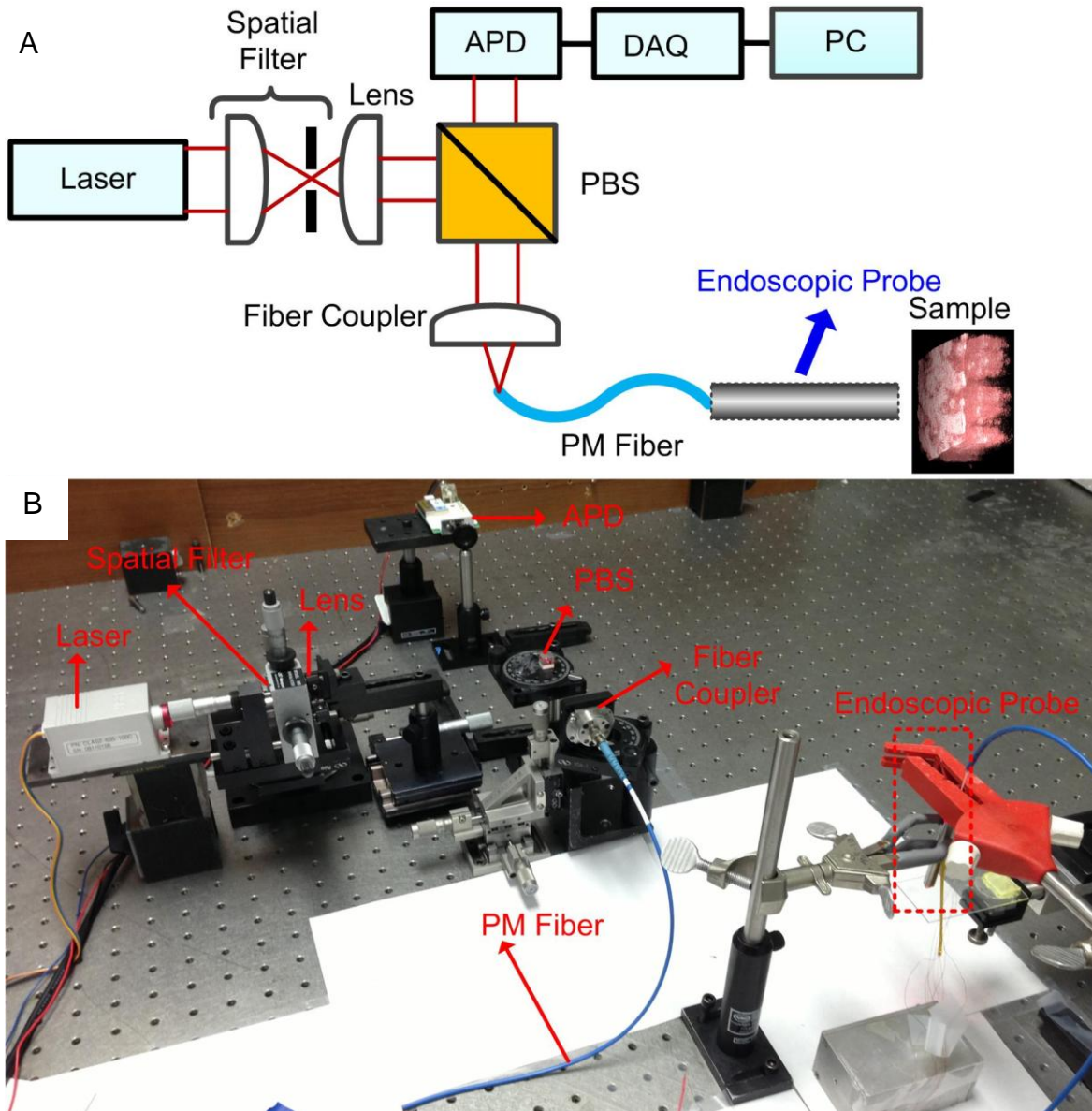


Figure 5-21. System design of the 3D confocal scanning endomicroscope. A) Schematic of the system design. B) Photograph of the complete system.

The endoscopic probe as shown in Figure 5-22A comprises a GRIN lens, a quarter wave plate (QWP), a MEMS 2D scan mirror, a fixed mirror, a pair of achromatic lenses and a MEMS tunable objective lens. The GRIN lens with quarter-pitch is to collimate the diverging light exiting the fiber core. The diameter of the GRIN lens is 2 mm and the length is 5.17 mm. The linearly-polarized beam after GRIN lens is incident on the QWP at  $45^\circ$  to the optic axis of the QWP. The linearly s-polarized light is divided into two equal orthogonal electric field components with one component retarded by a quarter of the wavelength by the QWP, therefore producing a circularly-polarized light output. Then A MEMS 2D scan mirror perform the two-dimensional lateral scan of the collimated light beam, followed by a fixed mirror tilted at  $45^\circ$  to fold the light path by  $90^\circ$ . A pair of achromatic lenses (Edmund Optics) is then employed for beam expansion as well as aberration correction. After that, a 1D MEMS tunable objective lens is used to focus the beam and also perform the depth scan.

The backreflected/backscattered light from the sample propagates back through the probe passing the MEMS tunable objective lens, the beam expander lens pair, the fixed mirror and the MEMS 2D mirror. Then the light passes the QWP for the second time with another quarter wavelength retardation introduced by the QWP, which changes the circularly-polarized light to linearly p-polarized light. The p-polarized signal light is then focused by the GRIN lens, coupled back into the PM fiber, transmitted by the PBS, detected by an avalanche photodetector (APD) (Hamamatsu), and collected by a DAQ (Agilent) to a PC. Meantime, the unwanted specular reflections at the fiber end and the GRIN lens end-face remain s-polarized and thereby get reflected by the PBS without entering the detector. Simply put, the polarization sensitive components

including PBS, PM fiber and QWP work together to turn the polarization direction of the signal light by 90° while maintain the polarization direction of the unwanted reflection so that the two will be divided into separate paths.

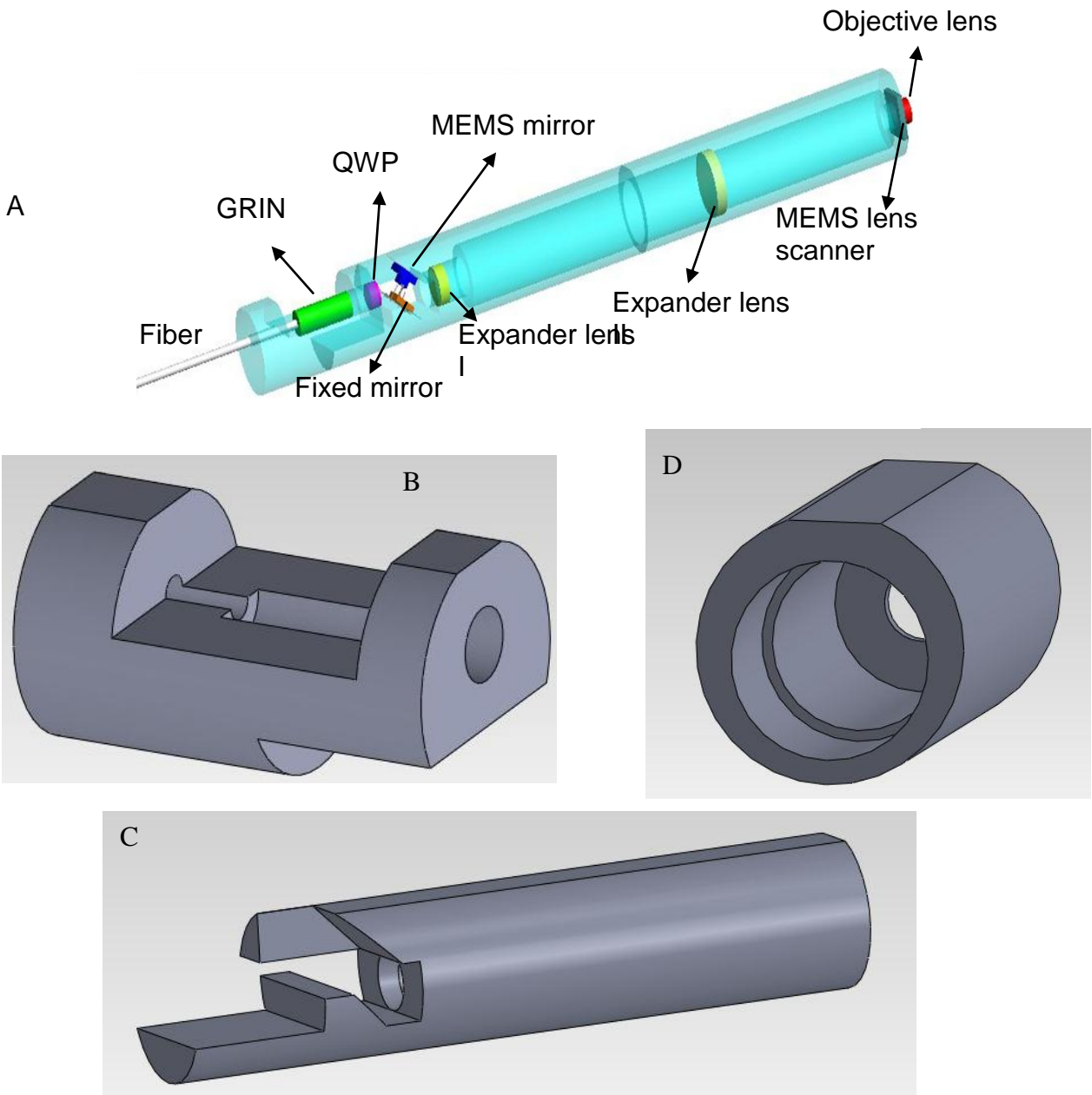


Figure 5-22. 3D endoscopic probe mechanical design. A) 3D model of the complete endoscopic probe with components. B) Piece I of the probe. C) Piece II of the probe. D) Piece III of the probe.

### 5.4.2 Endoscopic Probe Design

The 3D model of the confocal endoscopic probe is given in Figure 5-22A. As shown in the model, the components are a fiber, a GRIN lens, a QWP, a 2D MEMS micromirror, a fixed mirror, a pair of beam expansion lens, a 1D MEMS lens scanner, and a micro-objective. The probe is a precision-machined metal mount with three pieces assembled and bonded together. The three pieces of the probe are shown in Figure 5-22B to Figure 5-22D.

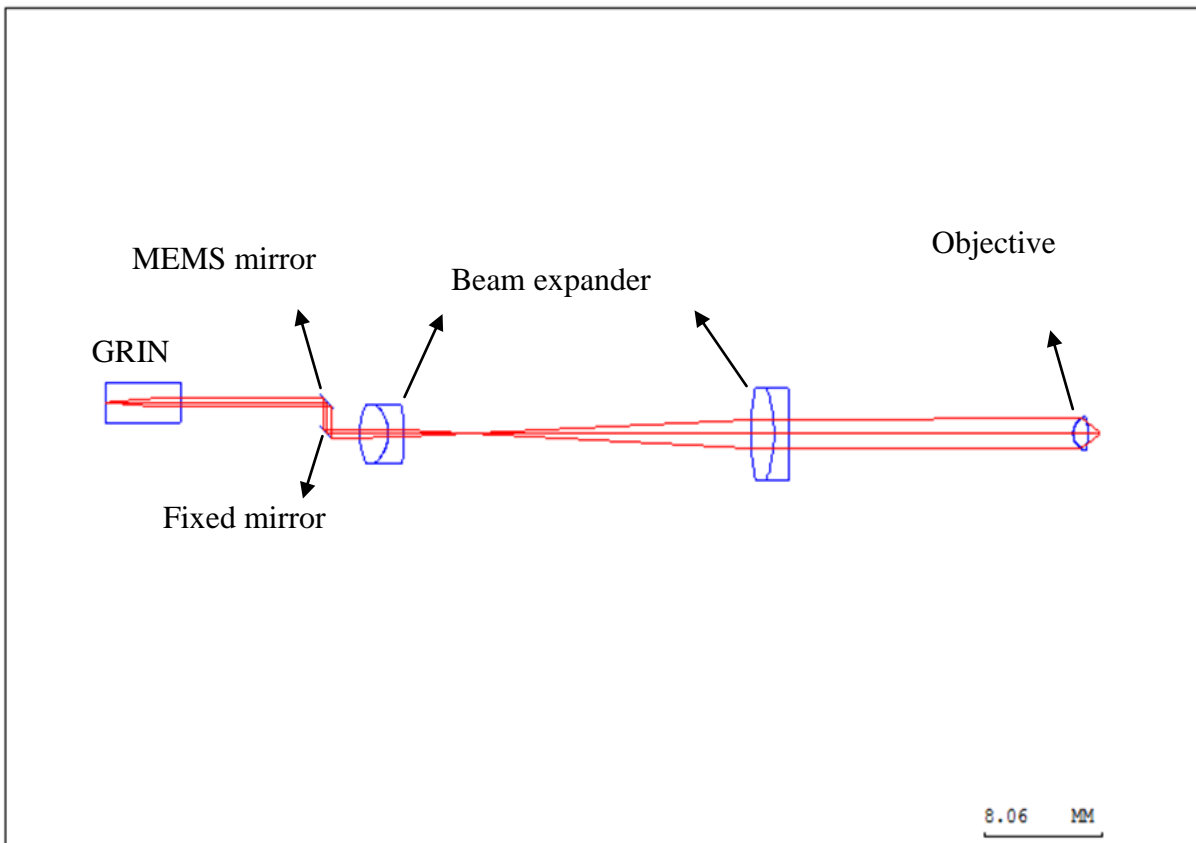


Figure 5-23. Optical design of the confocal endoscopic probe

The optical design of the confocal endoscopic probe is shown in Figure 5-23. The point source from the fiber will be collimated by the quarter-pitch GRIN lens, 2D lateral scan by the MEMS mirror, deflected by the fix mirror to forward direction. The collimated beam after GRIN lens is 0.54 mm in diameter, which will under-fill the objective and lead

to small effective NA. So a pair of beam expander lenses (Edmund Optics,  $f_1= 6 \text{ mm}$ ,  $f_2= 20 \text{ mm}$ ) is used to expand the beam by  $3.33 \times$  to  $1.8 \text{ mm}$  in diameter. The beam-expander pair is also used for aberration correction. The expanded beam is collimated after the second beam expander lens and then focused by the aspheric miniature objective to the sample. The objective is scanned in axial direction by the MEMS lens scanner to perform depth scan. The MEMS mirror is located at the conjugate plane of the back focus plane of the objective.

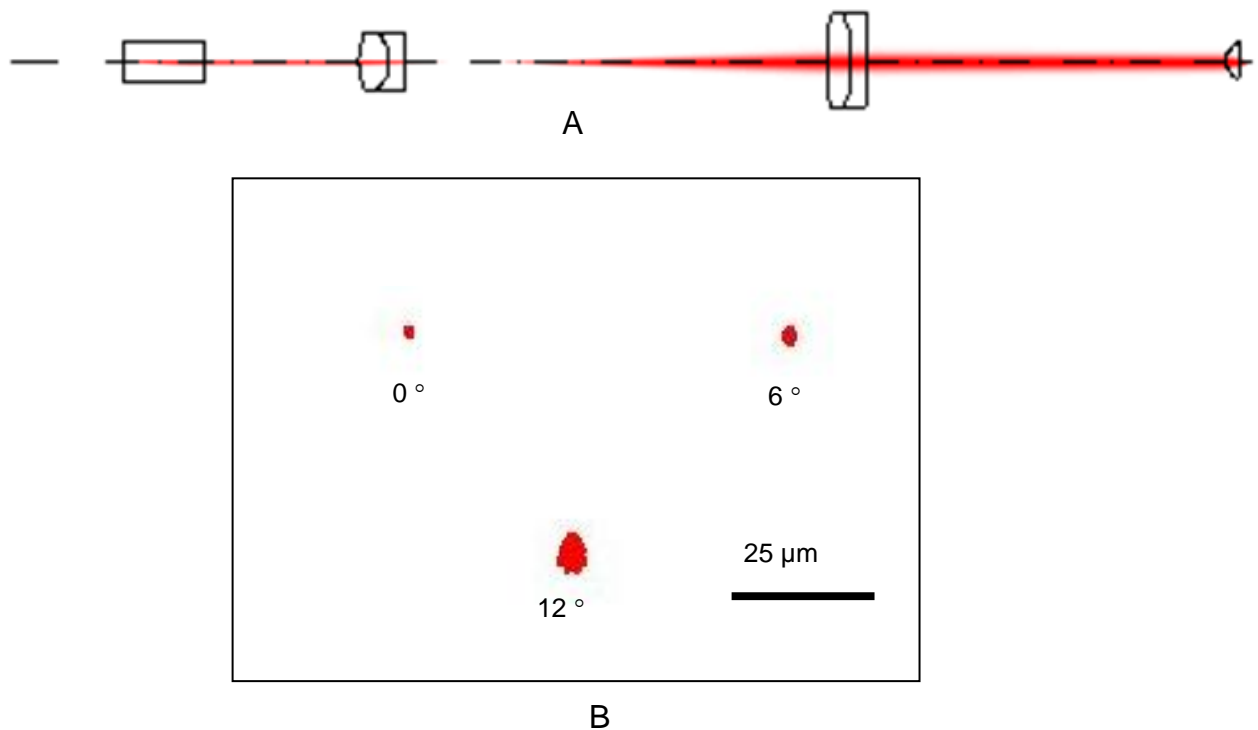


Figure 5-24. Optical simulation results of the confocal endoscopic probe. A) Gaussian tracing results of the optical system. B) Spot diagram at different optical scan angles. RMS spot sizes at optical scan angles of  $0^\circ$ ,  $6^\circ$ , and  $12^\circ$  are  $0.49 \mu\text{m}$ ,  $0.88 \mu\text{m}$ , and  $2.8 \mu\text{m}$ , respectively.

Figure 5-23 is also a ray-tracing result of the optical system model by CODE V. The simulation model in CODE V starts from model the single mode fiber output with

NA of 0.14, and then self-focus material is defined in CODE V to model the quarter-pitch GRIN lens. The Gaussian trace results show the beam diameter after collimating by SLW30 GRIN lens is 0.54 mm, which match the theoretical calculations. Then two achromatic lenses of diameter of 3 mm and 5 mm from Edmond Optics are added to the model. Then the light is focused by the aspheric miniature objective (Thorlabs,  $f= 1.45$  mm,  $NA=0.55$ ).

The simulations results are shown in Figure 5-24. Figure 5-24A is the Gaussian beam tracing result of the optical system that shows a focused beam spot size of  $1 \mu\text{m}$ . Figure 5-24B shows that the RMS spot sizes at optical scan angles of  $0^\circ$ ,  $6^\circ$ , and  $12^\circ$  are  $0.49 \mu\text{m}$ ,  $0.88 \mu\text{m}$ , and  $2.8 \mu\text{m}$ , respectively.

#### **5.4.3 MEMS Scanning Devices**

The 2D lateral scan is accomplished by a MEMS mirror with a footprint of  $2 \text{ mm} \times 2 \text{ mm}$  (Figure 5-25). The MEMS mirror has a mirror plate symmetrically supported by four inverted-series-connected (ISC) bimorph actuators [137]. The ISC bimorph actuator has inverted bimorph, non-inverted bimorph, and sandwiched overlap connected in series to form an S-shaped beam. Figure 5-25A and Figure 5-25B show an SEM picture of one ISC actuator and an SEM of the MEMS mirror, respectively. This mirror is fabricated using a combined surface- and bulk-micromachining process as reported in [137]. The mirror scans optical angles of  $\pm 26^\circ$  at 4.5 V (Figure 5-25C), and the resonance is 460 Hz (Figure 5-25D). Tip-tilt motion is generated by differentially driving two opposite actuators of the mirror. The frequency response is measured also using a Polytec OFV-511 laser Doppler vibrometer.

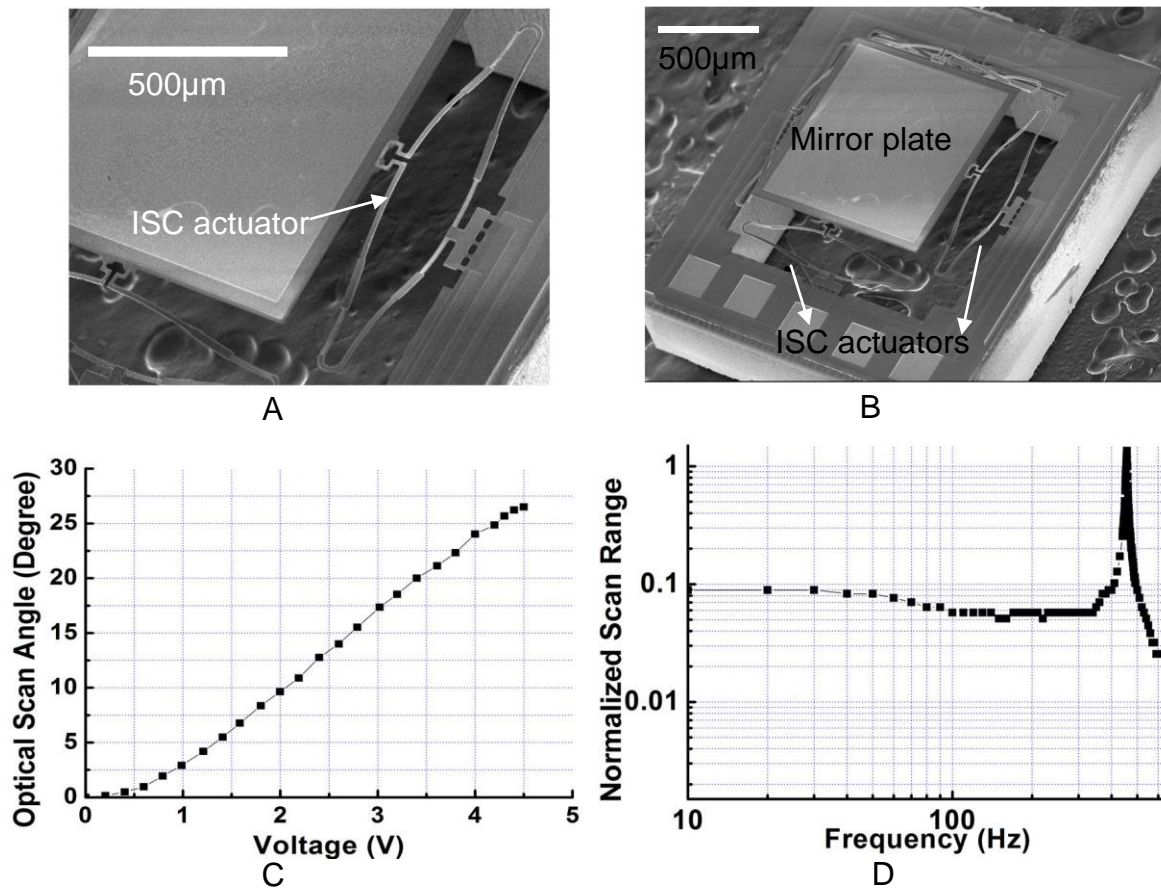


Figure 5-25. SEMs and characterizations of the 2D ISC micromirror used in the endomicroscope. A) SEM of an ISC actuator. B) SEM of a MEMS mirror. C) Optical scan angle vs. driving voltage. D) Frequency response.

An electrothermal tunable microlens is used to perform the depth scan. The tunable MEMS lens consists of a MEMS lens-scanner with a central opening (Figure 5-26A) and a 2.4 mm-diameter glass objective lens assembled onto the platform of the scanner (Figure 5-26B). The central platform in the MEMS lens-scanner is symmetrically supported by four electrothermal lateral-shift-free large-vertical-displacement (LSF-LVD) actuators [136] at two sides (Figure 5-26A). The LSF-LVD actuator is comprised of three Al/SiO<sub>2</sub> bimorphs with two rigid frames connected in between. The actuation mechanism is electrothermal actuation, with a thin layer of Pt embedded along the bimorphs as the heater. The platform is elevated upward at about

800  $\mu\text{m}$  after the device release due to the residual stresses in the bimorph beams. And the platform together with the objective lens will be actuated downward upon electrical current introduces Joule heating and thereby bending of the bimorph beams.

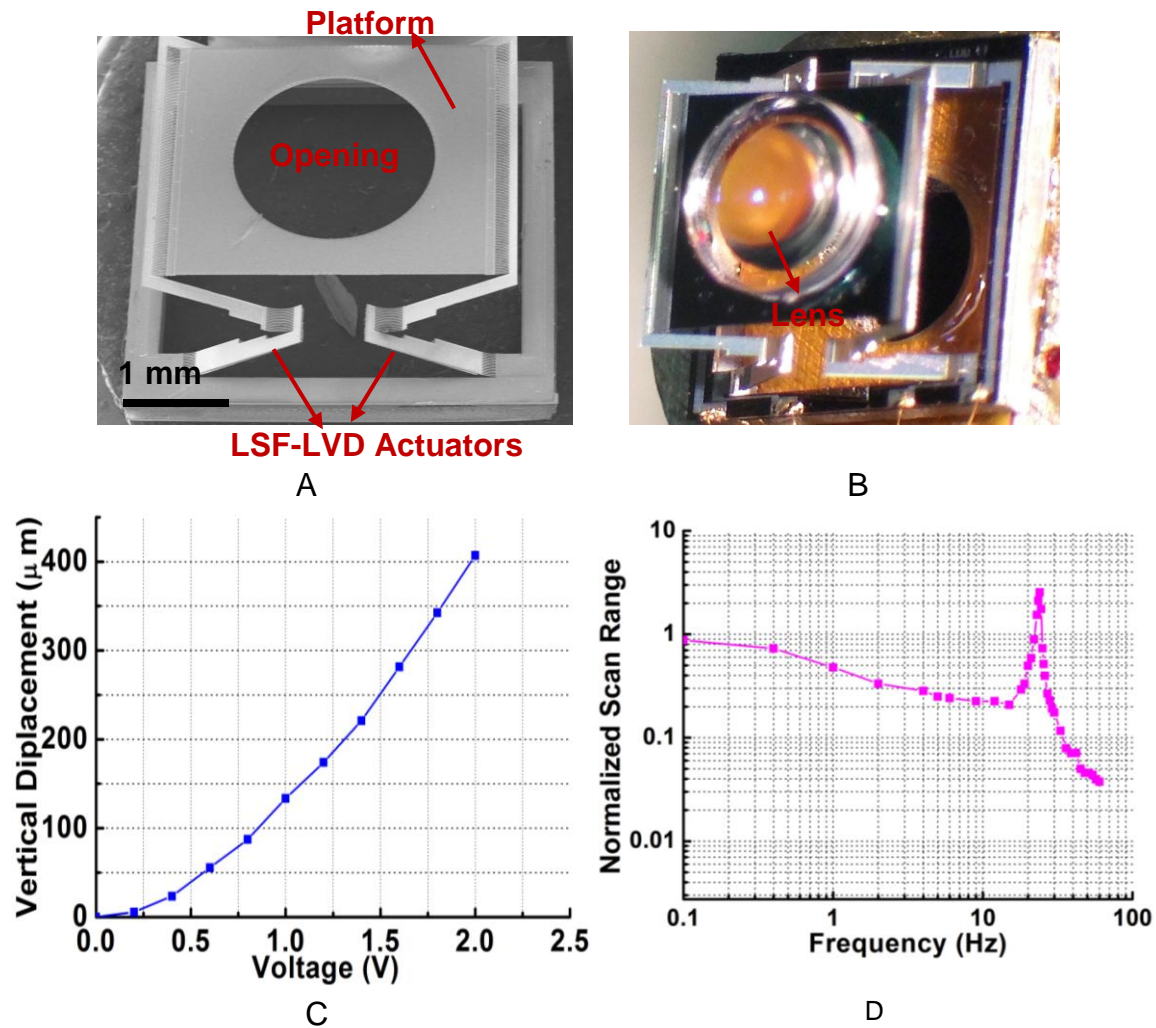


Figure 5-26. Photos and characterizations of the tunable lens used in the 3D confocal scanning endomicroscope. A) SEM of a lens scanner. B) Photograph of an assembled tunable lens. C) Z displacement vs. voltage. D) Frequency response.

A miniature glass lens with a diameter of 2.4 mm, a NA of 0.55 and a back focal length of 0.88 mm is selected as the objective lens for this system. The lens has diffraction-limit performance at  $\lambda=638$  nm. The lens is glued by UV glue to the platform

with the clear aperture of the lens aligned to the central opening in the platform. The vertical elevation of the platform after the lens being assembled is 510  $\mu\text{m}$ . The device footprint of the lens scanner is 4.4 mm  $\times$  4.4 mm.

The vertical displacement and frequency response of this device are experimentally measured and shown in Figure 5-26C and Figure 5-26D. The vertical displacement is measured by an Olympus BX51 microscope equipped with a QC200 micro-position recorder. To measure the vertical displacement, the lens scanner is operated at the piston mode by simultaneously driving all the actuators with a same dc voltage, and then gradually changing the added dc voltage. After each step of voltage change, the microscope is refocused onto the mirror plate and the coordinates of multiple points on the mirror plate are recorded. A vertical actuation range of 400  $\mu\text{m}$  is obtained at only 2 V (Figure 5-26C). The frequency response is measured using a Polytec OFV-511 laser Doppler vibrometer. The frequency response of the assembled lens scanner is shown in Figure 5-26D with the first resonance peak at about 24 Hz.

Figure 5-27 shows an assembled probe with a diameter of 7 mm. The probe mount consists of three separate precision-machined metal pieces. The first piece is designed to hold fiber, GRIN and QWP. The fiber with the end cleaved is inserted into the trench machined in the first metal piece. The GRIN lens is then inserted into the metal base with its end face adhesively attached to the fiber tip by optical UV glue. Then the QWP is inserted and carefully rotated to align its axis at 45° to the incident light polarization direction. The second piece is used to house the MEMS mirror, the fixed mirror and the first expander lens, while the third piece is loaded with the second expander lens and the MEMS tunable objective lens. Flexible printed circuit boards

(FPCBs) are used for the electrical connections. Two FPCBs are first adhesively bonded to the metal pieces and then the MEMS mirror and MEMS lens are placed on top of the FPCBs, adhesively bonded to the FPCBs, and then electrically connected to the pads on FPCBs by Silver Epoxy. Finally, the three assembled pieces are bonded together to form a complete endoscopic imaging probe.

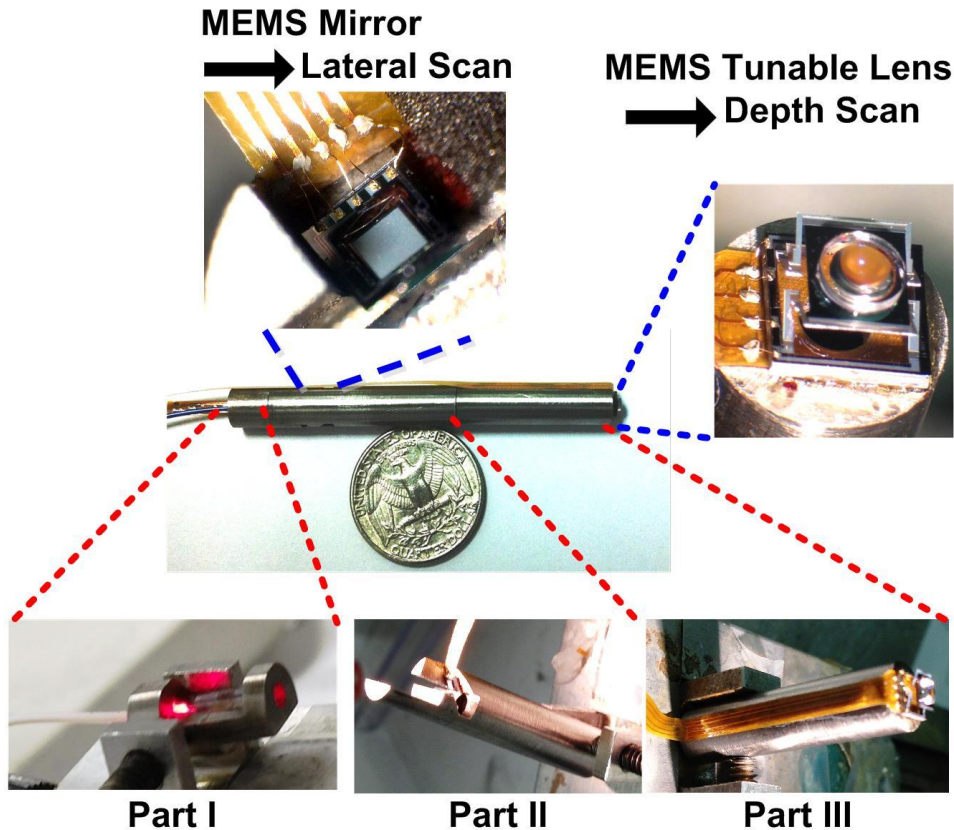


Figure 5-27. Photos of the assembled confocal endoscopic probe

#### 5.4.4 System Characterization

Both the lateral and axial resolutions have been characterized. Figure 5-28A shows an en face confocal reflectance image of the elements in Group 7 of a USAF resolution target by the confocal imaging system. There is some distortion in the image because the fast axis of the MEMS mirror scans an arc near the resonance peak and the speed of the mirror is not exactly uniform along the scan path. The resolution would

degrade as the beam scans towards the edge of the field of view, but the reflectance image of the resolution target shows that the smallest pattern with a width of  $2.2\ \mu\text{m}$  is still resolvable.

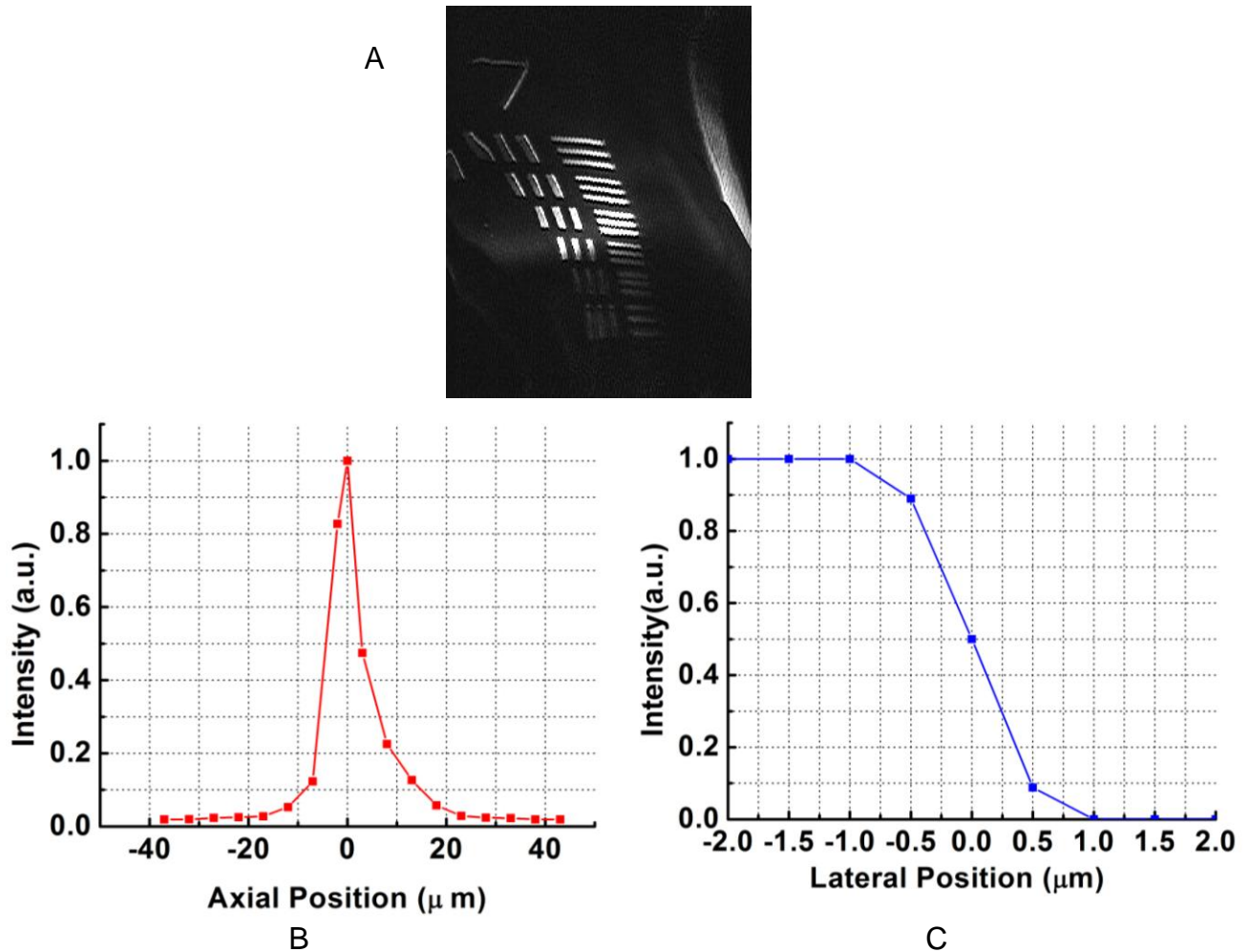


Figure 5-28. System characterization results of the 3D confocal scanning endomicroscope. A) Reflectance image of group 7 elements in a USAF resolution target. The smallest elements are  $2.2\ \mu\text{m}$  wide. B) Axial resolution measurement. C) Lateral resolution measurement.

Figure 5-28B and Figure 5-28C show the measurement results of the axial resolution and the lateral resolution, respectively. The axial resolution is measured by translating a mirror surface axially across the focal plane and recording the change of the signal strength detected by the APD and the FWHM axial resolution is found to be

7.0  $\mu\text{m}$ . The lateral resolution was measured by laterally translating the reflective chrome surface of the resolution target on the focal plane and the 10%--90% edge width is measured as 1  $\mu\text{m}$ .

#### **5.4.5 Imaging Experiments and Results**

Confocal imaging experiments have been performed using this MEMS-based confocal scanning endomicroscope system. 2D and 3D confocal reflectance images of micro-patterns (Figure 5-29), micro-particles embedded in PDMS (Figure 5-30), Onion skin (Figure 5-31) and acute rat brain tissue (Figure 5-32) have been obtained.

During the experiments, the four actuators of the 2D MEMS mirror are grouped into two pairs with each pair including two actuators at the opposite sides of the mirror plate. The actuator pair controlling the x-scan is differentially driven with a ramp waveform of 0 ~ 2 V at 450 Hz. The scan in x- direction is driven near the resonance peak for large scan angle. The actuator pair driving the y- direction scan is differentially driven with a ramp waveform of 0 ~ 4 V at 0.75 Hz. Meanwhile, the z-direction scan is performed by simultaneously driving all the actuators of the MEMS lens scanner with a ramp waveform of 0 ~ 2 V at 1 mHz.

Figure 5-29A shows a 2D reflectance confocal image of micro-patterns on the USAF resolution target. The micro-patterns shown in the figure include a number and a bar. Figure 5-29B is a 3D volume-rendered image of the USAF resolution target covered by a 200- $\mu\text{m}$  thick glass cover slide. The layers from up to down are the top surface of the glass slide, the bottom surface of the glass slide, and the micro-patterns. The imaging volume shown in this figure is 180  $\mu\text{m}$   $\times$  180  $\mu\text{m}$   $\times$  400  $\mu\text{m}$ .

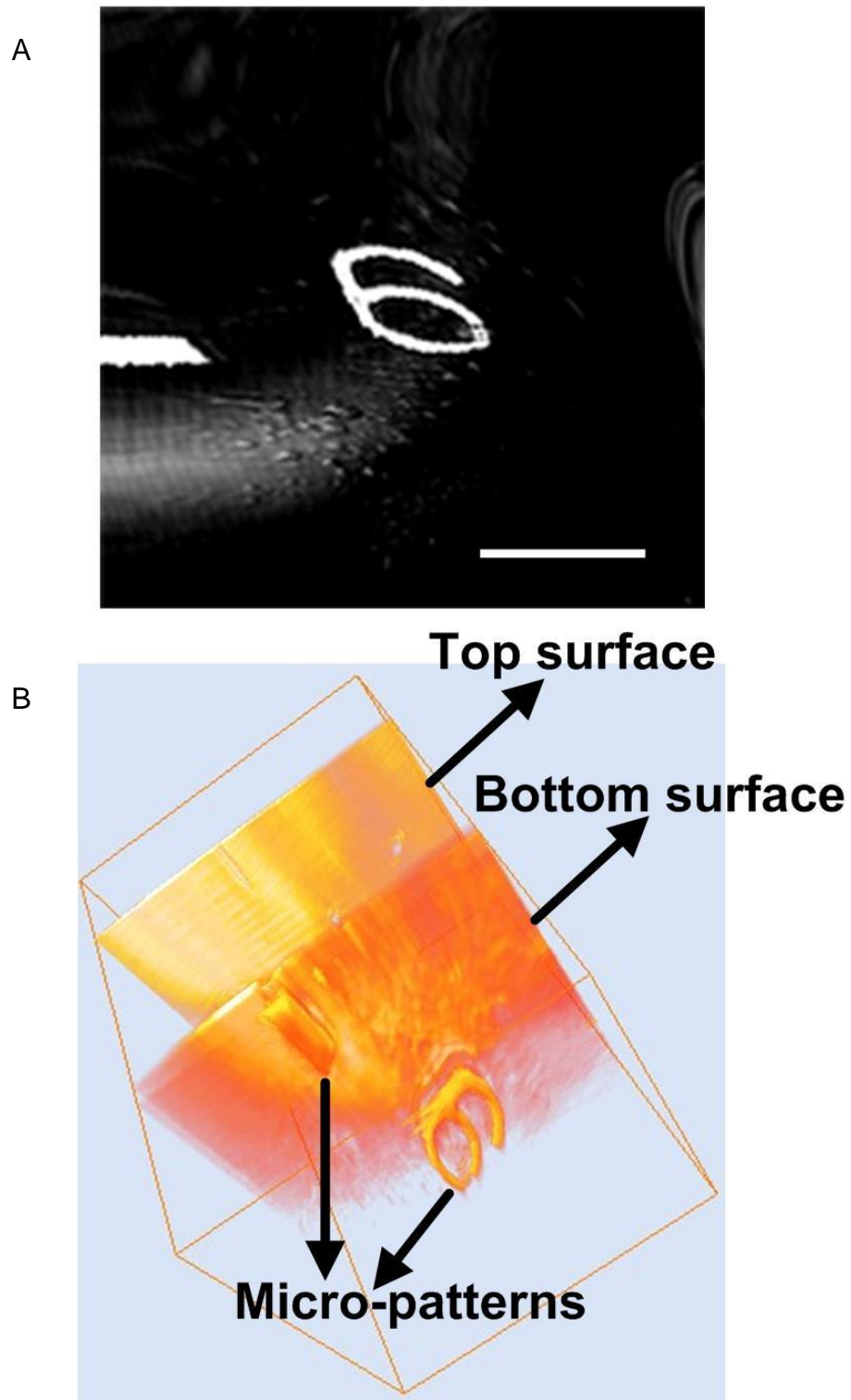


Figure 5-29. 2D and 3D confocal reflectance images of micro-patterns by the 3D confocal scanning endomicroscope. A) 2D reflectance image of the micro-patterns. B) 3D volume-rendered image of the micro-patterns under a 200- $\mu\text{m}$  thick glass slide.

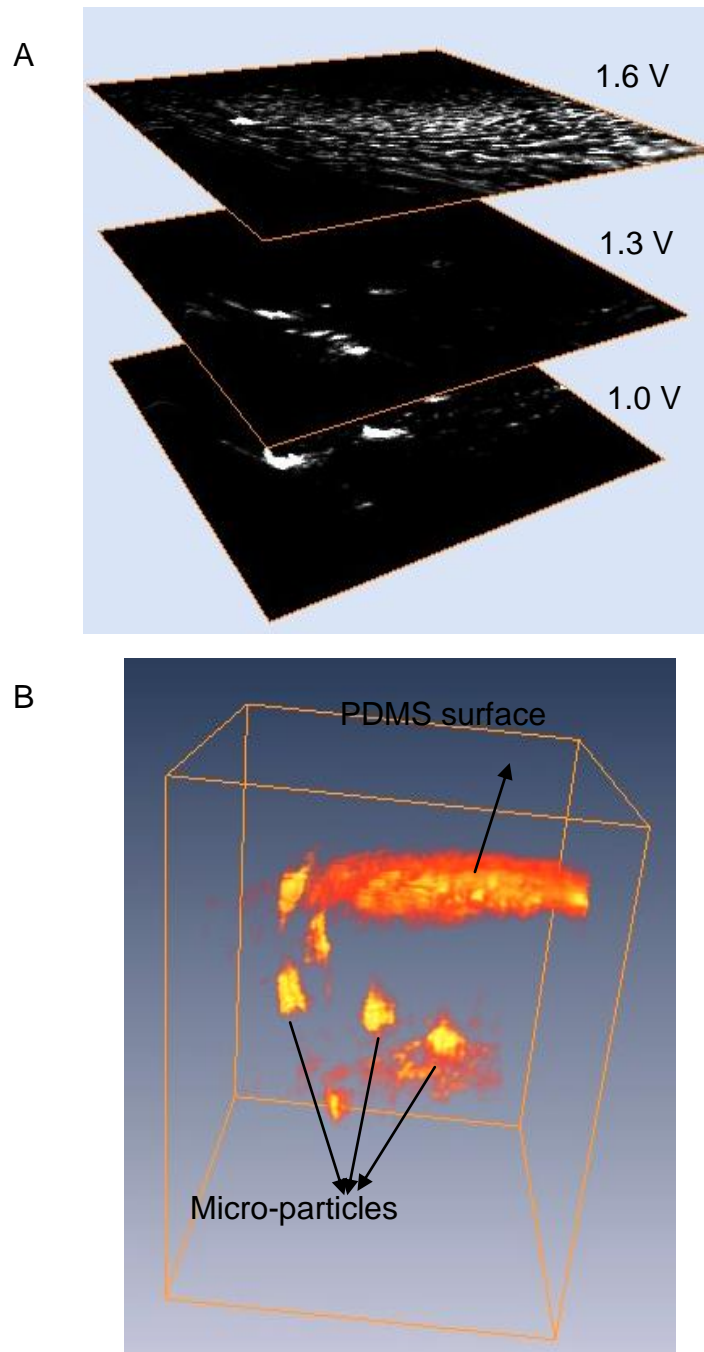


Figure 5-30. 2D and 3D confocal reflectance images of micro-particles embedded in PDMS by the 3D confocal scanning endomicroscope. A) Stack of 2D confocal reflectance images of the micro-particles at different depths. The driving voltages of the MEMS lens scanner from up to bottom are at: 1.6 V, 1.3 V, and 1 V. The image sizes are  $180\ \mu\text{m} \times 180\ \mu\text{m}$ . B) 3D volume-rendered image of the micro-particles embedded in PDMS.

Figure 5-30A shows a stack of 2D confocal reflectance images of the micro-particles acquired at different depths of the sample. The image sizes are  $180\ \mu\text{m} \times 180\ \mu\text{m}$ . The micro-particles are alloy particles with the diameters in the range of microns to tens of microns. The driving voltages on the MEMS lens scanner from up slice to bottom slice were 1.6 V, 1.3 V and 1.0 V, corresponding to the axial displacements of 281  $\mu\text{m}$ , 197  $\mu\text{m}$  and 133  $\mu\text{m}$ , respectively. Figure 5-30B is a 3D volume rendered image of the micro-particles embedded in PDMS reconstructed by stacking the 2D image slices (3D image rendered by Amira). The imaging volume shown in Figure 5-29B is about  $180\ \mu\text{m} \times 180\ \mu\text{m} \times 250\ \mu\text{m}$ .

Figure 5-31A and Figure 5-31B are the 2D and 3D confocal reflectance images of onion skin sample. The imaging volume shown in this figure is  $180\ \mu\text{m} \times 180\ \mu\text{m} \times 270\ \mu\text{m}$ .

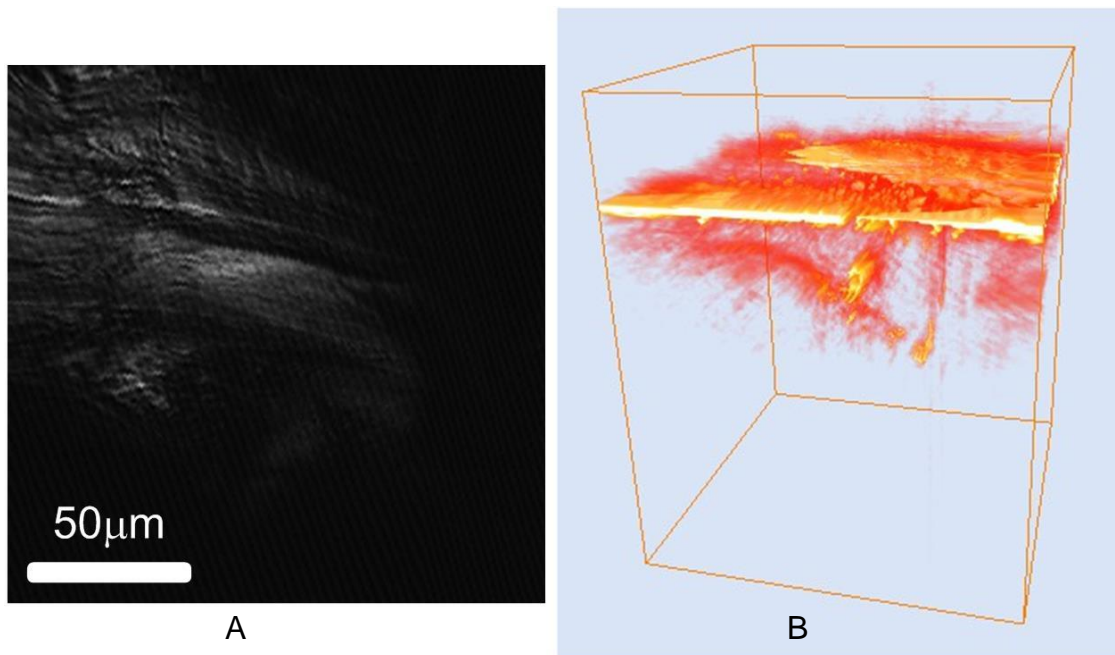


Figure 5-31. 2D and 3D confocal reflectance images of onion skin by the 3D confocal scanning endomicroscope. A) 2D reflectance image of the onion skin sample. B) 3D volume-rendered image of the onion skin sample.

Figure 5-32A and Figure 5-32B are the 2D and 3D confocal reflectance images of an acute rat brain tissue sample. The image volume shown in Figure 5-32B is  $180\ \mu\text{m} \times 180\ \mu\text{m} \times 380\ \mu\text{m}$ .

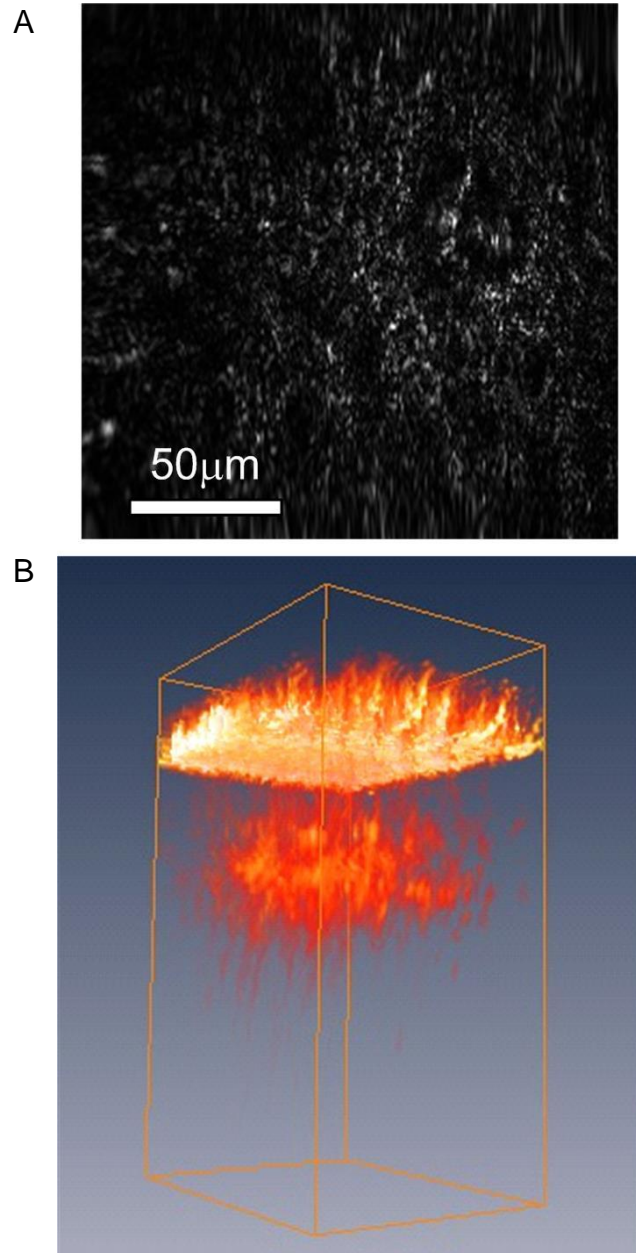


Figure 5-32. 2D and 3D confocal reflectance images of rat brain tissue by the 3D confocal scanning endomicroscope. A) 2D confocal reflectance image of the acute rat brain tissue. B) 3D volume-rendered image of the rat brain tissue.

## 5.5 Chapter Summary

Focal-tunable microlenses driven by electrothermal lens scanners have been designed, fabricated, assembled, and tested. Three generations of MEMS-based confocal imaging systems using the developed electrothermal microlens scanners for depth scan have been present. The 1<sup>st</sup>-generation 2D CSM demonstrates the capability and advantages of the tunable microlens for automatic depth scan in confocal microscopic imaging. The 2<sup>nd</sup>-generation 3D CSM demonstrates the 3D full-MEMS scanning system by incorporating an electrothermal 2D micromirror for lateral scan with an electrothermal tunable microlens for axial scan. The full-MEMS 3D scan engine has been demonstrated as a viable way to achieve large-scan-range 3D confocal imaging at low voltage and small footprint. 2D and 3D confocal images have been successfully obtained by this system. The 3<sup>rd</sup>-generation confocal scanning endomicroscope is an endoscopic system aiming to realize *in-vivo* confocal 3D imaging by the full-MEMS 3D scanning system and high-performance micro-optics design. The endomicroscopic system has been designed, simulated and constructed. The prototype of the endoscopic probe has also been designed, manufactured and assembled. 2D and 3D confocal reflectance images of micro-patterns, micro-particles embedded in PDMS, onion skin and rat brain tissue have been obtained by this system. Due to its small size, 3D imaging capability and high optical performance, this miniature MEMS-based confocal microendoscope is attractive for early cancer diagnosis.

## CHAPTER 6 CONCLUSION AND FUTURE WORK

The primary goal of this research is to develop MEMS micromirrors and microlenses for endoscopic biomedical imaging applications, and to develop the MEMS-based biomedical imaging systems including MEMS-based endoscopic OCT, MEMS-based CSM and MEMS-based confocal scanning endomicroscope.

To achieve this research goal, the research efforts have been put into the design and fabrication of a TSV micromirror, and the design and instrumentation of an endoscopic OCT system that integrates a TSV micromirror-based miniature endoscopic probe. To further increase the area efficiency and to explore new curved actuator design, this research has also developed a curved actuator design, the CCBA, and applied this actuator to two new MEMS micromirror designs. And to realize MEMS-based endoscopic imaging depth scan, multiple designs of MEMS lens scanners and MEMS tunable micro-lenses have been developed. In order to demonstrate the capabilities of these tunable microlenses, three generations of MEMS-based confocal imaging systems have been developed that include a 2D CSM, a 3D CSM, and a 3D confocal scanning endomicroscope.

### **6.1 Research Accomplishments**

Tasks that have been accomplished for this research are summarized as follows:

A 2D electrothermal micromirror with through-silicon vias has been designed, fabricated, and characterized. This TSV micromirror has a device footprint of only 1.5 mm × 1.5 mm. The mirror demonstrates optical scan angle of  $\pm 16^\circ$  at 3.6 V for both x- and y-axis and vertical displacement of 215  $\mu\text{m}$  at 4 V. The resonance frequency measurement shows the first resonance peak at 659 Hz. This TSV mirror has four

through-silicon-vias integrated at the four corners to ease the electrical connection and to reduce the space occupied by electrical connection wires. This device is fabricated by a combined surface- and bulk- micromachining process.

A time-domain endoscopic OCT system using the TSV mirror for 2D beam scan has been developed and experimentally demonstrated. A miniature 2.6 mm-diameter OCT endoscopic probe in the sample arm performs the OCT imaging *in vivo*. The endoscopic OCT system has 10  $\mu\text{m}$  axial resolution, 53 dB measured system sensitivity, 2.5 fs/s frame rate. The endoscopic OCT probe consists of a TSV interconnect MEMS mirror, a GRIN lens, a single-mode fiber and a metal mount base and the working distance of the probe is 1.5 mm in air. The MEMS mirror with TSVs proves to be an effective way to shrink the endoscopic probe size as well as ease the wire bonding and probe assembling.

A new type of curved actuator has been designed and fabricated to actuate circular micromirrors with improved area efficiency, while achieving large scan range at low voltage drive. This CCBA actuator consists of three curved concentric Aluminum/Tungsten bimorphs for fast thermal response and high sensitivity, and two rigid frames connected in between for scan range amplification. Analytical and finite element models show that the CCBA actuator has unique characteristics of the coupled bending and twisting motion, and also the in-plane movement because of the twisting. It has also been found that the symmetrical arrangement of the actuators could effectively reduce the twisting and the in-plane movement. The analysis and simulations on curved electrothermal bimorph actuators have been used to guide the design of mirrors with curved bimorph actuators.

Two mirrors based on the CCBA actuator have been designed, fabricated and characterized. Large scan range at low driving voltage has been demonstrated. A tip-tilt-piston micromirror with a circular mirror plate based on this actuator design has been proposed and fabricated. The mirror is capable of scanning  $\pm 11^\circ$  at 0.6 V, and generating a 227  $\mu\text{m}$  piston displacement at only 0.8 V. The measured lateral shift and tilt angle of the mirror plate are less than 7  $\mu\text{m}$  and  $0.7^\circ$ , respectively, through the entire piston displacement. A piston-only micromirror has also been demonstrated, and it has even smaller lateral shift of less than 3  $\mu\text{m}$  and tilt of less than  $0.4^\circ$  through the piston scan range. This mirror generates large vertical displacement of 200  $\mu\text{m}$  at 0.9 V.

Focal tunable microlenses driven by electrothermal microlens scanners have been developed. The miniature electrothermal microlens scanners are able to actuate microlens with large tunable range from hundreds of microns to 1 mm under low driving voltage. The microlens scanners have two sets of LSF-LVD actuators symmetrically located at two sides, and have the last bimorphs of both actuators line-anchored to the edge of the platform to ensure a stable actuation. The platform used to hold the microlens has a central hole to allow light to pass through. The device is fabricated using a combined surface- and bulk-micromachining process. Multiple types of microlenses with various parameters have been integrated with the MEMS lens scanners for different imaging applications.

A 2D CSM using a microlens scanner for large-tunable-range depth scan and a motor-driven stage for lateral scan has been demonstrated. The microlens scanner is assembled with a spherical glass lens with a diameter of 1 mm and a thickness of 1 mm. The working distance is 3 mm in this lens with a NA of 0.17. The assembled tunable

lens is able to scan 0.9 mm vertical displacement at only 6.3 V. The mechanical resonance of the device is 79 Hz. The FWHM axial resolution of the system is 38.0  $\mu\text{m}$  and the 10%-90% edge width lateral resolution is about 1.25  $\mu\text{m}$ . 2D confocal images have been obtained on alloy micro-particles embedded in polymer and rat skin tissue.

A 3D CSM based on a full-MEMS 3D scanning system has been developed. The full-MEMS 3D scanning system includes a MEMS lens scanner that can axially scan for large displacement at small voltage and a MEMS 2D mirror that can scan large angles at both lateral directions at low voltage. An aspheric glass lens with a diameter of 2.4 mm, a NA of 0.55 and a back focal length of 0.88 mm is assembled onto the lens scanner. The device footprint of the lens scanner is 3.3 mm  $\times$  3.3 mm. A vertical actuation range of 515  $\mu\text{m}$  was obtained at only 3.2 V. The frequency response of the assembled lens scanner shows the first resonance peak at about 30 Hz. The FWHM axial resolution and the lateral resolution of the 3D CSM system are found to be 9.0  $\mu\text{m}$  and 1.2  $\mu\text{m}$ , respectively. 2D and 3D reflectance images have been taken on a PDMS sample with micro-particles embedded inside an acute rat brain tissue slice by this system with an imaging volume of about 120  $\mu\text{m}$   $\times$  120  $\mu\text{m}$   $\times$  500  $\mu\text{m}$ .

A 3D confocal scanning endomicroscope with 3D MEMS scan, high-performance optical system design and compact probe design has been developed. Both lateral and axial scans are accomplished by MEMS devices: a 2D micromirror for large-angle lateral scan and a tunable microlens for large-range axial scan both at low voltage. The MEMS 3D scan engine achieves a lateral scan range of over  $\pm 26^\circ$  and a depth scan of over 400  $\mu\text{m}$ . The MEMS scanners and high-quality micro-optics are incorporated in a compact endoscopic probe. A fiber-optic polarization-sensitive confocal scanning

endomicroscope system with this miniature endoscopic probe integrated has been developed. The FWHM axial resolution is 7.0  $\mu\text{m}$  and the lateral resolution basing on the 10%--90% edge width criteria is measured as 1  $\mu\text{m}$ . 2D and 3D confocal reflectance images of micro-patterns, micro-particles embedded in PDMS, onion skin and rat brain tissue have been obtained by this system with an imaging volume of about 180  $\mu\text{m}$   $\times$  180  $\mu\text{m}$   $\times$  380  $\mu\text{m}$ . Due to its small size and 3D imaging capability, this miniature MEMS-based confocal microendoscope is attractive for *in-vivo* early cancer diagnosis.

## 6.2 Future Work

The MEMS micromirrors and MEMS microlenses, and the endoscopic OCT and confocal imaging systems developed in this work have shown great potentials for *in vivo* cancer diagnosis and clinical use. However, to realize the end goal, additional work needs to be done in future.

For MEMS-based endoscopic OCT system, it has been found during the prototype probe assembling that the MEMS micromirrors are susceptible to external shock or vibration induced by improper handling. The reliability of the micromirrors needs to be studied, and experimental tests on the long-term reliability need to be carried out for future designs. Optimization of actuator structures, materials and fabrication process is suggested to develop more reliable and durable devices.

The CCBA-based micromirrors have introduced a new and interesting topic on curved actuators. Studies on curved actuators and designs of new circular mirrors using curved actuators are suggested. Besides, the CCBA has shown unique characterizations of the coupled bending and twisting motion, and also the in-plane movement because of the twisting. These unique characteristics of CCBA's may be

useful for generating special scanning patterns by utilizing the bending, twisting and in-plane movement. 2D or even 3D scan patterns can potentially be generated by a single CCBA or its modifications. Therefore, another suggested future study is to manage the coupled twisting and bending of CCBA in order to generate desirable 2D/3D patterns. In addition, the MEMS mirrors based on the CCBA show some stress on the mirror plate which introduces additional curvature of the mirror plate. This can be addressed either by structure design with improved stress balance or by process optimization.

As for the MEMS tunable microlenses, it's been found that the repeatability and reliability of assembled devices needs to be improved. Since the glass lens adds weight as well as stress to the MEMS scanners, the scanner is more susceptible to external shock or vibration. Future study is suggested on researching the reliability and repeatability of this device. Besides, other than the application in confocal scanning endomicroscopy, the MEMS tunable microlenses are also appealing for nonlinear optical endomicroscopy and optical coherence endomicroscopy applications. Future studies can be focused on developing MEMS-based nonlinear optical endomicroscopy or optical coherence endomicroscopy with tunable focal depth.

Furthermore, the MEMS-based confocal scanning endomicroscope prototype can be improved in several ways. First, fluorescence imaging may be added to the current prototype system since fluorescence can greatly enhance the contrast and the image quality. Second, more *in vivo* experiments on bio-samples may be taken to further demonstrate the imaging capacity of the system. Third, there is still room to shrink the probe size by modifying the optical design such as using even smaller objective while maintaining optical performance, or by increasing the form factor of the

MEMS microlens scanner. Also disposable endoscopic probe is another topic worth of study. Disposable endoscopic probe may pose low requirements on the reliability of MEMS devices.

## LIST OF REFERENCES

- [1] American Cancer Society, "Cancer Facts and Figures 2012," Atlanta, GA, 2012.
- [2] American Cancer Society, "Colorectal Cancer Facts & Figures 2011-2013," Atlanta, GA, 2011.
- [3] F. Koenig, J. Knittel and H. Stepp, "Diagnosing cancer in vivo," *Science*, vol. 292, no. 5520, pp. 1401-1403, May 18 2001.
- [4] G.J. Tearney, M.E. Brezinski, B.E. Bouma, S.A. Boppart, C. Pitris, J.F. Southern and J.G. Fujimoto, "In vivo endoscopic optical biopsy with optical coherence tomography," *Science*, vol. 276, no. 5321, pp. 2037-2039, 1997.
- [5] R. Weissleder and M.J. Pittet, "Imaging in the era of molecular oncology," *Nature*, vol. 452, no. 7187, pp. 580-589, 2008.
- [6] A.F. Fercher, W. Drexler, C.K. Hitzenberger and T. Lasser, "Optical coherence tomography-principles and applications," *Reports on progress in physics*, vol. 66, no. 2, pp. 239, 2003.
- [7] E.A. Swanson, J. Izatt, M.R. Hee, D. Huang, C. Lin, J. Schuman, C. Puliafito and J.G. Fujimoto, "In vivo retinal imaging by optical coherence tomography," *Opt.Lett.*, vol. 18, no. 21, pp. 1864-1866, 1993.
- [8] N. Nassif, B. Cense, B. Park, M. Pierce, S. Yun, B. Bouma, G. Tearney, T. Chen and J. de Boer, "In vivo high-resolution video-rate spectral-domain optical coherence tomography of the human retina and optic nerve," *Optics Express*, vol. 12, no. 3, pp. 367-376, 2004.
- [9] M.R. Hee, J.A. Izatt, E.A. Swanson, D. Huang, J.S. Schuman, C.P. Lin, C.A. Puliafito and J.G. Fujimoto, "Optical coherence tomography of the human retina." *Arch.Ophthalmol.*, vol. 113, no. 3, pp. 325, 1995.
- [10] G. Tearney, M. Brezinski, J. Southern, B. Bouma, M. Hee and J. Fujimoto, "Determination of the refractive index of highly scattering human tissue by optical coherence tomography," *Opt.Lett.*, vol. 20, no. 21, pp. 2258-2260, 1995.
- [11] J. Welzel, E. Lankenau, R. Birngruber and R. Engelhardt, "Optical coherence tomography of the human skin," *J.Am.Acad.Dermatol.*, vol. 37, no. 6, pp. 958-963, 1997.
- [12] J. Welzel, C. Reinhardt, E. Lankenau, C. Winter and H. Wolff, "Changes in function and morphology of normal human skin: Evaluation using optical coherence tomography," *Br.J.Dermatol.*, vol. 150, no. 2, pp. 220-225, 2004.

- [13] G. Tearney, M. Brezinski, J. Southern, B. Bouma, S. Boppart and J. Fujimoto, "Optical biopsy in human gastrointestinal tissue using optical coherence tomography." *Am.J.Gastroenterol.*, vol. 92, no. 10, pp. 1800, 1997.
- [14] M.V. Sivak, K. Kobayashi, J.A. Izatt, A.M. Rollins, R. Ung-Runyawee, A. Chak, R.C.K. Wong, G.A. Isenberg and J. Willis, "High-resolution endoscopic imaging of the GI tract using optical coherence tomography," *Gastrointest.Endosc.*, vol. 51, no. 4, pp. 474-479, 2000.
- [15] A. Sergeev, V. Gelikonov, G. Gelikonov, F. Feldchtein, R. Kuranov, N. Gladkova, N. Shakhova, L. Snopova, A. Shakhov and I. Kuznetzova, "In vivo endoscopic OCT imaging of precancer and cancer states of human mucosa," *Optics Express*, vol. 1, no. 13, pp. 432-440, 1997.
- [16] Y. Pan, Q. Wu, Z. Wang, P. Brink and C. Du, "High-resolution imaging characterization of bladder dynamic morphophysiology by time-lapse optical coherence tomography," *Opt.Lett.*, vol. 30, no. 17, pp. 2263-2265, 2005.
- [17] M.J. Manyak, N.D. Gladkova, J.H. Makari, A.M. Schwartz, E.V. Zagaynova, L. Zolfaghari, J.M. Zara, R. Iksanov and F.I. Feldchtein, "Evaluation of superficial bladder transitional-cell carcinoma by optical coherence tomography," *Journal of endourology*, vol. 19, no. 5, pp. 570-574, 2005.
- [18] J.M. Herrmann, M.E. Brezinski, B.E. Bouma, S.A. Boppart, C. Pitris, J.F. Southern and J.G. Fujimoto, "Two-and three-dimensional high-resolution imaging of the human oviduct with optical coherence tomography," *Fertil.Steril.*, vol. 70, no. 1, pp. 155-158, 1998.
- [19] M.A. Brewer, U. Utzinger, J.K. Barton, J.B. Hoying, N.D. Kirkpatrick, W.R. Brands, J.R. Davis, K. Hunt, S.J. Stevens and A.F. Gmitro, "Imaging of the ovary." *Technology in cancer research & treatment*, vol. 3, no. 6, pp. 617, 2004.
- [20] L.P. Hariri, G.T. Bonnema, K. Schmidt, A.M. Winkler, V. Korde, K.D. Hatch, J.R. Davis, M.A. Brewer and J.K. Barton, "Laparoscopic optical coherence tomography imaging of human ovarian cancer," *Gynecol.Oncol.*, vol. 114, no. 2, pp. 188-194, 2009.
- [21] A. Terentéva, A. Shakhov, A. Maslennikova, N. Gladkova, V. Kamensky, F. Feldchtein and N. Shakhova, "OCT in laryngology," in *Optical Coherence Tomography*. Springer Berlin Heidelberg, 2008, pp.1123-1150.
- [22] A.M. Karamzadeh, R. Jackson, S. Guo, J.M. Ridgway, H.S. Wong, G.S. Ahuja, M.C. Chao, L.H.L. Liaw, Z. Chen and B.J.F. Wong, "Characterization of submucosal lesions using optical coherence tomography in the rabbit subglottis," *Archives of Otolaryngology—Head & Neck Surgery*, vol. 131, no. 6, pp. 499-504, 2005.

- [23] M.R. Hee, J.A. Izatt, E.A. Swanson, D. Huang, J.S. Schuman, C.P. Lin, C.A. Puliafito and J.G. Fujimoto, "Optical coherence tomography of the human retina," *Arch.Ophthalmol.*, vol. 113, no. 3, pp. 325-332, 1995.
- [24] S.A. Boppart, M.E. Brezinski, B.E. Bouma, G.J. Tearney and J.G. Fujimoto, "Investigation of developing embryonic morphology using optical coherence tomography," *Dev.Biol.*, vol. 177, no. 1, pp. 54-63, 1996.
- [25] J.M. Schmitt, "Optical coherence tomography (OCT): A review," *Selected Topics in Quantum Electronics, IEEE Journal of*, vol. 5, no. 4, pp. 1205-1215, 1999.
- [26] Y. Pan, E. Lankenou, J. Welzel, R. Birngruber and R. Engelhardt, "Optical coherence-gated imaging of biological tissues," *Selected Topics in Quantum Electronics, IEEE Journal of*, vol. 2, no. 4, pp. 1029-1034, 1996.
- [27] J. Welzel, E. Lankenau, R. Birngruber and R. Engelhardt, "Optical coherence tomography of the human skin," *J.Am.Acad.Dermatol.*, vol. 37, no. 6, pp. 958-963, 1997.
- [28] M. Minsky, "Memoir on inventing the confocal scanning microscope," *Scanning*, vol. 10, no. 4, pp. 128-138, 1988.
- [29] R.H. Webb, "Confocal optical microscopy," *Reports on Progress in Physics*, vol. 59, no. 3, pp. 427-471, 1996.
- [30] D. Semwogerere and E.R. Weeks, "Confocal microscopy," in *Encyclopedia of Biomaterials and Biomedical Engineering*. New York: Taylor and Francis, Feb 2013, pp. 1-10.
- [31] F. Koenig, S. González, W.M. White, M. Lein and M. Rajadhyaksha, "Near-infrared confocal laser scanning microscopy of bladder tissue in vivo," *Urology*, vol. 53, no. 4, pp. 853-857, 1999.
- [32] R.H. Webb, G.W. Hughes and F.C. Delori, "Confocal scanning laser ophthalmoscope," *Appl.Opt.*, vol. 26, no. 8, pp. 1492-1499, 1987.
- [33] M. Rajadhyaksha, M. Grossman, D. Esterowitz, R.H. Webb and R.R. Anderson, "In vivo confocal scanning laser microscopy of human skin: Melanin provides strong contrast," *J.Invest.Dermatol.*, vol. 104, no. 6, pp. 946-952, 1995.
- [34] P.M. Andrews, W.M. Petroll, H.D. Cavanagh and J.V. Jester, "Tandem scanning confocal microscopy (TSCM) of normal and ischemic living kidneys," *Am.J.Anat.*, vol. 191, no. 1, pp. 95-102, 2005.

- [35] J.V. Jester, P.M. Andrews, W. Matthew Petroll, M.A. Lemp and H. Dwight Cavanagh, "In vivo, real-time confocal imaging," *J.Electron Microsc. Tech.*, vol. 18, no. 1, pp. 50-60, 1991.
- [36] U. Günther, S. Daum, F. Heller, M. Schumann, C. Loddenkemper, M. Grünbaum, M. Zeitz and C. Bojarski, "Diagnostic value of confocal endomicroscopy in celiac disease," *Endoscopy*, vol. 42, no. 3, pp. 197-202, 2010.
- [37] K. Banno, Y. Niwa, R. Miyahara, M. Nakamura, T. Nagaya, T. Nagasaka, O. Watanabe, T. Ando, H. Kawashima, N. Ohmiya, A. Itoh, Y. Hirooka and H. Goto, "Confocal endomicroscopy for phenotypic diagnosis of gastric cancer," *J.Gastroenterol.Hepatol.*, vol. 25, no. 4, pp. 712-718, 2010.
- [38] R. Kiesslich, L. Gossner, M. Goetz, A. Dahlmann, M. Vieth, M. Stolte, A. Hoffman, M. Jung, B. Nafe, P.R. Galle and M.F. Neurath, "In vivo histology of Barrett's esophagus and associated neoplasia by confocal laser endomicroscopy," *Clinical Gastroenterology and Hepatology*, vol. 4, no. 8, pp. 979-987, 8 2006.
- [39] R. Kiesslich, J. Burg, M. Vieth, J. Gnaendiger, M. Enders, P. Delaney, A. Polglase, W. McLaren, D. Janell, S. Thomas, B. Nafe, P.R. Galle and M.F. Neurath, "Confocal laser endoscopy for diagnosing intraepithelial neoplasias and colorectal cancer in vivo," *Gastroenterology*, vol. 127, no. 3, pp. 706-713, 9 2004.
- [40] A. Mennone and M.H. Nathanson, "Needle-based confocal laser endomicroscopy to assess liver histology in vivo," *Gastrointest.Endosc.*, vol. 73, no. 2, pp. 338-344, 2 2011.
- [41] R. Kiesslich, M. Goetz, J. Burg, M. Stolte, E. Siegel, M.J. Maeurer, S. Thomas, D. Strand, P.R. Galle and M.F. Neurath, "Diagnosing helicobacter pylori in vivo by confocal laser endoscopy," *Gastroenterology*, vol. 128, no. 7, pp. 2119-2123, 2005.
- [42] S. Yoshida, S. Tanaka, M. Hirata, R. Mouri, I. Kaneko, S. Oka, M. Yoshihara and K. Chayama, "Optical biopsy of GI lesions by reflectance-type laser-scanning confocal microscopy," *Gastrointest.Endosc.*, vol. 66, no. 1, pp. 144-149, 2007.
- [43] W. Denk, J.H. Strickler and W.W. Webb, "Two-photon laser scanning fluorescence microscopy," *Science*, vol. 248, no. 4951, pp. 73-76, 1990.
- [44] L. Fu and M. Gu, "Fibre-optic nonlinear optical microscopy and endoscopy," *J.Microsc.*, vol. 226, no. 3, pp. 195-206, 2007.
- [45] Y.R. Shen, *The principles of nonlinear optics*, New York: Wiley-Interscience, 1984, 575 pp. 1.

- [46] W.R. Zipfel, R.M. Williams and W.W. Webb, "Nonlinear magic: Multiphoton microscopy in the biosciences," *Nat.Biotechnol.*, vol. 21, no. 11, pp. 1369-1377, 2003.
- [47] C. Xu, W. Zipfel, J.B. Shear, R.M. Williams and W.W. Webb, "Multiphoton fluorescence excitation: New spectral windows for biological nonlinear microscopy," *Proceedings of the National Academy of Sciences*, vol. 93, no. 20, pp. 10763-10768, 1996.
- [48] M. Rubart, "Two-photon microscopy of cells and tissue," *Circ.Res.*, vol. 95, no. 12, pp. 1154-1166, 2004.
- [49] P. Theer, M.T. Hasan and W. Denk, "Two-photon imaging to a depth of 1000  $\mu\text{m}$  in living brains by use of a Ti:  $\text{Al}_2\text{O}_3$  regenerative amplifier," *Opt.Lett.*, vol. 28, no. 12, pp. 1022-1024, 2003.
- [50] F. Helmchen and W. Denk, "Deep tissue two-photon microscopy," *Nature methods*, vol. 2, no. 12, pp. 932-940, 2005.
- [51] P.J. Campagnola, M. Wei, A. Lewis and L.M. Loew, "High-resolution nonlinear optical imaging of live cells by second harmonic generation." *Biophys.J.*, vol. 77, no. 6, pp. 3341, 1999.
- [52] P.J. Campagnola and L.M. Loew, "Second-harmonic imaging microscopy for visualizing biomolecular arrays in cells, tissues and organisms," *Nat.Biotechnol.*, vol. 21, no. 11, pp. 1356-1360, 2003.
- [53] R. Gauderon, P. Lukins and C. Sheppard, "Three-dimensional second-harmonic generation imaging with femtosecond laser pulses," *Opt.Lett.*, vol. 23, no. 15, pp. 1209-1211, 1998.
- [54] G. Agrawal, "Nonlinear fiber optics," in *Nonlinear Science at the Dawn of the 21st Century*. Springer Berlin Heidelberg, 2000, pp. 195-211.
- [55] D. Bird and M. Gu, "Fibre-optic two-photon scanning fluorescence microscopy," *J.Microsc.*, vol. 208, no. 1, pp. 35-48, 2002.
- [56] R. Wolleschensky, T. Feurer, R. Sauerbrey and U. Simon, "Characterization and optimization of a laser-scanning microscope in the femtosecond regime," *Appl.Phys. B*, vol. 67, no. 1, pp. 87-94, 1998.
- [57] A.F. Gmitro and D. Aziz, "Confocal microscopy through a fiber-optic imaging bundle," *Opt.Lett.*, vol. 18, no. 8, pp. 565-567, 1993.
- [58] K. Carlson, M. Chidley, K.B. Sung, M. Descour, A. Gillenwater, M. Follen and R. Richards-Kortum, "In vivo fiber-optic confocal reflectance microscope with an

- injection-molded plastic miniature objective lens," *Appl.Opt.*, vol. 44, no. 10, pp. 1792-1797, 2005.
- [59] A.R. Rouse, A. Kano, J.A. Udovich, S.M. Kroto and A.F. Gmitro, "Design and demonstration of a miniature catheter for a confocal microendoscope," *Appl.Opt.*, vol. 43, no. 31, pp. 5763-5771, 2004.
- [60] J. Knittel, L. Schnieder, G. Buess, B. Messerschmidt and T. Possner, "Endoscope-compatible confocal microscope using a gradient index-lens system," *Opt.Commun.*, vol. 188, no. 5-6, pp. 267-273, 2001.
- [61] T. Dabbs and M. Glass, "Fiber-optic confocal microscope: FOCON," *Appl.Opt.*, vol. 31, no. 16, pp. 3030-3035, 1992.
- [62] V.X.D. Yang, M. Gordon, S. Tang, N. Marcon, G. Gardiner, B. Qi, S. Bisland, E. Seng-Yue, S. Lo and J. Pekar, "High speed, wide velocity dynamic range doppler optical coherence tomography (part III): In vivo endoscopic imaging of blood flow in the rat and human gastrointestinal tracts," *Optics Express*, vol. 11, no. 19, pp. 2416-2424, 2003.
- [63] J. Wu, M. Conry, C. Gu, F. Wang, Z. Yaqoob and C. Yang, "Paired-angle-rotation scanning optical coherence tomography forward-imaging probe," *Opt.Lett.*, vol. 31, no. 9, pp. 1265-1267, 2006.
- [64] H.L. Fu, Y. Leng, M.J. Cobb, K. Hsu, J.H. Hwang and X. Li, "Flexible miniature compound lens design for high-resolution optical coherence tomography balloon imaging catheter," *J.Biomed.Opt.*, vol. 13, no. 6, pp. 060502-060502-3, 2008.
- [65] E.J. Seibel and Q.Y.J. Smithwick, "Unique features of optical scanning, single fiber endoscopy," *Lasers Surg.Med.*, vol. 30, no. 3, pp. 177-183, 2002.
- [66] L. Giniunas, R. Juskaitis and S. Shatalin, "Scanning fibre-optic microscope," *Electron.Lett.*, vol. 27, no. 9, pp. 724-726, 1991.
- [67] M.T. Myaing, D.J. MacDonald and X. Li, "Fiber-optic scanning two-photon fluorescence endoscope," *Opt.Lett.*, vol. 31, no. 8, pp. 1076-1078, 2006.
- [68] D. Kim, K.H. Kim, S. Yazdanfar and P.T.C. So, "Optical biopsy in high-speed handheld miniaturized multifocal multiphoton microscopy," in *Proc. of SPIE Vol.*, , 2005, pp. 15.
- [69] F. Helmchen, M.S. Fee, D.W. Tank and W. Denk, "A miniature head-mounted two-photon microscope: High-resolution brain imaging in freely moving animals," *Neuron*, vol. 31, no. 6, pp. 903-912, 2001.

- [70] X. Liu, M.J. Cobb, Y. Chen, M.B. Kimmey and X. Li, "Rapid-scanning forward-imaging miniature endoscope for real-time optical coherence tomography," *Opt.Lett.*, vol. 29, no. 15, pp. 1763-1765, 2004.
- [71] K.C. Maitland, H.J. Shin, H. Ra, D. Lee, O. Solgaard and R. Richards-Kortum, "Single fiber confocal microscope with a two-axis gimbaled MEMS scanner for cellular imaging," *Optics Express*, vol. 14, no. 19, pp. 8604-8612, 2006.
- [72] H.J. Shin, M.C. Pierce, D. Lee, H. Ra, O. Solgaard and R. Richards-Kortum, "Fiber-optic confocal microscope using a MEMS scanner and miniature objective lens," *Optics Express*, vol. 15, no. 15, pp. 9113-9122, 2007.
- [73] J.W. Jeong, M.J. Mandella, G.S. Kino, C.H. Contag and O. Solgaard, "3-D MEMS scanning system for dual-axis confocal microendoscopy," in *Optical MEMS and Nanophotonics (OMN), 2011 International Conference on*, , 2011, pp. 71-72.
- [74] C.L. Arrasmith, D.L. Dickensheets and A. Mahadevan-Jansen, "MEMS-based handheld confocal microscope for in-vivo skin imaging," *Optics express*, vol. 18, no. 4, pp. 3805-3819, 2010.
- [75] W. Piyawattanametha and T.D. Wang, "MEMS-based dual-axes confocal microendoscopy," *Selected Topics in Quantum Electronics, IEEE Journal of*, vol. , no. 99, pp. 1-11, 2011.
- [76] Y. Wang, M. Raj, H. McGuff, T. Shen and X. Zhang, "Portable oral cancer detection using miniature confocal imaging probe with large field of view," in *Solid-State Sensors, Actuators and Microsystems Conference (TRANSDUCERS), 2011 16th International*, , 2011, pp. 1821-1824.
- [77] L. Fu, A. Jain, H. Xie, C. Cranfield and M. Gu, "Nonlinear optical endoscopy based on a double-clad photonic crystal fiber and a MEMS mirror," *Optics Express*, vol. 14, no. 3, pp. 1027-1032, 2006.
- [78] W. Piyawattanametha, R.P.J. Barretto, T.H. Ko, B.A. Flusberg, E.D. Cocker, H. Ra, D. Lee, O. Solgaard and M.J. Schnitzer, "Fast-scanning two-photon fluorescence imaging based on a microelectromechanical systems two-dimensional scanning mirror," *Opt.Lett.*, vol. 31, no. 13, pp. 2018-2020, 2006.
- [79] L. Fu, A. Jain, C. Cranfield, H. Xie and M. Gu, "Three-dimensional nonlinear optical endoscopy," *J.Biomed.Opt.*, vol. 12, no. 4, pp. 40501-41200, 2007.
- [80] T.M. Liu, M.C. Chan, I. Chen, S.H. Chia and C.K. Sun, "Miniaturized multiphoton microscope with a 24Hz frame-rate," *Optics express*, vol. 16, no. 14, pp. 10501-10506, 2008.

- [81] C.L. Hoy, N.J. Durr, P. Chen, W. Piyawattanametha, H. Ra, O. Solgaard and A. Ben-Yakar, "Miniaturized probe for femtosecond laser microsurgery and two-photon imaging," *Optics express*, vol. 16, no. 13, pp. 9996-10005, 2008.
- [82] W. Piyawattanametha, E.D. Cocker, L.D. Burns, R.P.J. Barretto, J.C. Jung, H. Ra, O. Solgaard and M.J. Schnitzer, "< i> in vivo</i> brain imaging using a portable 2.9 g two-photon microscope based on a microelectromechanical systems scanning mirror," *Opt.Lett.*, vol. 34, no. 15, pp. 2309-2311, 2009.
- [83] W. Jung, S. Tang, D.T. McCormic, T. Xie, Y.C. Ahn, J. Su, I.V. Tomov, T.B. Krasieva, B.J. Tromberg and Z. Chen, "Miniaturized probe based on a microelectromechanical system mirror for multiphoton microscopy," *Opt.Lett.*, vol. 33, no. 12, pp. 1324-1326, 2008.
- [84] W. Jung, D.T. McCormick, J. Zhang, L. Wang, N.C. Tien and Z. Chen, "Three-dimensional endoscopic optical coherence tomography by use of a two-axis microelectromechanical scanning mirror," *Appl.Phys.Lett.*, vol. 88, no. , pp. 163901, 2006.
- [85] Y. Pan, H. Xie and G.K. Fedder, "Endoscopic optical coherence tomography based on a microelectromechanical mirror," *Opt.Lett.*, vol. 26, no. 24, pp. 1966-1968, 2001.
- [86] Y. Xu, J. Singh, C. Premachandran, A. Khairyanto, K. Chen, N. Chen, C. Sheppard and M. Olivo, "Design and development of a 3D scanning MEMS OCT probe using a novel SiOB package assembly," *J Micromech Microengineering*, vol. 18, no. , pp. 125005, 2008.
- [87] K.H. Kim, B.H. Park, G.N. Maguluri, T.W. Lee, F.J. Rogomentich, M.G. Bancu, B.E. Bouma, J.F. de Boer and J.J. Bernstein, "Two-axis magnetically-driven MEMS scanning catheter for endoscopic high-speed optical coherence tomography," *Optics Express*, vol. 15, no. 26, pp. 18130-18140, 2007.
- [88] S. Guo, L. Wu, J. Sun, L. Liu and H. Xie, "Three-Dimensional Optical Coherence Tomography Based on a High-Fill-Factor Microelectromechanical Mirror," in *Novel Techniques in Microscopy*, , 2009, pp. .
- [89] K. Kumar, J.C. Condit, A. McElroy, N.J. Kemp, K. Hoshino, T.E. Milner and X. Zhang, "Fast 3D in vivo swept-source optical coherence tomography using a two-axis MEMS scanning micromirror," *Journal of Optics A: Pure and Applied Optics*, vol. 10, no. , pp. 044013, 2008.
- [90] A. Komiyama and M. Hashimoto, "A new class of crosstalk in image fibers," *Opt.Commun.*, vol. 107, no. 1-2, pp. 49-53, 4/1 1994.
- [91] J.B. Pawley, *Handbook of biological confocal microscopy*, 3rd ed. New York: Springer, 2006.

- [92] H.L. Fu, Y. Leng, M.J. Cobb, K. Hsu, J.H. Hwang and X. Li, "Flexible miniature compound lens design for high-resolution optical coherence tomography balloon imaging catheter," *J.Biomed.Opt.*, vol. 13, no. 6, pp. 060502, 2008.
- [93] L. Liu, L. Wu, J. Sun, E. Lin and H. Xie, "Miniature endoscopic optical coherence tomography probe employing a two-axis microelectromechanical scanning mirror with through-silicon vias," *J.Biomed.Opt.*, vol. 16, no. 2, pp. 6006, 2011.
- [94] Y. Pan, H. Xie and G.K. Fedder, "Endoscopic optical coherence tomography based on a microelectromechanical mirror," *Opt.Lett.*, vol. 26, no. 24, pp. 1966-1968, 2001.
- [95] P.F. Van Kessel, L.J. Hornbeck, R.E. Meier and M.R. Douglass, "A MEMS-based projection display," *Proc IEEE*, vol. 86, no. 8, pp. 1687-1704, 2002.
- [96] H. Toshiyoshi and H. Fujita, "Electrostatic micro torsion mirrors for an optical switch matrix," *J Microelectromech Syst*, vol. 5, no. 4, pp. 231-237, 1996.
- [97] Meng-Hsiung Kiang, O. Solgaard, R.S. Muller and K.Y. Lau, "Surface-micromachined electrostatic-comb driven scanning micromirrors for barcode scanners," in *Micro Electro Mechanical Systems, 1996, MEMS '96, Proceedings. 'An Investigation of Micro Structures, Sensors, Actuators, Machines and Systems'. IEEE, The Ninth Annual International Workshop on*, 1996, pp. 192-197.
- [98] N. Doble, G. Yoon, L. Chen, P. Bierden, B. Singer, S. Olivier and D.R. Williams, "Use of a microelectromechanical mirror for adaptive optics in the human eye," *Opt.Lett.*, vol. 27, no. 17, pp. 1537-1539, 2002.
- [99] X. Zhang, A. Liu, D. Tang and C. Lu, "Discrete wavelength tunable laser using microelectromechanical systems technology," *Appl.Phys.Lett.*, vol. 84, no. 3, pp. 329-331, 2004.
- [100] O. Manzardo, H.P. Herzig, C.R. Marxer and N.F. de Rooij, "Miniaturized time-scanning fourier transform spectrometer based on silicon technology," *Opt.Lett.*, vol. 24, no. 23, pp. 1705-1707, 1999.
- [101] L. Wu, A. Pais, S.R. Samuelson, S. Guo and H. Xie, "A Miniature Fourier Transform Spectrometer by a Large-Vertical-Displacement Microelectromechanical Mirror," in *Fourier Transform Spectroscopy*, 2009, pp. FWD4.
- [102] M. Hacker, G. Stobrawa, R. Sauerbrey, T. Buckup, M. Motzkus, M. Wildenhain and A. Gehner, "Micromirror SLM for femtosecond pulse shaping in the ultraviolet," *Appl.Phys. B*, vol. 76, no. 6, pp. 711-714, 2003.
- [103] K.E. Petersen, "Silicon torsional scanning mirror," *IBM Journal of Research and Development*, vol. 24, no. 5, pp. 631-637, 1980.

- [104] L. Fan and M. Wu, "Two-dimensional optical scanner with large angular rotation realized by self-assembled micro-elevator," in *Broadband Optical Networks and Technologies: An Emerging Reality/Optical MEMS/Smart Pixels/Organic Optics and Optoelectronics. 1998 IEEE/LEOS Summer Topical Meetings*, 1998, pp. II/107-II/108.
- [105] C.G. Agudelo, M. Packirisamy, G. Zhu and L. Saydy, "Nonlinear control of an electrostatic micromirror beyond pull-in with experimental validation," *Microelectromechanical Systems, Journal of*, vol. 18, no. 4, pp. 914-923, 2009.
- [106] Y. Ma, S. Islam and Y.J. Pan, "Electrostatic torsional micromirror with enhanced tilting angle using active control methods," *Mechatronics, IEEE/ASME Transactions on*, vol. 16, no. 6, pp. 994-1001, 2011.
- [107] Z. Hao, B. Wingfield, M. Whitley, J. Brooks and J.A. Hammer, "A design methodology for a bulk-micromachined two-dimensional electrostatic torsion micromirror," *Microelectromechanical Systems, Journal of*, vol. 12, no. 5, pp. 692-701, 2003.
- [108] K. Joudrey, G.G. Adams and N.E. McGruer, "Design, modeling, fabrication and testing of a high aspect ratio electrostatic torsional MEMS micromirror," *J Micromech Microengineering*, vol. 16, no. 10, pp. 2147, 2006.
- [109] M.R. Dokmeci, A. Pareek, S. Bakshi, M. Waelti, C.D. Fung, K.H. Heng and C.H. Mastrangelo, "Two-axis single-crystal silicon micromirror arrays," *Microelectromechanical Systems, Journal of*, vol. 13, no. 6, pp. 1006-1017, 2004.
- [110] J.L.A. Yeh, H. Jiang and N.C. Tien, "Integrated polysilicon and DRIE bulk silicon micromachining for an electrostatic torsional actuator," *Microelectromechanical Systems, Journal of*, vol. 8, no. 4, pp. 456-465, 1999.
- [111] H. Schenk, P. Durr, T. Haase, D. Kunze, U. Sobe, H. Lakner and H. Kuck, "Large deflection micromechanical scanning mirrors for linear scans and pattern generation," *Selected Topics in Quantum Electronics, IEEE Journal of*, vol. 6, no. 5, pp. 715-722, 2000.
- [112] G.D.J. Su, H. Toshiyoshi and M.C. Wu, "Surface-micromachined 2-D optical scanners with high-performance single-crystalline silicon micromirrors," *Photonics Technology Letters, IEEE*, vol. 13, no. 6, pp. 606-608, 2001.
- [113] D. Lee, U. Krishnamoorthy, K. Yu and O. Solgaard, "Single-crystalline silicon micromirrors actuated by self-aligned vertical electrostatic combdrives with piston-motion and rotation capability," *Sensors and Actuators A: Physical*, vol. 114, no. 2, pp. 423-428, 2004.

- [114] P.R. Patterson, D. Hah, H. Nguyen, H. Toshiyoshi, R. Chao and M.C. Wu, "A scanning micromirror with angular comb drive actuation," in *Micro Electro Mechanical Systems, 2002. The Fifteenth IEEE International Conference on*, 2002, pp. 544-547.
- [115] M.H. Jun, S. Moon and J.H. Lee, "A microassembly process to realize angular vertical comb electrodes for a gimbal-less two-axis electrostatic scanner," in *Micro Electro Mechanical Systems (MEMS), 2012 IEEE 25th International Conference on*, 2012, pp. 624-627.
- [116] V. Milanovic, G.A. Matus and D.T. McCormick, "Gimbal-less monolithic silicon actuators for tip-tilt-piston micromirror applications," *Selected Topics in Quantum Electronics, IEEE Journal of*, vol. 10, no. 3, pp. 462-471, 2004.
- [117] V. Milanovic, K. Castelino and D. McCormick, "Fully-Functional Tip-Tilt-Piston Micromirror array," in *Optical MEMS and Their Applications Conference, 2006. IEEE/LEOS International Conference on*, 2006, pp. 38-39.
- [118] V. Milanović, G. Matus and D.T. McCormick, "Tip-tilt-piston actuators for high fill-factor micromirror arrays," *the Proceedings of Hilton Head*, 2004, pp. 232-237.
- [119] V. Milanovic, K. Castelino and D.T. McCormick, "Highly adaptable MEMS-based display with wide projection angle," in *Micro Electro Mechanical Systems, 2007. MEMS. IEEE 20th International Conference on*, 2007, pp. 143-146.
- [120] J. Tsai, T. Hsieh, S. Chiou, D. Hah and M.C. Wu, "Experimental characterization of two-axis MEMS scanners with hidden radial vertical combdrive actuators and cross-bar spring structures," *J Micromech Microengineering*, vol. 19, no. 4, pp. 045002, 2009.
- [121] H. Miyajima, N. Asaoka, M. Arima, Y. Minamoto, K. Murakami, K. Tokuda and K. Matsumoto, "A durable, shock-resistant electromagnetic optical scanner with polyimide-based hinges," *Microelectromechanical Systems, Journal of*, vol. 10, no. 3, pp. 418-424, 2001.
- [122] A.D. Yalcinkaya, H. Urey, D. Brown, T. Montague and R. Sprague, "Two-axis electromagnetic microscanner for high resolution displays," *Microelectromechanical Systems, Journal of*, vol. 15, no. 4, pp. 786-794, 2006.
- [123] C.H. Ji, M. Choi, S.C. Kim, K.C. Song, J.U. Bu and H.J. Nam, "Electromagnetic two-dimensional scanner using radial magnetic field," *Microelectromechanical Systems, Journal of*, vol. 16, no. 4, pp. 989-996, 2007.
- [124] H.A. Yang, T.L. Tang, S.T. Lee and W. Fang, "A novel coilless scanning mirror using eddy current lorentz force and magnetostatic force," *Microelectromechanical Systems, Journal of*, vol. 16, no. 3, pp. 511-520, 2007.

- [125] Y. Yee, H.J. Nam, S.H. Lee, J.U. Bu and J.W. Lee, "PZT actuated micromirror for fine-tracking mechanism of high-density optical data storage," *Sensors and Actuators A: Physical*, vol. 89, no. 1, pp. 166-173, 2001.
- [126] J. Tsaur, L. Zhang, R. Maeda and S. Matsumoto, "2D micro scanner actuated by sol-gel derived double layered PZT," in *Micro Electro Mechanical Systems, 2002. The Fifteenth IEEE International Conference on*, 2002, pp. 548-551.
- [127] F. Filhol, E. Defay, C. Divoux, C. Zinck and M.T. Delaye, "Resonant micro-mirror excited by a thin-film piezoelectric actuator for fast optical beam scanning," *Sensors and Actuators A: Physical*, vol. 123, pp. 483-489, 2005.
- [128] K.H. Koh, T. Kobayashi and C. Lee, "A 2-D MEMS scanning mirror based on dynamic mixed mode excitation of a piezoelectric PZT thin film S-shaped actuator," *Optics express*, vol. 19, no. 15, pp. 13812-13824, 2011.
- [129] J.H. Park and J. Akedo, "Fabrication and scanning-angle temperature dependence of metal-based, optical resonant scanners with PZT actuation," *Ultrasonics, Ferroelectrics and Frequency Control, IEEE Transactions on*, vol. 55, no. 5, pp. 942-945, 2008.
- [130] M. Tani, M. Akamatsu, Y. Yasuda and H. Toshiyoshi, "A two-axis piezoelectric tilting micromirror with a newly developed PZT-meandering actuator," in *Micro Electro Mechanical Systems, 2007. MEMS. IEEE 20th International Conference on*, 2007, pp. 699-702.
- [131] Y. Zhu, W. Liu, K. Jia, W. Liao and H. Xie, "A piezoelectric unimorph actuator based tip-tilt-piston micromirror with high fill factor and small tilt and lateral shift," *Sensors and Actuators A: Physical*, vol. 167, no. 2, pp. 495-501, 2011.
- [132] R. Buser, N. De Rooij, H. Tischhauser, A. Dommann and G. Staufert, "Biaxial scanning mirror activated by bimorph structures for medical applications," *Sensors and Actuators A: Physical*, vol. 31, no. 1-3, pp. 29-34, 1992.
- [133] J. Buhler, J. Funk, O. Paul, F.P. Steiner and H. Baltes, "Thermally actuated CMOS micromirrors," *Sensors and Actuators A: Physical*, vol. 47, no. 1-3, pp. 572-575, 1995.
- [134] A. Jain, A. Kopa, Y. Pan, G.K. Fedder and H. Xie, "A two-axis electrothermal micromirror for endoscopic optical coherence tomography," *Selected Topics in Quantum Electronics, IEEE Journal of*, vol. 10, no. 3, pp. 636-642, 2004.
- [135] J. Singh, J. Teo, Y. Xu, C. Premachandran, N. Chen, R. Kotlanka, M. Olivo and C. Sheppard, "A two axes scanning SOI MEMS micromirror for endoscopic bioimaging," *J Micromech Microengineering*, vol. 18, no. 2, pp. 025001, 2007.

- [136] L. Wu and H. Xie, "A large vertical displacement electrothermal bimorph microactuator with very small lateral shift," *Sensors and Actuators A: Physical*, vol. 145, pp. 371-379, 2008.
- [137] K. Jia, S. Pal and H. Xie, "An electrothermal Tip–Tilt–Piston micromirror based on folded dual S-shaped bimorphs," *Microelectromechanical Systems, Journal of*, vol. 18, no. 5, pp. 1004-1015, 2009.
- [138] D.H. Kim, Y.C. Park and S. Park, "Design and fabrication of twisting-type thermal actuation mechanism for micromirrors," *Sensors and Actuators A: Physical*, vol. 159, no. 1, pp. 79-87, 2010.
- [139] H. Xie, Y. Pan and G.K. Fedder, "A CMOS-MEMS mirror with curled-hinge comb drives," *Microelectromechanical Systems, Journal of*, vol. 12, no. 4, pp. 450-457, 2003.
- [140] J.M. Byun, J.S. Han, J.H. Park, S.E. Lee and H.C. Lee, "A study on the piezoelectric properties of PZT and doped PZT thin films by sol-gel method," in *Materials Science Forum*, 2011, pp. 650-653.
- [141] M. Dekkers, M.D. Nguyen, R. Steenwelle, P.M. Te Riele, D.H.A. Blank and G. Rijnders, "Ferroelectric properties of epitaxial pb (zr, ti) O thin films on silicon by control of crystal orientation," *Appl.Phys.Lett.*, vol. 95, pp. 012902, 2009.
- [142] N. Izyumskaya, Y.I. Alivov, S.J. Cho, H. Morkoc, H. Lee and Y.S. Kang, "Processing, structure, properties, and applications of PZT thin films," *Critical reviews in solid state and materials sciences*, vol. 32, no. 3-4, pp. 111-202, 2007.
- [143] K. Budd, S. Key and D. Payne, "Sol-gel processing of PbTiO<sub>3</sub>, PbZrO<sub>3</sub>, PZT and PLZT thin films," in *BR. CERAM. PROC. Br. Ceram. Proc.*, 1985, pp. 107.
- [144] Y. Sakashita, T. Ono, H. Segawa, K. Tominaga and M. Okada, "Preparation and electrical properties of MOCVD-deposited PZT thin films," *J.Appl.Phys.*, vol. 69, no. 12, pp. 8352-8357, 1991.
- [145] C.K. Kwok and S.B. Desu, "Low temperature perovskite formation of lead zirconate titanate thin films by a seeding process," *J.Mater.Res.*, vol. 8, no. 2, pp. 339-344, 1993.
- [146] X. Meng, J. Cheng, B. Li, S. Guo, H. Ye and J. Chu, "Low-temperature preparation of highly (111) oriented PZT thin films by a modified sol–gel technique," *J.Cryst.Growth*, vol. 208, no. 1, pp. 541-545, 2000.
- [147] C. Zinck, D. Pinceau, E. Defajé E. Delevoye and D. Barbier, "Development and characterization of membranes actuated by a PZT thin film for MEMS applications," *Sens Actuators A Phys*, vol. 115, no. 2-3 SPEC. ISS., pp. 483-489, 2004.

- [148] R. Tyson, *Principles of adaptive optics*, ed. CRC Press, 2010.
- [149] F. Roddier, *Adaptive optics in astronomy*, ed. Cambridge university press, 1999.
- [150] E.J. Fernandez, L. Vabre, B. Hermann, A. Unterhuber, B. Povazay and W. Drexler, "Adaptive optics with a magnetic deformable mirror: Applications in the human eye," *Optics Express*, vol. 14, no. 20, pp. 8900-8917, 2006.
- [151] S. Kuiper and B. Hendriks, "Variable-focus liquid lens for miniature cameras," *Appl.Phys.Lett.*, vol. 85, no. 7, pp. 1128-1130, 2004.
- [152] D.Y. Zhang, N. Justis and Y.H. Lo, "Integrated fluidic adaptive zoom lens," *Opt.Lett.*, vol. 29, no. 24, pp. 2855-2857, 2004.
- [153] A. Jain and H. Xie, "Microendoscopic confocal imaging probe based on an LVD microlens scanner," *Selected Topics in Quantum Electronics, IEEE Journal of*, vol. 13, no. 2, pp. 228-234, 2007.
- [154] K. Aljaseem, A. Werber, A. Seifert and H. Zappe, "Fiber optic tunable probe for endoscopic optical coherence tomography," *Journal of Optics A: Pure and Applied Optics*, vol. 10, no. 4, pp. 044012, 2008.
- [155] L. Wu and H. Xie, "A millimeter-tunable-range microlens for endoscopic biomedical imaging applications," *Quantum Electronics, IEEE Journal of*, vol. 46, no. 9, pp. 1237-1244, 2010.
- [156] S. Kwon and L.P. Lee, "Stacked two dimensional micro-lens scanner for micro confocal imaging array," in *Micro Electro Mechanical Systems, 2002. The Fifteenth IEEE International Conference on*, 2002, pp. 483-486.
- [157] M. Wu, S.Y. Hsiao, C.Y. Peng and W. Fang, "Development of tracking and focusing micro actuators for dual-stage optical pick-up head," *Journal of Optics A: Pure and Applied Optics*, vol. 8, no. 7, pp. S323, 2006.
- [158] S.H. Kim, Y. Yee, J. Choi, H. Kwon, M.H. Ha, C. Oh and J.U. Bu, "A micro optical flying head for a PCMCIA-sized optical data storage," in *Micro Electro Mechanical Systems, 2004. 17th IEEE International Conference on.(MEMS)*, 2004, pp. 85-88.
- [159] S. Suyama, M. Date and H. Takada, "Three-dimensional display system with dual-frequency liquid-crystal varifocal lens," *Japanese Journal of Applied Physics*, vol. 39, pp. 480, 2000.
- [160] T. Krupenkin, S. Yang and P. Mach, "Tunable liquid microlens," *Appl.Phys.Lett.*, vol. 82, no. 3, pp. 316-318, 2003.

- [161] B. Berge and J. Peseux, "Variable focal lens controlled by an external voltage: An application of electrowetting," *The European Physical Journal E: Soft Matter and Biological Physics*, vol. 3, no. 2, pp. 159-163, 2000.
- [162] W. Wang and J. Fang, "Design, fabrication and testing of a micromachined integrated tunable microlens," *J Micromech Microengineering*, vol. 16, no. 7, pp. 1221, 2006.
- [163] D.Y. Zhang, V. Lien, Y. Berdichevsky, J. Choi and Y.H. Lo, "Fluidic adaptive lens with high focal length tunability," *Appl.Phys.Lett.*, vol. 82, no. 19, pp. 3171-3172, 2003.
- [164] N. Sugiura and S. Morita, "Variable-focus liquid-filled optical lens," *Appl.Opt.*, vol. 32, no. 22, pp. 4181-4186, 1993.
- [165] S. Sato, "Applications of liquid crystals to variable-focusing lenses," *Optical Review*, vol. 6, no. 6, pp. 471-485, 1999.
- [166] X. Zeng and H. Jiang, "Tunable liquid microlens actuated by infrared light-responsive hydrogel," *Appl.Phys.Lett.*, vol. 93, no. 15, pp. 151101-151101-3, 2008.
- [167] J. Chen, W. Wang, J. Fang and K. Varahramyan, "Variable-focusing microlens with microfluidic chip," *J Micromech Microengineering*, vol. 14, no. 5, pp. 675, 2004.
- [168] C. Gorecki, L. Nieradko, S. Bargiel, J. Dziuban, D. Henis, J. Sylvestre, K. Alkowska, G. Soto-Romero, J. Thevenet and R. Yahiaoui, "On-chip scanning confocal microscope with 3D MEMS scanner and VCSEL feedback detection," in *Solid-State Sensors, Actuators and Microsystems Conference*, 2007, pp. 2561-2564.
- [169] S. Kwon, V. Milanovic and L.P. Lee, "Large-displacement vertical microlens scanner with low driving voltage," *Photonics Technology Letters, IEEE*, vol. 14, no. 11, pp. 1572-1574, 2002.
- [170] S. Kwon and L.P. Lee, "Stacked two dimensional micro-lens scanner for micro confocal imaging array," in *Micro Electro Mechanical Systems, 2002. The Fifteenth IEEE International Conference on*, 2002, pp. 483-486.
- [171] A. Jain and H. Xie, "An electrothermal microlens scanner with low-voltage large-vertical-displacement actuation," *Photonics Technology Letters, IEEE*, vol. 17, no. 9, pp. 1971-1973, 2005.
- [172] S. Kwon, V. Milanovic and L.P. Lee, "Large-displacement vertical microlens scanner with low driving voltage," *Photonics Technology Letters, IEEE*, vol. 14, no. 11, pp. 1572-1574, 2002.

- [173] S.K. Gokce, S. Holmstrom, C. Hibert, S. Olcer, D. Bowman and H. Urey, "Two-dimensional MEMS stage integrated with microlens arrays for laser beam steering," *Microelectromechanical Systems, Journal of*, vol. 20, no. 1, pp. 15-17, 2011.
- [174] L. Wu and H. Xie, "A millimeter-tunable-range microlens for endoscopic biomedical imaging applications," *Quantum Electronics, IEEE Journal of*, vol. 46, no. 9, pp. 1237-1244, 2010.
- [175] J. Fujimoto, C. Pitris, S. Boppart and M. Brezinski, "Optical coherence tomography: An emerging technology for biomedical imaging and optical biopsy," *Neoplasia*, vol. 2, no. 1-2, pp. 9-25, JAN-APR 2000.
- [176] K. Takada, I. Yokohama, K. Chida and J. Noda, "New measurement system for fault location in optical waveguide devices based on an interferometric technique," *Appl.Opt.*, vol. 26, no. 9, pp. 1603-1606, 1987.
- [177] R.C. Youngquist, S. Carr and D.E.N. Davies, "Optical coherence-domain reflectometry: A new optical evaluation technique," *Opt.Lett.*, vol. 12, no. 3, pp. 158-160, 1987.
- [178] B.E. Bouma and G.J. Tearney, *Handbook of optical coherence tomography*, ed. New York: Marcel Dekker, 2002.
- [179] D.M. SHOTTON, "Confocal scanning optical microscopy and its applications for biological specimens," *J.Cell.Sci.*, vol. 94, no. 2, pp. 175-206, 1989.
- [180] B. Tata and B. Raj, "Confocal laser scanning microscopy: Applications in material science and technology," *Bull.Mater.Sci.*, vol. 21, no. 4, pp. 263-278, 1998.
- [181] P. Török and L. Mule'Stagno, "Applications of scanning optical microscopy in materials science to detect bulk microdefects in semiconductors," *J.Microsc.*, vol. 188, no. 1, pp. 1-16, 1997.
- [182] J.W. Lichtman and J.A. Conchello, "Fluorescence microscopy," *Nature Methods*, vol. 2, no. 12, pp. 910-919, 2005.
- [183] G.H. Patterson, S.M. Knobel, W.D. Sharif, S.R. Kain and D.W. Piston, "Use of the green fluorescent protein and its mutants in quantitative fluorescence microscopy," *Biophys.J.*, vol. 73, no. 5, pp. 2782-2790, 1997.
- [184] C. Mann, L. Yu, C.M. Lo and M. Kim, "High-resolution quantitative phase-contrast microscopy by digital holography," *Optics Express*, vol. 13, no. 22, pp. 8693-8698, 2005.
- [185] C. Burch and J. Stock, "Phase-contrast microscopy," *J.Sci.Instrum.*, vol. 19, no. , pp. 71, 1942.

- [186] H. Neumann, R. Kiesslich, M.B. Wallace and M.F. Neurath, "Confocal laser endomicroscopy: Technical advances and clinical applications," *Gastroenterology*, vol. 139, no. 2, pp. 388-392.e2, 2010.
- [187] P.M. Delaney, M.R. Harris and R.G. King, "Fiber-optic laser scanning confocal microscope suitable for fluorescence imaging," *Appl.Opt.*, vol. 33, no. 4, pp. 573-577, 1994.
- [188] K.B. Sung, C. Liang, M. Descour, T. Collier, M. Follen and R. Richards-Kortum, "Fiber-optic confocal reflectance microscope with miniature objective for in vivo imaging of human tissues," *Biomedical Engineering, IEEE Transactions on*, vol. 49, no. 10, pp. 1168-1172, 2002.
- [189] L.B. Freund and S. Suresh, *Thin film materials: stress, defect formation and surface evolution*. Cambridge University Press, 2004.
- [190] J.A. Thornton and D. Hoffman, "Stress-related effects in thin films," *Thin Solid Films*, vol. 171, no. 1, pp. 5-31, 1989.
- [191] M. Ohring, *Materials science of thin films*. Academic press, 2001.
- [192] M.J. Madou, *Fundamentals of microfabrication: the science of miniaturization*. CRC, 2002.
- [193] G. Lammel, S. Schweizer and P. Renaud, *Optical microscanners and microspectrometers using thermal bimorph actuators*. Springer, 2002.
- [194] S.T. Todd, " *Electrothermomechanical modeling of a 1-D electrothermal MEMS micromirror* ", M.S. thesis, ECE, Univ. of Florida, FL, 2005.
- [195] S.T. Todd and H. Xie, "An electrothermomechanical lumped element model of an electrothermal bimorph actuator," *Microelectromechanical Systems, Journal of*, vol. 17, no. 1, pp. 213-225, 2008.
- [196] S. Pal and H. Xie, "Analysis and simulation of curved bimorph microactuators," *Proc. Nanotech*, 2010, pp. 685-688.
- [197] A. Blake, "THE HANDBOOK OF MECHANICS, MATERIALS, AND STRUCTURES," A.Blake, Ed., Wiley and Sons, Inc., New York, NY, 1985,\$ 64.50, To order, contact Brian Johnson, John Wiley and Sons, Inc., 605 Third Avenue, New York, NY 10158, vol. , no. , pp. , 1985.
- [198] H.I. M Okaji and, "A practical measurement system for the accurate determination of linear thermal expansion coefficients," *Journal of Physics E: Scientific Instruments*, vol. 17, no. 8, pp. 669, 1984.

[199] W. Riethmuller and W. Benecke, "Thermally excited silicon microactuators,"  
*Electron Devices, IEEE Transactions on*, vol. 35, no. 6, pp. 758-763, 1988.

## BIOGRAPHICAL SKETCH

Lin Liu was born in Xiangyang, Hubei, China in November of 1986. She enrolled in the Huazhong University of Science and Technology of China, Wuhan, Hubei China in the fall of 2004. Based on her academic excellence, she was awarded first-class scholarship and received her B.S. degree in optical science & technology in June 2008.

Lin joined the Biophotonics and Microsystems Lab, Interdisciplinary Microsystems Group at the University of Florida in August of 2008 to pursue her Ph.D. degree in electrical engineering. She received University of Florida Alumni Graduate Award from 2008 to 2012. Her main research focus is on the development of MEMS micromirrors and microlenses and MEMS-based biomedical imaging systems including endoscopic optical coherence tomography system and confocal scanning endomicroscope. Her research interests include MEMS actuators, MEMS optical scanners, endoscopic biomedical imaging, MEMS-based optical coherence tomography, and MEMS-based confocal scanning microscopy. Upon the completion of her dissertation, she has contributed more than 10 research publications on prestigious journals and conferences and 2 provisional patents from her doctoral research.

Lin is a member of the Institute of Electrical and Electronics Engineers and the Optical Society of America. She will pursue a career in the fields of MEMS and optics after receiving her Ph. D. degree in May 2013.